FEDERAL UNIVERSITY OF SÃO CARLOS
CENTER OF EXACT SCIENCES AND TECHNOLOGY
GRADUATE PROGRAM IN MATERIALS SCIENCE AND ENGINEERING

ON THE INTERPLAY BETWEEN INTERSTITIAL DOPING, GRAIN SIZE, AND TRIP EFFECT IN A CrCoNi ALLOY

Gustavo Bertoli

São Carlos-SP
2026

FEDERAL UNIVERSITY OF SÃO CARLOS
CENTER OF EXACT SCIENCES AND TECHNOLOGY
GRADUATE PROGRAM IN MATERIALS SCIENCE AND ENGINEERING

ON THE INTERPLAY BETWEEN INTERSTITIAL DOPING, GRAIN SIZE, AND TRIP EFFECT IN A CrCoNi ALLOY

Gustavo Bertoli

Thesis submitted to the Graduate Program in Materials Science and Engineering as a partial requirement for obtaining the title of DOCTOR OF MATERIALS SCIENCE AND ENGINEERING.

Advisor: Dr. Claudio S. Kiminami
Co-advisor: Dr. Francisco G. Coury
Funding Agency:
FAPESP (Brazil) - Grant number: 2021-05408-4
FAPESP (RIA/BEPE) - Grant number: 2023-16311-7

São Carlos-SP
2026

VITAE

Master's degree in Materials Science and Engineering, Federal University of São Carlos (2021).

Bachelor's degree in Materials and Manufacturing Engineering, University of São Paulo (2018).

APPROVAL SHEET

UNIVERSIDADE FEDERAL DE SÃO CARLOS

Centro de Ciências Exatas e de Tecnologia
Programa de Pós-Graduação em Ciência e Engenharia de Materiais

Folha de Aprovação

Defesa de Tese de Doutorado do candidato Gustavo Bertoli, realizada em 26/02/2026.

Comissão Julgadora:

Prof. Dr. Claudio Shyinti Kiminami (UFSCar)

Prof. Dr. Eric Marchezini Mazzer (UFSCar)

Prof. Dr. Lucas Barcelos Otani (UFSCar)

Prof. Dr. Hélio Goldenstein (USP)

Prof. Dr. Rubens Caram Júnior (UNICAMP)

O Relatório de Defesa assinado pelos membros da Comissão Julgadora encontra-se arquivado junto ao Programa de Pós-Graduação em Ciência e Engenharia de Materiais.

ACKNOWLEDGEMENTS

First, I would like to thank my advisors: Prof. Dr. Claudio S. Kiminami (advisor in Brazil), Prof. Dr. Francisco G. Coury (co-advisor in Brazil), and Prof. Dr. Michael J. Kaufman (advisor abroad). I am grateful for the opportunity to be part of the research group, for their guidance throughout my doctoral studies, and especially for their exemplary conduct as researchers and professors, which continually inspires me.

To the members of the examination committee: Dr. Lucas B. Otani, Dr. Eric M. Mazzer, Dr. Rubens Caram Jr., Dr. Hélio Goldenstein, Dr. Guilherme Zepon, and Dr. Julian A. Avila Diaz.

I also thank the many collaborators, with whom I had the privilege to work, for their support, discussions, and guidance.

I acknowledge the Federal University of São Carlos (UFSCar), the Department of Materials Engineering (DEMa), the Graduate Program in Materials Science and Engineering (PPG-CEM), the Colorado School of Mines (CSM), the Structural Characterization Laboratory (LCE), the Argonne National Laboratory (ANL/APS), and the Deutsches Elektronen-Synchrotron (DESY/PETRA III), for all the resources and support provided. My sincere thanks go to all staff members and colleagues from the institutions mentioned above for their assistance and guidance.

I am grateful to all members of my research group, the High-Entropy Alloy Design (HEAD) group, for the collaboration and insightful discussions.

I would also like to thank my girlfriend Juliana B. de Camargo (Ph.D. student in biomolecular physics), my friend Igor P. Zago (postdoctoral researcher in aeronautical/materials engineering), my brother Guilherme Bertoli (undergraduate student in materials science and engineering), for the many discussions about our research, life, the universe, and everything.

I am deeply grateful to my parents, Silvia H. B. Bertoli and João R. Bertoli Jr., for their support and encouragement, which were essential for the completion of this work.

This study was financed by the São Paulo Research Foundation (FAPESP) through scholarship grants 2021/05408-4 and 2023/16311-7.

This study was financed in part by the Coordenação de Aperfeiçoamento de Pessoal de Nível Superior - Brasil (CAPES) - Finance Code 001.

ABSTRACT

After the popularization of medium/high entropy alloys, some CrCoNi alloys are gaining attention for their outstanding toughness and mechanical performance. The Cr- and Co-rich alloys, such as $Cr_{40}Co_{40}Ni_{20}$, present a favorable combination of two mechanisms: the FCC to HCP strain-induced phase transformation (TRIP effect), which provides improved ductility and toughness; and a high strengthening potential via grain refining, which significantly enhances its mechanical strength. Furthermore, interstitial doping with C or N can strengthen the alloy by inducing precipitation and microstructural refinement. However, according to recent review papers, the influence of these interstitial elements on TRIP effect and stacking fault energy (SFE) is still controversial, and the related explanation is not completely convincing. The objective of this work is to evaluate the interplay between interstitial doping, grain refinement, and TRIP effect. Firstly, *in situ* synchrotron X-ray diffraction during tensile testing allowed us to observe and quantify the strain-induced transformation throughout the entire test. The results indicated that: in terms of stress, the critical stress for TRIP is proportional to the grain refinement strengthening; and in terms of strain, grain size has no obvious influence on TRIP effect. Then, the effect of C and N on phase equilibria, grain refinement capacity, and TRIP effect was evaluated. C-doping promoted the formation of $M_{23}C_6$ precipitates, which was highly effective in inducing grain refinement through the pinning mechanism, while N-doping did not promote the formation of nitrides, but also induced grain refinement to a lesser extent. Both C and N affected the extent of the TRIP effect by altering the SFE. The N addition disfavored the TRIP effect, while C addition did not show monotonic behavior, but higher C levels also disfavored TRIP effect. For these low SFE alloys, the martensitic HCP phase is transformed back into the FCC phase during heating (martensite reversion) by recrystallization of the FCC matrix, and not by a displacive or diffusional HCP to FCC transformation before recrystallization. These findings highlight the complex interplay of mechanisms governing the microstructure and deformation behavior of CrCoNi alloys.

Keywords: Grain size; Interstitial doping; TRIP effect; Strain-induced phase transformation; Recrystallization; CrCoNi.

RESUMO

INTERAÇÃO ENTRE DOPAGEM INTERSTICIAL, TAMANHO DE GRÃO E EFEITO TRIP EM UMA LIGA CrCoNi.

Após a popularização das ligas de média/alta entropia, algumas ligas CrCoNi têm ganhado destaque por sua excepcional tenacidade e desempenho mecânico. As ligas ricas em Cr e Co, como a $Cr_{40}Co_{40}Ni_{20}$, apresentam uma combinação favorável de dois mecanismos: a transformação de fase induzida por deformação de CFC para HCP (efeito TRIP), que proporciona maior ductilidade e tenacidade; e um alto potencial de endurecimento via refino de grão, que aumenta significativamente sua resistência mecânica. Além disso, a dopagem intersticial com C ou N pode endurecer a liga induzindo precipitação e refino microestrutural. No entanto, artigos de revisão recentes apontam que a influência desses intersticiais no efeito TRIP e na energia de falha de empilhamento (EFE) ainda é controversa. O objetivo deste trabalho é avaliar a interação entre a dopagem intersticial, o refinamento de grão e o efeito TRIP. Primeiramente, difração de raios-X *in situ* durante ensaios de tração permitiu observar e quantificar o efeito TRIP. Os resultados indicaram que a tensão crítica para o efeito TRIP é proporcional ao endurecimento por refino de grão, e em termos de deformação, o tamanho do grão não tem influência significativa. Em seguida, avaliou-se o efeito do C e do N no equilíbrio de fases, na capacidade de refino de grão e no efeito TRIP. A dopagem com C promoveu a formação de precipitados $M_{23}C_6$, que foram muito eficazes no refino de grão, enquanto a dopagem com N não promoveu a formação de nitretos, mas também induziu o refinamento de grão em menor grau. C e N afetaram a extensão do efeito TRIP ao alterar a EFE: N desfavoreceu o efeito TRIP, enquanto C não apresentou comportamento monotônico, mas maiores teores de C também desfavoreceram o efeito TRIP. Nessas ligas com baixa EFE, a fase martensítica HCP é revertida em CFC durante o aquecimento por recristalização, e não por uma transformação displaciva ou difusional antes da recristalização. Esses resultados destacam a complexa interação de mecanismos que governam a microestrutura e o comportamento de deformação das ligas CrCoNi.

Palavras-chave: Tamanho de grão; Dopagem intersticial; Efeito TRIP; Transformação de fase induzida por deformação; Recristalização; CrCoNi.

PUBLICATIONS

Gustavo Bertoli; Amy J. Clarke; Michael J. Kaufman; Claudio S. Kiminami; Francisco G. Coury. Influence of grain size on strain-induced phase transformation in a CrCoNi multi-principal element alloy. **International Journal of Plasticity (IF = 12.8)**, v. 183, p. 104164, 2024. Available at: <https://doi.org/10.1016/j.ijplas.2024.104164>.

Gustavo Bertoli; Lucas B. Otani; Amy J. Clarke; Claudio S. Kiminami; Francisco G. Coury. Hall–Petch and grain growth kinetics of the low stacking fault energy TRIP $Cr_{40}Co_{40}Ni_{20}$ multi-principal element alloy. **Applied Physics Letters (IF = 3.6)**, v. 119, n. 6, 2021. Available at: <https://doi.org/10.1063/5.0057888>.

Guilherme C. Stumpf; **Gustavo Bertoli**; Francisco G. Coury; Augusta C. Isaac Neta; Luciano A. Montoro; Roberto B. Figueiredo; Witor Wolf. Stacking-fault networks with Lomer-Cottrell locks induced by carbon addition in a severely strained Cr-Co-Ni alloy. **Journal of Alloys and Compounds (IF = 6.3)**, p. 181162, 2025. Available at: <https://doi.org/10.1016/j.jallcom.2025.181162>.

David D.S. Silva; **Gustavo Bertoli**; Paul Mason; Nelson D. Campos Neto; Norbert Schell; Michael J. Kaufman; Amy J. Clarke; Francisco G. Coury; Claudemiro Bolfarini. Metastability-engineering strategy in CoCrFeMnNi-based medium-and high-entropy alloys: Unraveling the interplay with recrystallization, grain growth, and mechanical properties. **International Journal of Plasticity (IF = 12.8)**, v. 187, p. 104285, 2025. Available at: <https://doi.org/10.1016/j.ijplas.2025.104285>.

David D.S. Silva; **Gustavo Bertoli**; Nelson D. Campos Neto; Norbert Schell; Kester D. Clarke; Michael J. Kaufman; Amy J. Clarke; Francisco G. Coury; Claudemiro Bolfarini. Computational thermodynamics-guided alloy design and phase stability in CoCrFeMnNi-based medium-and high-entropy alloys: An experimental-theoretical study. **Scripta materialia (IF = 5.6)**, v. 252, p. 116264, 2024. Available at: <https://doi.org/10.1016/j.scriptamat.2024.116264>.

SUBJECT INDEX

Pág.

CHAPTER 1 – Introduction

1.1 Introduction to the central problem

For millennia, humanity has sought to improve its knowledge of metallurgy. In antiquity, the discovery of new metals and new metal alloys was responsible for great technological leaps [1]. Currently, the search for new compositions and processing routes that present good combinations of properties is still very relevant. At the beginning of the 21st century, a new strategy for developing metallic alloys became popular. The so-called multi-principal element alloys (MPEAs) or medium/high entropy alloys (M/HEAs) [1–4] represent this new concept: the idea of creating alloys using not only one principal element and a few alloying elements, but rather numerous principal elements. In this way, there is no longer a clear distinction between solvents and solutes. This new strategy expands the number of possible compositions to values never before imagined.

Based on studies with MPEAs, in the mid-2010s, the equiatomic CrCoNi alloy emerged with excellent combinations of mechanical properties, being classified as one of the toughest materials ever reported in the literature [5]. These CrCoNi alloys tend to exhibit a face-centered cubic (FCC) structure, but depending on the composition it may also exhibit other phases. Coury et al. (2018) [6] showed that increasing the Cr content up to ~40-45 at% increases the solid solution strengthening component, which improves the mechanical response of the material. In addition, they observed that increasing the Co content alters the active deformation mechanism: from mechanical twinning (TWIP effect) to strain-induced phase transformation (TRIP effect), in which the FCC matrix partially transforms into a hexagonal close packed (HCP) phase when the alloy is deformed, in addition to the dislocation slip. Based on these findings, the $Cr_{40}Co_{40}Ni_{20}$ alloy (richer in Cr and Co than the equiatomic CrCoNi) was proposed. Bertoli et al. (2021) [7] observed that this alloy also has an excellent combination of mechanical properties, and it stands out for having a high grain refinement strengthening component and presenting the TRIP effect.

In other words, the $Cr_{40}Co_{40}Ni_{20}$ alloy has a high potential for strengthening through grain refinement and exhibits strain-induced phase transformation (TRIP effect), which in turn provides greater ductility. Some studies suggest that the grain

refinement increases the “apparent or effective” stacking fault energy (SFE), which potentially modify the characteristics and/or type of deformation mechanisms, disfavoring or even inhibiting the TRIP/TWIP effects [8–10], but this correlation is not yet fully understood in the literature. Therefore, there is a need for a more in-depth understanding of how the TRIP effect is impacted by grain refinement, due to the importance that both mechanisms have in different alloys, especially in the $Cr_{40}Co_{40}Ni_{20}$ MPEA [7]. Chapter 2 of this work uses *in situ* tensile tests with synchrotron radiation in order to evaluate the activation and evolution of the TRIP effect in samples with different grain sizes, and to understand if grain size alone has the potential to modify the deformation mechanisms in a CrCoNi alloy.

Furthermore, one of the major challenges in the development of new alloys is to improve mechanical strength without significant losses in ductility, and one possible solution is through grain refinement. It is known that interstitial elements, such as C and N, are capable of inducing grain refinement through the Zener pinning mechanism when precipitates form [11,12]. On the other hand, it is still unclear if C and N atoms in solute form are effective in microstructural refinement. A recent review paper about grain growth in HEAs [11] states that the exploration of solute atoms to inhibit grain growth seems to be an interesting research front in future studies. For the solute drag effect of C and N, there are some reports indicating negligible effects [13–15], while some others showed their noticeable effect [16–19], which necessitates more research in this field. Therefore, this work also evaluates the use of interstitial elements as microstructural refiners in the $Cr_{40}Co_{40}Ni_{20}$ alloy, which should be especially advantageous, since grain refinement is a very effective strengthening mechanism for the alloy in question [7].

However, the effect of these interstitial elements is not limited to grain refinement, small additions of interstitial elements typically have a strong influence on phase equilibria, solid solution strengthening, precipitation strengthening (in the case of carbides or nitrides), SFE which in turn can alter deformation mechanisms (TRIP/TWIP effects), etc. The combination of these factors can drastically modify the properties and performance of these alloys [2,12]. Chapter 3 of this work first assesses the effect of C and N additions on phase equilibria and grain refinement capacity, using the $Cr_{40}Co_{40}Ni_{20}$ composition as Base alloy.

According to review papers [12,20], the influence of C- and N-doping on the SFE and TRIP/TWIP deformation mechanisms is still controversial in the literature, and the related explanation is not completely convincing. So, there is a need for a more in-depth understanding of how the SFE and TRIP effect are impacted by C- and N-doping, since this addition represents an important microstructural refinement route, and it modifies an important deformation mechanism (TRIP) of the $Cr_{40}Co_{40}Ni_{20}$ alloy. Chapter 4 of this work assesses the effect of C and N additions on the strain-induced FCC to HCP phase transformation (TRIP effect) and its reverse transformation from HCP to FCC during heating (martensitic reversion), using the $Cr_{40}Co_{40}Ni_{20}$ composition as Base alloy.

Altogether, the central question of this thesis can be summarized as follows: how grain refinement and interstitial alloying (C and N) interact with each other and with the TRIP effect in low SFE alloys as the $Cr_{40}Co_{40}Ni_{20}$ MPEA, and how these interactions can be exploited to design alloys with a desired combination of properties?

1.2 Objectives and chapter summary

The central objective of this thesis is to evaluate the interplay between grain size, TRIP effect, and interstitial doping in the $Cr_{40}Co_{40}Ni_{20}$ alloy. In the next chapters, three interactions are evaluated:

i) In Chapter 2, the effect of grain size on the TRIP deformation mechanism;

ii) In Chapter 3, the effect of C and N interstitial doping on phase equilibria and grain size;

iii) In Chapter 4, the effect of C and N interstitial doping on the TRIP deformation mechanism (FCC to HCP transformation) and its reversion during heating (HCP to FCC).

Further details regarding the objective, methodology, and main conclusions of each chapter are shown in the paragraphs below.

In Chapter 2, different grain sizes of the $Cr_{40}Co_{40}Ni_{20}$ MPEA are analyzed through *in situ* synchrotron X-ray diffraction (SXRD) during tensile testing, with the goal of following the FCC to HCP strain-induced transformation (i.e., TRIP effect) and

its impact on the mechanical behavior. It is possible to conclude that the critical stress for TRIP is proportional to the grain refinement strengthening, and grain size has no obvious influence on TRIP effect in terms of strain. This work also supports a Hall-Petch-based model and provides a mechanistic picture of the influence of FCC grain size on the onset and evolution of the strain-induced transformation of FCC to HCP.

In Chapter 3, different C- and N-doped alloys are designed, produced, thermomechanically treated under different conditions, and analyzed by X-ray diffraction (XRD) and scanning electron microscopy with electron backscatter diffraction (SEM-EBSD), in order to evaluate the effect of C and N on phase equilibria, microstructure, precipitate formation, grain size, and grain size distribution at different conditions, as well as on the grain growth kinetics. In short, C-doping promotes the formation of $M_{23}C_6$ precipitates, which was highly effective in inducing grain refinement through the pinning mechanism, while N-doping does not promote the formation of nitrides, but also induces grain refinement to a lesser extent.

In Chapter 4, C- and N-doped alloys are studied under cold deformation and continuous heating to evaluate the strain-induced martensite transformation (TRIP effect), the SFE, the martensite reversion during annealing, the recrystallization and grain growth temperatures, and the influence of C and N interstitial elements on these features. The XRD and SEM-EBSD analyses in deformed samples (cold-rolled) revealed the occurrence and extent of the TRIP effect by measuring the fraction of martensite HCP phase formed. *In situ* SXRD analyses during heating provided data to evaluate the martensite reversion by measuring the phase fraction along continuous heating, and to evaluate the recrystallization and grain growth temperature through the dislocation density quantification and the texture of FCC Debye-Scherrer rings along the azimuthal angle (using coefficient of variation). In conclusion, both C- and N-doping affect the extent of the TRIP effect by altering the SFE. The N addition disfavors the TRIP effect, while C addition does not show monotonic behavior, but higher C levels also disfavors TRIP effect. For these low SFE alloys, the martensitic HCP phase is transformed back into the FCC phase during heating (martensite reversion) by recrystallization of the FCC matrix, and not by a displacive or diffusional HCP to FCC transformation before recrystallization.

Finally, Chapter 5 presents the general discussion and conclusions of this thesis, including the overall answer to the problem stated in Chapter 1, based on what was presented in Chapters 2-4, as well as the main scientific, methodological, and technological contributions of this thesis.

CHAPTER 2 – Influence of grain size on strain-induced phase transformation

2.1 Introduction

MPEAs have significantly increased the number of potential compositions of metallic alloys to unprecedented levels and are being widely studied recently, driving the development of alloys with optimized properties and the in-depth study of different mechanisms [1–4]. The equiatomic CrCoNi MPEA stands out in this research field as one of the toughest materials ever reported [5], mainly due to its high solid solution strengthening component and to the formation of nanoscale mechanical twins, resulting in the twinning induced plasticity (TWIP) effect [5,6,21,22].

Our research group recently designed the non-equiatomic $Cr_{40}Co_{40}Ni_{20}$ MPEA [7,23], which maintains the same solid solution strengthening component as the equiatomic alloy (~250 MPa) [7,24]. In addition, this non-equiatomic MPEA has lower SFE (11.8 mJ/m²) [7], when compared to the equiatomic TWIP CrCoNi alloy (18 to 22 mJ/m²) [21,25]. So, the non-equiatomic $Cr_{40}Co_{40}Ni_{20}$ alloy presents a strain-induced phase transformation, responsible for the transformation induced plasticity (TRIP) effect, in which the FCC matrix partially transforms into nanometric lamellae of a HCP phase when the alloy is deformed [7]. The TRIP effect provides high work-hardening capacity and ductility [21,26–29]. Despite this, it is desirable to improve its mechanical strength with minimal losses in ductility and toughness, which can potentially be achieved through grain refinement [26,27,30]. The $Cr_{40}Co_{40}Ni_{20}$ MPEA has a high grain refinement strengthening component compared to similar alloys [7], which means that grain refinement is an efficient way to improve the mechanical strength of this alloy. Furthermore, TRIP alloys have the advantage of obtaining more refined grains after cold rolling and annealing [28,29,31], which makes the alloy even stronger. In short, the TRIP effect and grain refinement are important mechanisms for adjusting mechanical properties in the current alloy, therefore it is essential to understand the influence that one has on the other, since this relationship is not yet fully understood in literature.

Some studies have shown that grain refinement strongly affects deformation mechanisms, disfavoring or even inhibiting TRIP/TWIP effects [8–10]. According to these studies, this behavior is related to the SFE, although it is not entirely clear how grain size affects SFE and there are few reports about this relation [32–34].

Furthermore, it is known that SFE is a key parameter to control and predict deformation mechanisms: only dislocation slip is expected for high SFE alloys (>45 mJ/m²), TWIP effect is activated for low/medium SFEs (15 to 45 mJ/m²), and TRIP is activated for very low SFEs (<15 mJ/m²) [28,29,31,35–37]. In short, the literature suggests that the grain refinement increases the "apparent or effective SFE", which potentially modify the characteristics and/or type of deformation mechanisms, disfavoring or even inhibiting the TWIP and/or TRIP effects.

A better understanding of the relation between grain size and TRIP effect is essential for the proper adjustment of mechanical properties, as grain size and TRIP effect have a synergistic effect, and both have a strong influence on mechanical strength and ductility. Knowing how much it is possible to take advantage of grain refinement without compromising the occurrence of the TRIP effect is valuable information, but it varies significantly depending on the alloy system studied. Furthermore, in studies with MPEAs, TRIP alloys are considerably less studied than TWIP alloys, since most studies focus on the CrCoNi and Cantor's alloy, both TWIP alloys. Therefore, there is a need for a more in-depth understanding of how the TRIP effect is impacted by grain refinement, due to the importance that both mechanisms have in different alloys, especially in the $Cr_{40}Co_{40}Ni_{20}$ MPEA [7].

2.1.1 Objectives

In the current work, different grain/crystallite sizes of the $Cr_{40}Co_{40}Ni_{20}$ MPEA were analyzed through *in situ* SXRD during tensile testing, with the goal of following the FCC to HCP strain-induced transformation (i.e., TRIP effect) and its impact on the mechanical behavior. This work also supports a Hall-Petch-based model and provides a mechanistic picture of the influence of FCC grain/crystallite size on the onset and evolution of the strain-induced transformation of FCC to HCP.

2.2 Literature review

2.2.1 CrCoNi system alloys

Based on numerous studies in the field of MPEAs, it has been observed that the equiatomic CrCoNi alloy stands out in comparison to similar alloys with an FCC structure. This alloy exhibits excellent combinations of mechanical strength and ductility at room temperature and has even better properties at cryogenic temperatures. [21,25,38–42]. Gludovatz et al. (2016) [5] showed that the equiatomic CrCoNi alloy qualifies as one of the toughest alloys ever reported among all materials. Its good mechanical properties are mainly attributed to the high solid solution strengthening component [6,22], and the occurrence of twinning induced plasticity (TWIP) effect [5,21]. More recent studies [23] discuss that both the strengthening components and the deformation mechanisms involved are fundamental to explaining, predicting, and optimizing the mechanical properties, especially the toughness, of CrCoNi alloys.

In the CrCoNi system, the solid solution strengthening component *(*$\Delta\sigma_{SS}$) can be improved by adding Cr: $Cr_{45}Co_{27.5}Ni_{27.5}$ [6] and $Cr_{40}Co_{30}Ni_{30}$ [43] alloys (richer in Cr) exhibit even greater mechanical strength and toughness than the equiatomic CrCoNi alloy. It is also observed that Cr plays an essential role in corrosion resistance, which is also a prominent aspect of this alloy system [44]. However, the addition of Cr and Co must be carefully planned, as it favors the formation of sigma phase [6,24], which can be detrimental to mechanical properties due to its brittleness [45]. Furthermore, the formation of sigma phase may cause the removal of Cr from the FCC matrix, which can decrease corrosion [44] and oxidation [46] resistance.

Regarding deformation mechanisms, mechanical twinning (TWIP effect) occurs in alloys in the central region of the CrCoNi diagram: such as the equiatomic CrCoNi [5,21,25], and the quasi-equiatomic $Cr_{45}Co_{27.5}Ni_{27.5}$ [6] and $Cr_{40}Co_{30}Ni_{30}$ [43]. Some studies involving these alloys [42,43,47,48] observed local phase transformation, in which the FCC phase transforms into the hexagonal close-packed (HCP) phase along stacking faults and deformation twins. This occurs only in more advanced stages of deformation and, unlike conventional TRIP, where the transformation occurs on a large scale, in these alloys only a very small fraction of HCP phase is observed with a thickness on the order of a few atomic layers.

From the center of the CrCoNi diagram, the addition of Co decreases the SFE [24,49], in other words, it increases the thermodynamic driving force for the formation of an HCP phase. Consequently, the tendency of the deformation mechanisms is altered, favoring the FCC to HCP strain-induced transformation, also known as transformation induced plasticity (TRIP) effect [7,24,49].

Bertoli et al. (2021) [7] studied the $Cr_{40}Co_{40}Ni_{20}$ composition, an alloy richer in Cr and Co than the equiatomic CrCoNi. As shown in Figure 2.1(a), this alloy also has excellent combinations of mechanical properties, reaching a yield strength greater than 600 MPa, a tensile strength greater than 1 GPa, while maintaining a ductility of around 50%. It is noteworthy that the $Cr_{40}Co_{40}Ni_{20}$ alloy exhibits a higher grain refinement strengthening component ($\Delta\sigma_{RG}$) than other similar MPEAs, as it has higher Hall-Petch coefficients (σ_0 and K_{HP}), as shown in Figure 2.1(b). Bertoli et al (2021) [7] also observed that grain growth is relatively slow in this alloy, providing a refined grain microstructure after conventional heat treatments. Furthermore, it is estimated that the solid solution strengthening component ($\Delta\sigma_{SS}$) is as high as that of the equiatomic CrCoNi alloy, on the order of 250 MPa [7,24]. The acting deformation mechanism alters to the TRIP effect, in which the FCC matrix partially transforms into a strain-induced HCP phase, which exhibits lath morphology and nanometric thickness (between ~5 and 20 nm), as shown in Figures 2.1(c,d). This alloy exhibits a high work hardening capacity, even at high stress levels, which provides high ductility. Considering its promising mechanical response in different aspects, the $Cr_{40}Co_{40}Ni_{20}$ MPEAs was selected as the object of study for this work.

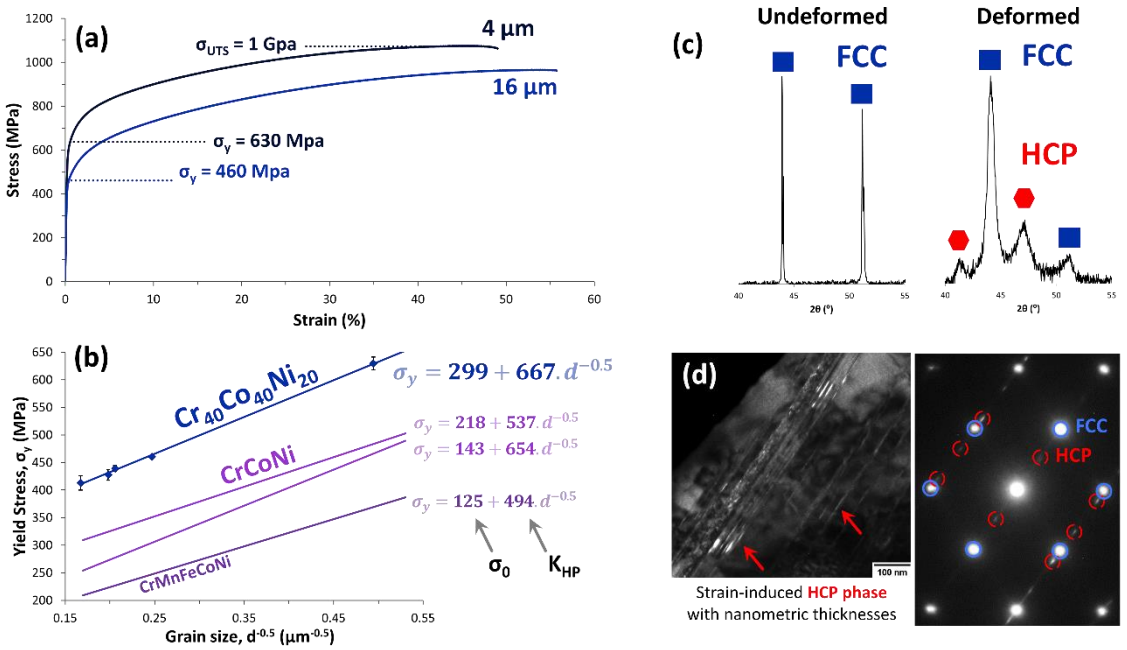

Figure 2.1: (a) Engineering stress-strain curves for $Cr_{40}Co_{40}Ni_{20}$ alloy. (b) Hall–Petch plot relating yield stress (σ_y) and FCC grain size (d) (excluding twin boundaries) of $Cr_{40}Co_{40}Ni_{20}$ alloy compared to similar alloys. (c) XRD patterns of recrystallized and deformed (taken from within the gauge length of a tensile test with ~50% of strain) samples. (d) Transmission electron microscopy (TEM) analysis of a deformed sample: dark field (DF) acquired using the $\{01\text{-}10\}_{HCP}$ reflection and selected area diffraction pattern from <110>/<2-1-10> zone axis. Adapted from [7].

2.2.2 Deformation mechanisms and stacking fault energy

The high ductility and toughness of CrCoNi alloys are attributed, among other factors, to the TWIP/TRIP deformation mechanisms. It is important to clarify that, even in TWIP/TRIP alloys, dislocation slip is still the basic and dominant mechanism of plastic deformation. Other mechanisms such as TWIP and TRIP, when activated during deformation, do not replace dislocation slip, in fact, they complement it and make it more efficient, increasing the work hardening rate and ductility [35].

Alloys in the central region of the CrCoNi diagram, such as the equiatomic CrCoNi [5,21,25], $Cr_{45}Co_{27.5}Ni_{27.5}$ [6], and $Cr_{40}Co_{30}Ni_{30}$ [43], exhibit strain-induced twinning (TWIP effect - twinning induced plasticity), i.e., the formation of twins of nanometric thickness during deformation.

Adjusting the SFE, it is possible to control the deformation mechanisms [28,35,36]. Co addition in CrCoNi alloys decreases the SFE [7,28,49], culminating in alloys as $Cr_{40}Co_{40}Ni_{20}$ [7] e $Cr_{40}Co_{55}Ni_5$ [24] that exhibit strain-induced phase transformation (TRIP effect - transformation-induced plasticity), where the FCC matrix phase partially transforms into an HCP phase. HCP phase forms with a fine and elongated morphology, like needles or plates, and typically presents the orientation $<110>_{FCC}//<11\text{-}20>_{HCP}$; $\{111\}_{FCC}//\{0001\}_{HCP}$ [42,47,48], which corresponds to the alignment of the close-packed planes and directions of both structures.

The formation of mechanical twins (TWIP) and the HCP phase (TRIP) during deformation can be understood as the propagation of a stacking fault along close-packed planes. In more detail: in FCC metals with low SFE, a 1/2<110>{111} perfect dislocation dissociates into a pair of 1/6<112>{111} Shockley partial dislocations, so that the first partial dislocation alters the crystal stacking and the second repairs it, creating a stacking fault in the region between the partials [50]. As shown in Figure 2.2, starting from the FCC structure (...ABC ABC... stacking): the passage of a set of partial dislocations in consecutive {111} close-packed planes generates a twin (...A/C/B/A/C/B... stacking); while the passage of partials every 2 {111} planes generates HCP phase (...AB/AB/AB... stacking) [47,51,52].

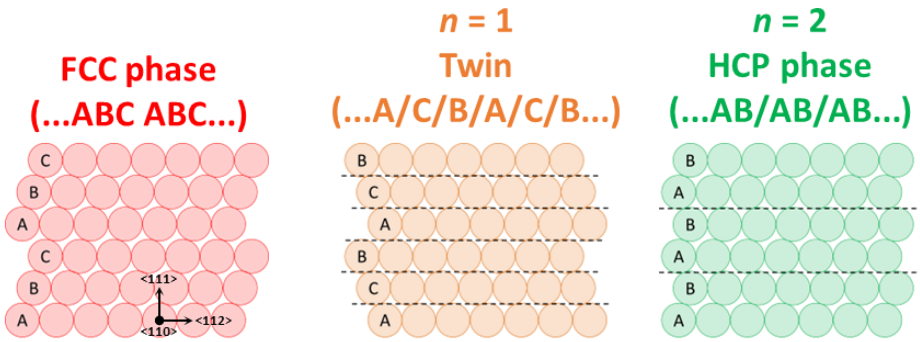

Figure 2.2: From the FCC structure, the presence of stacking faults (/) every n {111} close-packed plane generates the twin structure (for n=1) and the HCP phase (for n=2).

During deformation, both deformation twins (resulting from the TWIP effect) and HCP phase lamellae (resulting from the TRIP effect) act as extra barriers to dislocation slip, which is known as the dynamic Hall-Petch effect. These additional mechanisms, besides dislocation slip, provide greater work hardening capacity to these alloys. It is known from the Considère criterion that plastic instability due to necking

occurs approximately when the work hardening rate decays to the point of equaling the true stress ($d\sigma_{tr}/d\varepsilon_{tr} = \sigma_{tr}$), thus the high work hardening rate provided by the TRIP/TWIP effects delays plastic instability, considerably increasing ductility, and consequently allowing these alloys to withstand higher stresses before failing [5,21,26–28].

There is no consensus in the literature, but there are indications that TRIP alloys of the CrCoNi system have a higher strain hardening rate than TWIP alloys [52,53]. Considering that the HCP phase is presumably more resistant to dislocation slip than the FCC phase, due to the smaller number of slip systems, HCP lamellae are probably more difficult to be traversed by dislocations than deformation twins.

As mentioned earlier, the SFE influences the acting deformation mechanisms [28,35,36]. The SFE quantifies the energy difference between the faulted region and the ideal crystal, already considering the interfaces formed [50]. Considering CrCoNi alloys that have a high-temperature FCC field and a lower-temperature HCP field, the SFE represents the stability between the FCC and HCP phases, plus the energy required to create new FCC/HCP interfaces.

It is understood that zero or negative SFE values indicate that stacking faults are more stable than the FCC matrix and that partial dislocations tend to separate indefinitely. This phenomenon is physically interpreted as the formation of martensitic HCP phase during cooling. Thus, the temperature at which SFE is zero indicates the martensite start temperature (M_S) [36,51].

In metastable FCC crystals, those with very low SFE (< ~15 mJ/m² [35]), the HCP phase is slightly more stable than the FCC phase, but the martensitic transformation (FCC to HCP) does not spontaneously happen since there should be an additional driving force to overcome the formation of the FCC/HCP interfaces. In this case, the alloy usually presents a strain-induced HCP phase when subjected to mechanical stress, which characterizes the TRIP effect [35,36,51].

For higher SFE, the FCC phase becomes more stable than the HCP, disfavoring the TRIP effect. There is an SFE range (15~45 mJ/m² [35]) in which the HCP phase is too unstable to form, but the partial dislocations are still too far apart, which hinders the recombination of the partials and cross-slip of the dislocations; in this SFE range, mechanical twinning (TWIP effect) is activated. For even higher SFE (> ~45 mJ/m²

[35]), the partial dislocations are close enough, facilitating cross-slip, so both TRIP and TWIP effects are suppressed at the expense of dislocation slip [35].

Several factors potentially influence the SFE and deformation mechanisms, some of them have an impact on the relative stability between the FCC and HCP phases, on the SFE in fact, others have an impact on the force balance between the Shockley partial dislocations, that is, on the "apparent SFE". Some of them include: alloy composition [54–58], local composition in the vicinity of the stacking fault [59–61], as well as temperature, and short-range order.

Higher temperatures increase the SFE in CrCoNi alloys [47,62], which reduce the driving force for the FCC to HCP transformation, decreasing the extent of the strain-induced transformation [63].

The short-range order (SRO) is another factor that can impact SFE and TRIP/TWIP deformation mechanisms [60,64–67], although SRO seems to have no effect on strength [68]. SRO consists of a slight preference for unlike atoms in the first neighbors [69–71] and leads to a considerable increase in SFE: an increase of up to 70 mJ/m² (-42 to 30 mJ/m²) was observed through simulations [60,64], and up to 15 mJ/m² (8 to 23 mJ/m²) experimentally [65]. Basically, SRO reduces the Gibbs free energy of the FCC phase (ΔG^{FCC}), increasing the energy difference between the FCC and HCP phases ($\Delta G^{FCC\text{-}HCP}$), which explains the increase in SFE when it is considered.

2.2.3 Influence of grain size on stacking fault energy and deformation mechanisms

Grain/crystallite size is another factor that potentially alters SFE. There are few studies that address the direct relation between grain size and SFE, and therefore this relation is not fully understood. Despite this, the previous relation is reinforced by the fact that there are numerous studies showing that grain size strongly affects deformation mechanisms, in which grain refinement disfavors or even inhibits TRIP/TWIP effects [8–10]. In addition, there is a consensus in the literature that SFE is directly related to the acting deformation mechanisms, both in steels and in MPEAs with FCC structure [28,29,31,35–37]. Therefore, grain refining supposedly increases SFE, which hinders or even inhibits TWIP and/or TRIP effects.

Regarding the few studies that investigate the relation between grain size and SFE, Jun e Choi (1998) [72] and Takaki, Nakatsu e Tokunaga (1993) [73] observed that grain refinement leads to an increase in SFE in steels, which is more pronounced for grain sizes smaller than ~30 μm [32,72]. In these studies, the SFE was estimated from the decrement of M_S temperature with grain refinement.

According to these studies, when considering this increase in SFE due to grain refinement, the parameter is now called "effective or apparent SFE" (SFE_{app}), and can be calculated for austenitic steels using Equations 2.1 and 2.2 [32], where SFE_0 is the SFE of the material without considering the grain size; ρ is the planar density of the {111} planes; a is the lattice parameter; N is Avogadro's constant; and d is the grain size.

$$SFE_{app} = SFE_0 + 2\rho\, 170.06 \exp\left(\frac{-d}{18.55}\right) \quad \textbf{Eq. 2.1}$$

$$\rho = \frac{4}{\sqrt{3}\, a^2\, N} \quad \textbf{Eq. 2.2}$$

The SFE_0 of the $Cr_{40}Co_{40}Ni_{20}$ alloy is approximately 11.8 mJ/m² [7], within the SFE range where the TRIP effect is expected (SFE < ~15 mJ/m²) [35]. Using Equations 2.1 and 2.2 [32] for the current alloy and extrapolating to a grain size tending towards zero, a maximum SFE increment of 10.25 mJ/m² is obtained due to grain refinement. It shows that grain refinement does not significantly increase SFE, although it may alter the acting deformation mechanisms on some alloys.

2.3 Experimental Procedure

2.3.1 Alloy production and thermomechanical processing

A 2 kg ingot (20x40x300 mm) of the $Cr_{40}Co_{40}Ni_{20}$ (at. %) alloy was produced with commercially pure elements (>99.7%) by vacuum induction melting with non-forced cooling using an alumina crucible. The ingot was homogenized at 1100 ºC for 2 hours, and the thickness was gradually reduced by several hot rolling steps to a final thickness of ~1.7 mm at around 1100 ºC. The plate was cold rolled up to a final thickness of ~1.0 mm (final cold rolling thickness reduction of ~40%). Tensile test

specimens were obtained by electrical discharge machining, a schematic of the sample geometry is provided in the supplementary material (Section S1). Samples were recrystallized under four different conditions (1: 800 ºC/20 min; 2: 900 ºC/30 min; 3: 1000 ºC/2 h; 4: 1100 ºC/2 h) to obtain four different grain/crystallite sizes, followed by water quenching. The heat treatment conditions were chosen based on the grain growth kinetics of the $Cr_{40}Co_{40}Ni_{20}$ alloy, studied by Bertoli et al. (2021) [7].

2.3.2 Sample preparation and grain/crystallite size counting

Scanning electron microscopy (SEM) with electron backscatter diffraction (EBSD) analyses were performed on the recrystallized and deformed samples, in the grip section and in the gauge length, respectively, after the tensile tests. The loading direction is oriented vertically in the microscopy images. The EBSD maps were post-processed in the EDAX OIM Analysis™ software using the "grain dilation" cleanup routine, with the parameters adjusted according to the magnification and step size (spatial resolution) used in each analysis. Samples were carefully prepared according to standard metallographic preparation, up to a final stage of at least 15 h in a vibratory polisher with a 0.04 μm colloidal silica suspension. This stage is important in TRIP alloys for removing any transformed phase layer from the surface region formed in the cutting and grinding processes.

In the recrystallized samples, the grain size d (excluding annealing twin boundaries) and the crystallite size c (accounting for both grain and annealing twin boundaries) were determined for the FCC phase, as the contribution of annealing twins to alloy strength is still a matter of debate in the literature [74]. Calculations, simulations and experimental observation of dislocation pile-up against annealing twins suggest that those twins influence the alloy strength [75–78]. The initial FCC grain/crystallite size were obtained by the intercept procedure, according to the ASTM E112 standard [79]. The presented grain and crystallite size values are the average value and standard deviation obtained from four fields in each condition, using ten horizontal and ten vertical lines per field.

2.3.3 *In situ* synchrotron X-ray diffraction during tensile testing

In situ SXRD was performed during uniaxial tensile testing at Sector 1-ID at the Advanced Photon Source (APS), Argonne National Laboratory, IL, USA, at room temperature with a constant strain rate of $2x10^{-4}$ s^{-1}. A monochromated 71.6 KeV high-energy beam was used, with a corresponding wavelength of 0.1731 Å. This high photon energy allowed to perform diffraction experiments in transmission mode in relatively thick samples, enabling the determination of bulk microstructural information. CeO_2 powder was used as a standard for the calibration of the instrument parameters and to determine the sample-to-detector distance, which was calculated to be 2129 mm. Four GE-41RT area detectors were used to capture the 2D raw Debye-Scherrer rings at different stress/strain levels. Each diffraction pattern was obtained through the summation of 10 individual images with an exposure time of 0.3 s. A dark image was recorded before each test for background subtraction. The 2D Debye-Scherrer rings were converted into conventional 1D intensity vs 2θ diffraction patterns by integrating along the full azimuthal angle (φ range from 0 to 360°) and the 10° transverse direction (TD) (φ range from -5 to 5°) using the General Structure Analysis System (GSASII) software [80]. Peaks were individually fitted by a pseudo-Voigt function to determine key peak parameters such as peak position, peak intensity, full width at half maximum (FWHM), and area under the peak.

The FCC dislocation density was determined by the modified Williamson-Hall method using the 10° TD integration data (as it develops less texture) from five FCC peaks (111, 200, 220, 311, and 222), after subtracting the instrumental broadening via the CeO_2 standard. More details about the methodology for calculating dislocation density via the modified Williamson-Hall method can be found in the supplementary material (Section S2).

2.3.4 Phase fraction quantification

The HCP phase fraction was quantified by two methods: via EBSD and via SXRD. The first consists of the area fraction obtained via EBSD analyses of the deformed samples, which reports only the maximum (final) fraction for each sample. The second one consists of calculating the volumetric fraction of the HCP phase

through the diffractograms obtained via SXRD and reports the fraction of phases throughout the entire tensile test. The calculation via SXRD was performed through Equation 2.3, where A is the experimental integrated intensity for hkl plane, also understood as the area below the hkl peak; I is the theoretical relative integrated intensity for hkl plane (Equation 2.4); and n is the number of peaks examined. Five FCC peaks (111, 200, 220, 311, and 222) and four HCP peaks (10-10, 10-11, 10-12, and 10-13) were considered. The full integration data (φ range from 0 to 360°) was used so that the full intensity of each peak was evaluated.

$$f_{HCP} = \frac{\frac{1}{n}\sum_{j=1}^{n}\frac{A_{HCP}^{j}}{I_{HCP}^{j}}}{\frac{1}{n}\sum_{j=1}^{n}\frac{A_{HCP}^{j}}{I_{HCP}^{j}} + \frac{1}{n}\sum_{j=1}^{n}\frac{A_{FCC}^{j}}{I_{FCC}^{j}}} \quad \textbf{Eq. 2.3}$$

The theoretical relative integrated intensity (I) was obtained using Equation 2.4, where V is the volume of the unit cell (m³), $|F|$ is the structure factor, p is the multiplicity factor, and the term in parentheses is the Lorentz-polarization factor, which depends on the diffraction angle (θ).

$$I = \left(\frac{1}{V^2}\right)|F|^2 p\left(\frac{1+cos^2 2\theta}{sin^2\theta\, cos\theta}\right) \quad \textbf{Eq. 2.4}$$

2.4 Results

2.4.1 Microstructural characterization of recrystallized samples

SEM-EBSD analyses were performed on the recrystallized samples to assess their microstructure, phases and average grain/crystallite size. Figures 2.3(a-d) show the microstructure of the recrystallized samples with FCC grains and annealing twins. Table 2.1 compiles the FCC average grain size and crystallite size for each sample. Figure 2.3(e) shows that all samples have a monomodal grain size distribution. Figure 2.3(f-g) show the misorientation angle distribution and coincidence site lattice (CSL) boundaries fractions as a function of total high-angle boundaries length. The frequency of Σ3 (60°) annealing twin boundaries increases with increasing grain size, as expected for low SFE alloys due to the extensive twinning during grain growth [81]. The number of annealing twin boundaries per grain, shown in Table 2.1, also reinforces this point. The Σ9 (39°) is

the second most frequent CSL boundary, it can be formed by the intersection of two Σ3s [82]. EBSD and SXRD analyses revealed approximately 0.5% of sigma phase precipitates in samples 1 and 2, as shown in the supplementary material (Section S3). The small fraction of sigma phase is considered to not significantly alter the FCC matrix composition nor the mechanical strength of the samples. The precipitation strengthening component was estimated using Ashby-Orowan equation, as shown in the supplementary material (Section S4), and it can be considered negligible as it represents less than 2% of the yield stress in samples 1 and 2.

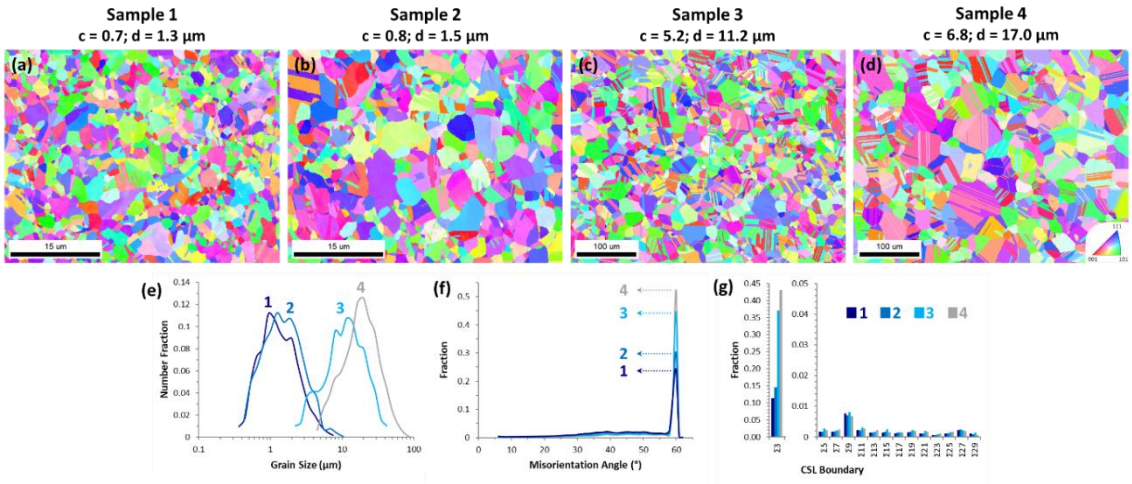

Figure 2.3: (a-d) SEM-EBSD (inverse pole figure) images of recrystallized samples with different grain sizes, *d*, and crystallite sizes, *c*. (e) Grain size distribution. (f) Misorientation angle distribution and (g) CSL boundaries fractions as a function of total high-angle boundaries length.

2.4.2 *In situ* synchrotron X-ray diffraction during tensile testing

Samples with different grain/crystallite sizes were analyzed by *in situ* SXRD during tensile testing, as shown in Figure 2.4, to evaluate their mechanical behavior and the evolution of the strain-induced phase transformation. Figure 2.4(a) shows the stress-strain curves, and Figure 2.4(b) shows the Hall-Petch plot correlating the yield stress (σ_y) and the grain size (d)/crystallite size (c). Mechanical properties are compiled in Table 2.1. Samples 1 and 2 (smaller grain/crystallite size) are much stronger than samples 3 and 4 (larger grain/crystallite size), and despite the drop in fracture strain, samples 1 and 2 still show good ductility, around 40%. Comparing the yield strength

(σ_y), sample 1 (~830 MPa) is twice as strong as samples 3 and 4 (~410 MPa). This increase in yield strength occurs mainly due to grain refinement strengthening, since the solid solution strengthening is the same for all samples and precipitation strengthening is negligible.

Table 2.1: Sample identification, heat treatment conditions, grain and crystallite size (average value and standard deviation), annealing twin boundaries per grain, mechanical properties, and final HCP fraction obtained by both SXRD (in the last diffractogram) and EBSD (in the fratured sample) methods.

Sample	*Heat treatment conditions*	*FCC average grain size, d (μm)*	*FCC average crystallite size, c (μm)*	*Annealing twin boundaries per grain, n = (d/c)-1*	*Yield strength, $\sigma_{y\ 0.2\%}$ (MPa)*	*Ultimate tensile strength, σ_{UTS} (MPa)*	*Elongation at fracture, ε_f*	*Final HCP fraction via SXRD (last diffractogram) (%)*	*Final HCP fraction via EBSD (after fracture) (%)*
1	800 °C / 20 min	1.3 ± 0.3	0.7 ± 0.1	0.85	834	1095	0.41	33.5	36.7
2	900 °C / 30 min	1.5 ± 0.1	0.8 ± 0.02	0.98	737	1062	0.41	45.3	40.8
3	1000 °C / 2 h	11.2 ± 0.6	5.2 ± 0.5	1.16	409	884	0.75	51.9	50.3
4	1100 °C / 2 h	17.0 ± 0.9	6.8 ± 1.0	1.50	417	874	0.72	51.9	53.4

Figures 2.4(c-e) shows the evolution of the TRIP effect, that is, the formation of the HCP phase during deformation. In the initial condition (represented by Figure 2.4(d)), before the start of load application, all samples had 0% HCP phase. At the end of the test (represented by Figure 2.4(e)), marked by the fracture of the specimens, samples showed between 35 and 52% HCP phase, depending on the sample's grain/crystallite size. This result shows a partial FCC to HCP strain-induced phase transformation (relating to TRIP effect), while no evidence of mechanical twins (relating to TWIP effect) was observed by complementary analyses, in agreement with a study carried out with this same composition by Bertoli et al. (2021) [7]. The diffractograms of sample 3 are used in Figure 2.4(c-e) to illustrate the general behavior of all samples, and the diffractograms (colormaps) of the other samples are in the supplementary material (Section S5).

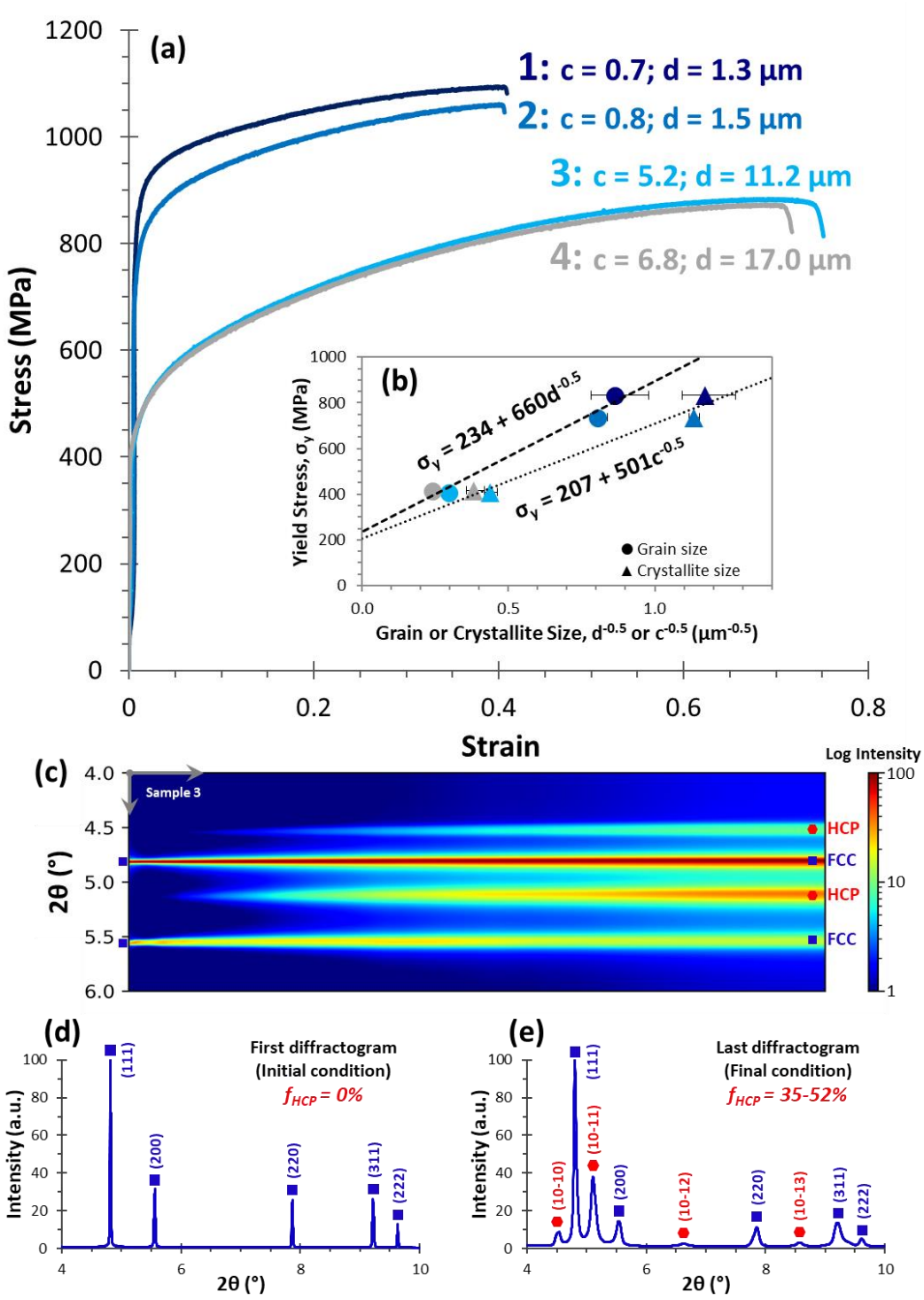

Figure 2.4: *In situ* SXRD during tensile testing of $Cr_{40}Co_{40}Ni_{20}$ alloy. (a) Engineering stress-strain curves of samples with different FCC grain sizes. (b) Hall-Petch plot for yield stress. (c) X-ray diffractogram throughout the tensile test vs strain, (d) first diffractogram, and (e) last diffractogram. The diffractograms of sample 3 are used in this figure to illustrate the general behavior of all four samples, which present a partial FCC to HCP strain-induced phase transformation, reaching 35 to 52% HCP phase, depending on the initial FCC grain/crystallite size.

2.4.3 Microstructural characterization of deformed samples

SEM-EBSD analyses were carried out on deformed samples, as shown in Figures 2.5(a-d) to assess their microstructure and the final phase fraction. Based on the phase distribution shown in this result and in a previous work with this same composition [7], it is noted that the HCP phase (in red) has a lamellar morphology that mostly crosses the original grains throughout their entire length.

From these EBSD analyses, it was possible to quantify the final phase fraction in order to validate the accuracy of the measurement via SXRD using the area under the peaks. Figure 2.5(e) show a comparison of the final HCP fraction obtained by both methods: EBSD in the fractured sample, and SXRD in the last diffractogram. This result is also listed in Table 2.1. The values obtained by both methods are close for each sample and follow the same increasing trend with increasing grain/crystallite size. The phase fraction analysis via EBSD has its limitations as it evaluates a relatively small and superficial region, however the proximity of the values between EBSD and SXRD reaffirms that the method used to calculate the phase fraction via SXRD proved to be accurate.

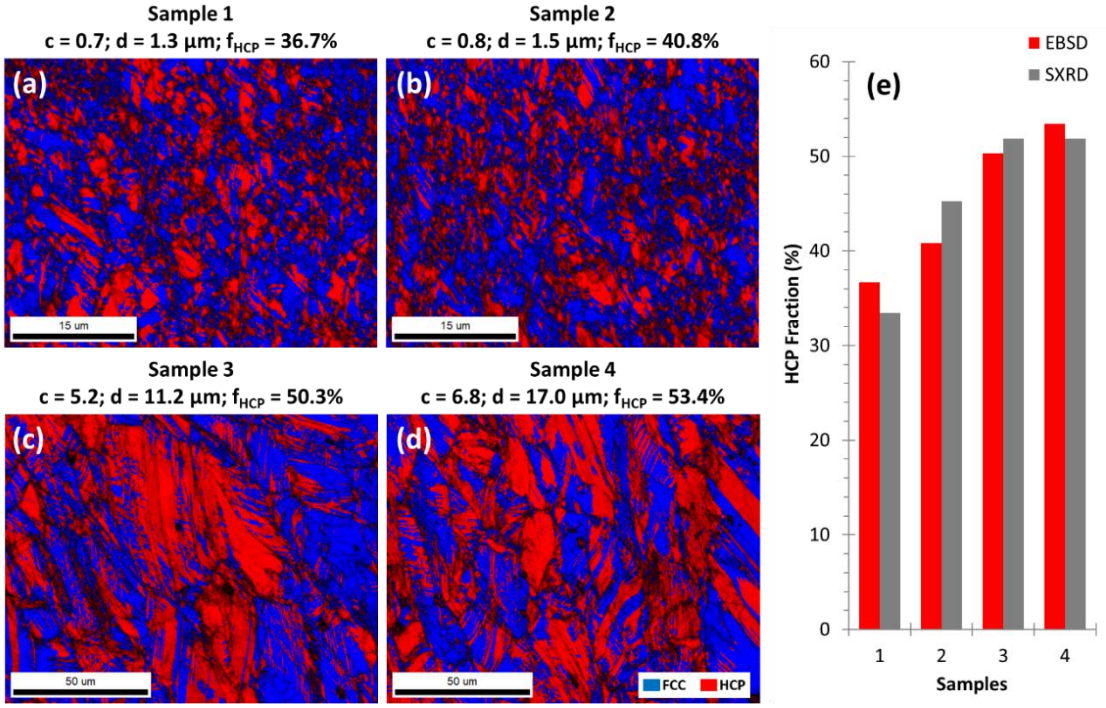

Figure 2.5: (a-d) SEM-EBSD (phases + image quality) images of deformed samples (fractured samples), and (e) comparison of the HCP phase fraction obtained via EBSD and via SXRD using the area under the peaks in the last diffractogram. The loading direction is oriented vertically in the microscopy images.

2.4.4 Modeling the correlation between HCP fraction, applied stress, and grain/crystallite size

From the *in situ* SXRD data obtained throughout the tensile test, it was possible to calculate the fraction of HCP phase formed at each instant of deformation. Figure 2.6(a) shows the HCP fraction as a function of the applied stress for various grain/crystallite sizes. At the beginning of the phase transformation, the HCP peaks exhibit similar intensities to the background noise, hindering their detection. As a result, reliable data begin to emerge between 3 and 6% of the HCP fraction, and the transformation onset is not accurately detected by the script programmed to find and fit the peaks.

In Figures 2.6(b1-b2), this data was plotted as follows: the critical stress required to form a certain fraction of HCP phase against the grain size ($d^{-0.5}$), and against the crystallite size ($c^{-0.5}$). An important finding is noteworthy: the evolution of the TRIP effect follows the classic Hall-Petch equation (Equations 2.5 and 2.6) in both cases. As expected, this relation also holds true for the yield stress, as shown in Figures 2.6(b1-b2). Furthermore, the Hall-Petch slope (the constant k) is approximately the same for the yield stress and for the TRIP evolution ($k_y \approx k_{TRIP}$: ~660 MPa/μm$^{-0.5}$ for grain size, and ~500 MPa/μm$^{-0.5}$ for crystallite size). Wagner and Laplanche (2023) [74] obtained a similar conclusion regarding the TWIP effect in the Cantor alloy (CrMnFeCoNi) where they reported that the uniaxial twinning stress, the TWIP onset, follows the Hall-Petch equation with the same Hall-Petch slope as for the yield stress ($k_y \approx k_{TWIP}$). Levitas (2023) [83] discussed the correlation between the Hall-Petch effect of the grain size on the minimum pressure for the strain-induced transformation, the TRIP onset in terms of pressure. Despite that, no documented correlation between the evolution of TRIP effect and Hall-Petch behavior, as our results show, was found in the existing literature.

$$\sigma_y = \sigma_0 + \frac{k_y}{\sqrt{d}} \quad or \quad \sigma_y = \sigma_0 + \frac{k_y}{\sqrt{c}}, \qquad \text{for dislocation slip} \qquad \textbf{Eq. 2.5}$$

$$\sigma_{TRIP} = \sigma_{TRIP,0} + \frac{k_{TRIP}}{\sqrt{d}} \quad or \quad \sigma_{TRIP} = \sigma_{TRIP,0} + \frac{k_{TRIP}}{\sqrt{c}}, \qquad \text{for TRIP effect} \qquad \textbf{Eq. 2.6}$$

Based on the findings shown in the previous paragraph, this work proposes a Hall-Petch-based model that describes the critical stress (σ_{TRIP}) required to form a certain fraction of strain-induced HCP phase (f_{HCP}), as a function of both the initial FCC grain size (d) and crystallite size (c). The development of the model will be presented below.

The first step was to perform a Hall-Petch fitting for different HCP fractions between 6.0 and 33.5% (in increments of 0.5%), where there are 4 points for the fitting, and obtaining the slope k_{TRIP} and the intercept $\sigma_{TRIP,0}$ for each dataset, as shown in the supplementary material (Section S6, Table S2).

Then, plotting the slope k_{TRIP} vs HCP fraction (Figures 2.6(c1-c2)), it is observed that slope k_{TRIP} presents an approximately constant value of 663.45 MPa/μm$^{-0.5}$ for grain size and 501.87 MPa/μm$^{-0.5}$ for crystallite size.

The next step is to plot the intercept $\sigma_{TRIP,0}$ vs HCP fraction (Figures 2.6(d1-d2)), it is observed that the HCP fraction presents a logistic or sigmoidal growth as a function of the $\sigma_{TRIP,0}$. This behavior is also clearly observed in our experimental curves of Figure 2.6(a). Phase transformations, including strain-induced ones, are commonly expressed by logistic or sigmoidal behavior [29]. In this case, the rate of phase transformation grows exponentially, until the rate gradually decreases, and the HCP fraction stabilizes at a plateau. A generalized logistic/sigmoidal curve for phase fraction (f_{HCP}) as a function of the applied stress (σ) can be expressed by the Equation 2.7.

$$f_{HCP} = A + \frac{K - A}{\sqrt[v]{1 + Qe^{-B\sigma}}} \quad \textbf{Eq. 2.7}$$

Where A is the lower asymptote (assumed to be equal to 0, because there is no HCP phase in the initial microstructure), B is the transformation rate, K is the upper asymptote, Q is a factor relating to the horizontal displacement (in the stress axis), and v describes the asymmetry of the curve. This function (Equation 2.7) was used to fit the HCP fraction (f_{HCP}) as a function of the $\sigma_{TRIP,0}$ data, as shown in Figures 2.6(d1-d2), with an initial guess of B = 0.001, K = 1, Q = -1, and v = -0.1, based on the shape of the experimental curves in Figure 2.6(a), and a coefficient of determination (R^2) equal to 99.87% was obtained for grain size and 99.86% for crystallite size.

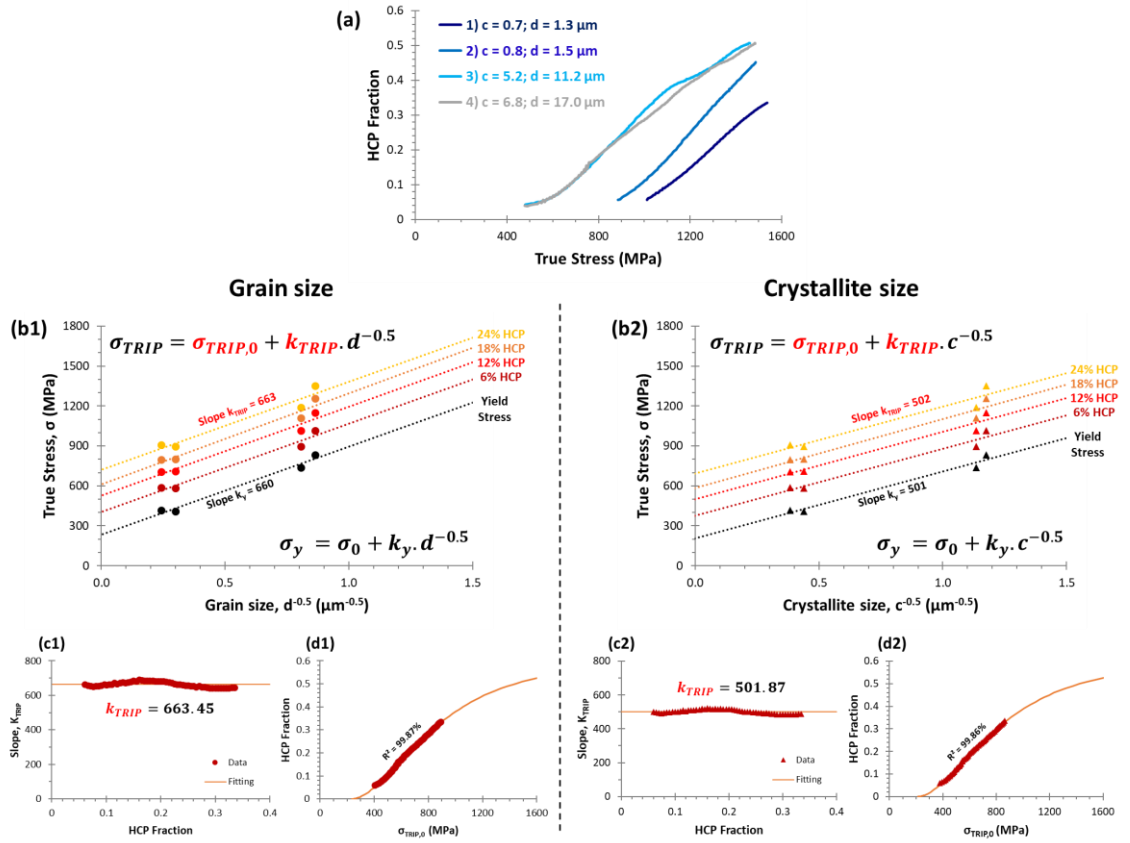

Figure 2.6: (a) HCP fraction measured as a function of true stress for samples with different FCC grain/crystallite sizes. Model development for grain size in Figures b1, c1, d1, and for crystallite size in Figures b2, c2, d2. (b1-b2) Hall-Petch plot for yield stress, in black, and HCP formation (TRIP effect), in color. Note that the TRIP evolution follows the Hall-Petch equation (Equations 2.5 and 2.6) as well as the yield stress, and the Hall-Petch slope is approximately the same for the yield stress and for the TRIP evolution (k ~ 660 MPa/µm$^{-0.5}$ for grain size, and ~500 for crystallite size). (c1-c2) Hall-Petch slope k_{TRIP} respecting an approximately linear behavior against the HCP fraction; and (d1-d2) Hall-Petch intercept $\sigma_{TRIP,0}$ respecting a logistic/sigmoidal behavior (Equation 2.7) as a function of the HCP fraction.

Isolating the term σ in Equation 2.7, we obtain the Equation 2.8, which describe the $\sigma_{TRIP,0}$ data as a function of the HCP fraction (f_{HCP}).

$$\sigma_{TRIP,0} = -\frac{1}{B}\ln\left[\frac{\left(\frac{K-A}{f_{HCP}-A}\right)^{v}-1}{Q}\right] \qquad \textbf{Eq. 2.8}$$

Finally, by replacing the expression for the intercept $\sigma_{TRIP,0}$ (Equation 2.8) into the Hall-Petch equation for phase transformation (Equation 2.6), it is obtained the

Equation 2.9, that describes the critical stress (σ_{TRIP}) required to form a certain fraction of strain-induced HCP phase (f_{HCP}), as a function of the initial FCC grain size (d) (or crystallite size (c)). Figures 2.7(a-b) show the 3D graphical representation of the model developed for both grain size and crystallite size, which are qualitatively similar. In the stress vs grain/crystallite size plane, the curve respects a Hall-Petch behavior (non-linearized), and in the stress vs HCP fraction plane, the curve presents a logistic/sigmoidal behavior, like the experimental curves in Figure 2.6(a). 2D plots of the model are in the supplementary material (Section S6).

$$\sigma_{TRIP} = -\frac{1}{B}\ln\left[\frac{\left(\frac{K-A}{f_{HCP}-A}\right)^{v}-1}{Q}\right]+\frac{k_{TRIP}}{\sqrt{d}} \qquad \textbf{Eq. 2.9}$$

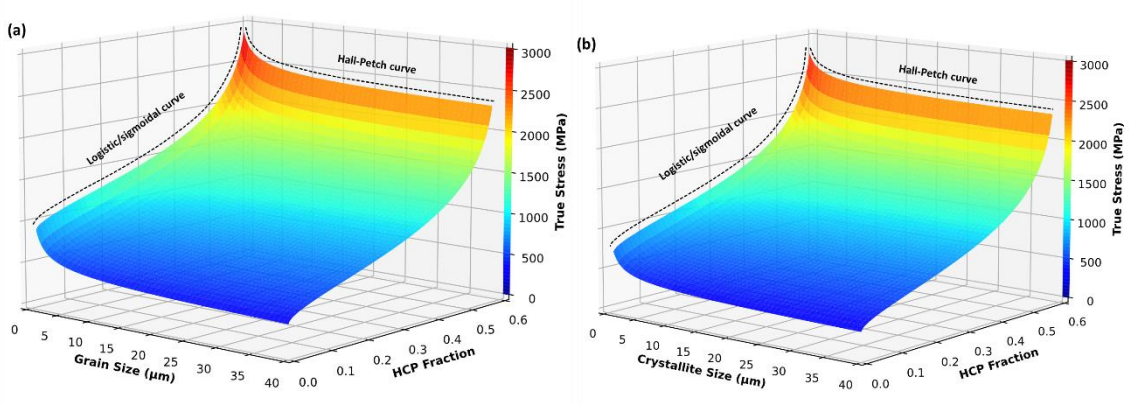

Figure 2.7: 3D plotting of the modeling (Equation 2.9) developed in this work for the $Cr_{40}Co_{40}Ni_{20}$ alloy: critical stress required to form a certain fraction of HCP phase (due to the TRIP effect), as a function of the initial FCC grain size (a) and crystallite size (b). The colors were used to facilitate the interpretation of the plot and represents the values of the "True Stress" axis.

The model also predicts the critical resolved shear stress (τ_{TRIP}), as shown in Equation 2.10, if divided the Equation 2.9 by the Taylor factor (M = 3.06 for FCC structures).

$$\tau_{TRIP} = \frac{\sigma_{TRIP}}{M} = -\frac{1}{M\,B}\ln\left[\frac{\left(\frac{K-A}{f_{HCP}-A}\right)^{v}-1}{Q}\right]+\frac{k_{TRIP}}{M\sqrt{d}} \qquad \textbf{Eq. 2.10}$$

By isolating f_{HCP} in Equation 2.9, the model can also determine the HCP fraction formed as a function of applied stress (σ) and grain size (d) (or crystallite size (c)), as shown in Equation 2.11.

$$f_{HCP} = A + \frac{K - A}{\sqrt[v]{1 + Qe^{-B\left(\sigma - \frac{k_{TRIP}}{\sqrt{d}}\right)}}} \quad \textbf{Eq. 2.11}$$

Equations 2.9 to 2.11 are valid for both grain size and crystallite size. For the $Cr_{40}Co_{40}Ni_{20}$ alloy, the R^2 of the complete model using the grain size is 96.25%, and the coefficients are: B = 2.163*10^{-3}; K = 0.5858; Q = -1.657; v = -0.4858; k_{TRIP} = 663.451; assuming A = 0, since there is no HCP phase in the initial microstructure.

Considering the crystallite size, the R^2 of the complete model is 95.48%, and the coefficients are: B = 2.130*10^{-3}; K = 0. 5840; Q = -1.582; v = -0.5080; k_{TRIP} = 501.866; also assuming A = 0. As can be seen, constants B, K, Q and v are quite similar in both cases.

2.5 Discussion

2.5.1 Interpretation, implications and limitations of the proposed model

The model developed in this work (Equations 2.9-2.11) combines two behaviors that were experimentally observed and have an associated physical meaning, therefore it is not a purely mathematical fitting. The first behavior described is the Hall-Petch behavior (Equations 2.5 and 2.6), which originally relates mechanical strength (yield stress) to grain/crystallite size. In this work, it was also associated with the evolution of a strain-induced phase transformation. In other words, our results imply that the evolution of the transformed fraction varies with grain/crystallite size according to the Hall-Petch equation, as shown in Figures 2.6(b1-b2). The mechanism that controls this relation will be better explored in a later topic (Section 2.5.4).

The Hall-Petch intercept (σ_0) is the intrinsic lattice friction stress and represents the mechanical strength of an alloy with grain/crystallite size tending to infinity. Similarly, the constant $\sigma_{TRIP,0}$ of this work (Equation 2.8) represents the stress required

to form a certain fraction of HCP in a material with grain/crystallite size tending to infinity (in practice, a very large grain/crystallite size).

The Hall-Petch slope (k_y) can be understood as the resistance offered by grain boundaries (and twin boundaries in the case of crystallite size measurements) to the dislocation slip and represents the degree of strengthening that grain refinement offers to the alloy. The constant k_{TRIP} in this work represents how much grain refinement disfavors the strain-induced phase transformation, since the higher the k_{TRIP}, the greater the stresses required for transformation as the grain/crystallite size decreases.

The second physical behavior described in the model is the logistic or sigmoidal growth behavior (Equation 2.7), used to describe several phenomena, including phase transformations [29]. This behavior is shown in Figures 2.6(d1-d2), and it can be clearly observed in our experimental curves of Figure 2.6(a). Regarding the physical meaning of the constants related to the logistic function (A, K, B, Q, v), A is the lower asymptote and represents the initial fraction of the HCP phase before the stress/strain application, which is equal to zero in this work. K is the upper asymptote and describes the maximum transformed fraction for the composition and test conditions. The values of A and K can only assume values between 0 and 1. B is related to the transformation rate; the higher $|B|$, the higher the rate of the transformation. Q is a horizontal displacement factor (on the stress axis); the higher $|Q|$, the higher the stress for phase transformation. Finally, v describes the asymmetry of the curve and has a more complex physical interpretation related to the balance between the stages of the transformation beginning and saturation.

It is important to emphasize that several factors should affect this type of transformation, including composition, temperature, strain rate, and deformation mode [29,63,84]. For example, compositions with higher SFE, less likely to present strain-induced transformation, would potentially present a lower maximum transformed fraction (lower K), lower transformation rate (lower B), and higher stresses required for transformation (higher Q). On the other hand, a composition more likely to undergo TRIP effect would present higher K and B, lower Q, and may even have an initial HCP phase fraction different from zero ($A > 0$). A change in the test temperature could also favor or disfavor the transformation [63], modifying the constants in a similar way to the previous example.

One of the caveats of the model is that its predictive power depends on the knowledge of the constants ($\sigma_{TRIP,0}$, k_{TRIP}, A, K, B, Q, and v), and the accurate obtaining of the constants for a given composition/condition requires the complete measurement of the phase transformation in at least two or three samples with different grain/crystallite sizes. From this, it is possible to estimate the stress required to form a certain transformed fraction, or the phase fraction formed when a certain stress is applied, for any grain/crystallite size. In some cases, it is also possible to identify the level of grain refinement that completely suppresses the phase transformation, which occurs when the stress for the transformation onset is greater than the ultimate tensile strength (σ_{UTS}) for a given condition.

Despite this caveat, there is a simplified way to use the model, considering a case in which the phase transformation was characterized for only one sample. It is necessary to have knowledge of the grain/crystallite size of the characterized sample and the Hall-Petch slope (k_y) of the composition studied. Thus, it is assumed that $k_y = k_{TRIP}$ for the composition/condition to be studied, which is true in the present work and will be better discussed in the following paragraphs. In this case, it is possible to estimate the evolution of the transformation at other grain/crystallite size values, according to Equation 2.12, which comes from the complete Equation 2.9, where the term k_{TRIP} is replaced by k_y, and the term $\sigma_{TRIP,0}$ is replaced by the term in parentheses, which consists of the stress required to form a certain fraction of HCP ($\sigma_{measured}$) and the grain size ($d_{measured}$) (or crystallite size, $c_{measured}$) of the characterized sample. This simplified equation can be applied to any fraction of the transformed phase.

$$\sigma_{TRIP} = \left(\sigma_{measured} - \frac{k_y}{\sqrt{d_{measured}}}\right) + \frac{k_y}{\sqrt{d}} \qquad \textbf{Eq. 2.12}$$

In this work, the Hall-Petch slope was shown to be approximately equal for yield stress and for TRIP effect ($k_y \approx k_{TRIP}$: ~660 MPa/μm$^{-0.5}$ for grain size, and ~500 MPa/μm$^{-0.5}$ for crystallite size), and it is worth discussing when this equality is expected. No information was found in the literature related to the resistance of grain boundaries against strain-induced phase transformation (k_{TRIP}), but there is a discussion regarding the resistance of grain boundaries against deformation twinning (k_{TWIP}) [74], which can be extrapolated to the context of a phase transformation (TRIP effect) due to

the similarity between these two mechanisms. Basically, alloys with less propensity for planar slip (medium/high SFE) should either not present the TRIP effect or the stress required to activate this mechanism will be much higher than the yield stress. In the latter case, the TRIP activation should occur at a high level of deformation, well above the yield point ($\varepsilon > \varepsilon_y$), so k_{TRIP} will correspond to the Hall-Petch slope for this level of deformation ($k(\varepsilon)$), which means that $k(\varepsilon) = k_{TRIP}$. However, in FCC metals, the Hall-Petch slope for a given deformation level ($k(\varepsilon)$) increases with straining, becoming increasingly greater than k_y [85]. In this context, $k(\varepsilon) > k_y$, and the equality between k_{TRIP} and k_y does not occur, since $k_{TRIP} > k_y$.

On the other hand, alloys with a greater propensity for planar slip (low SFE) tend to present lower stresses for activation of the TRIP effect, which will occur at lower deformation levels, tending towards the yield point, so that k_{TRIP} tends towards k_y, until they become equal ($k_{TRIP} = k_y$). Therefore, it is challenging to accurately predict when this equality is valid, but it is expected in alloys with SFE low enough to easily activate the TRIP effect, in general SFE < 15 mJ/m² [35], such as the $Cr_{40}Co_{40}Ni_{20}$ alloy of this work with 11.8 mJ/m² [7].

2.5.2 TRIP onset extrapolation

As discussed previously, it is challenging to detect the onset of the transformation accurately, because in the early stages of the strain-induced transformation, the HCP peaks are small with similar intensities to the background noise. The model developed in this work allows us to extrapolate the experimental results of higher strains to the early stages of the tensile test. Using Equation 2.9, when the HCP fraction tends to zero ($f_{HCP} \rightarrow 0$), the term $\sigma_{TRIP,0}$ tends to 233.6 MPa, and we obtain Equation 2.13, an expression that describes the critical stress to activate the TRIP effect (the TRIP onset) as a function of grain size. Similarly, considering the crystallite size, the term $\sigma_{TRIP,0}$ tends to 215.5 MPa, and we obtain Equation 2.14.

$$\lim_{f_{HCP}\to 0} \sigma_{TRIP}(d) = \sigma_{TRIP,0} + \frac{k_{TRIP}}{\sqrt{d}} = 233.6 + \frac{663.4}{\sqrt{d}} \qquad \textbf{Eq. 2.13}$$

$$\lim_{f_{HCP}\to 0} \sigma_{TRIP}(c) = \sigma_{TRIP,0} + \frac{k_{TRIP}}{\sqrt{c}} = 215.5 + \frac{501.9}{\sqrt{d}} \qquad \textbf{Eq. 2.14}$$

Equations 2.13 and 2.14 were plotted together with the yield stress in Figure 2.8(a). According to the model, the activation of the TRIP effect (in red) occurs concomitantly with the yield point (in black), considering both grain size and crystallite size. Checking the diffractograms collected close to the yield point, as represented in Figure 2.8(b) for sample 4 (intensity axis in log scale), it is observed that there are already HCP phase peaks at a very low volume fraction (measured as 0.07% HCP) even before the macroscopic yield point. In other words, a small fraction of HCP begins to form in the microplasticity stage, where there is dislocation activity occurring at stress levels slightly below the macroscopic yield point, immediately before the generalized plastic deformation.

Basically, our results and the model show that the TRIP onset increases with grain refinement, but proportionally to the yield stress. This is an indication that, in this alloy with very low SFE, the activation of the TRIP effect depends only on the dislocation slip onset.

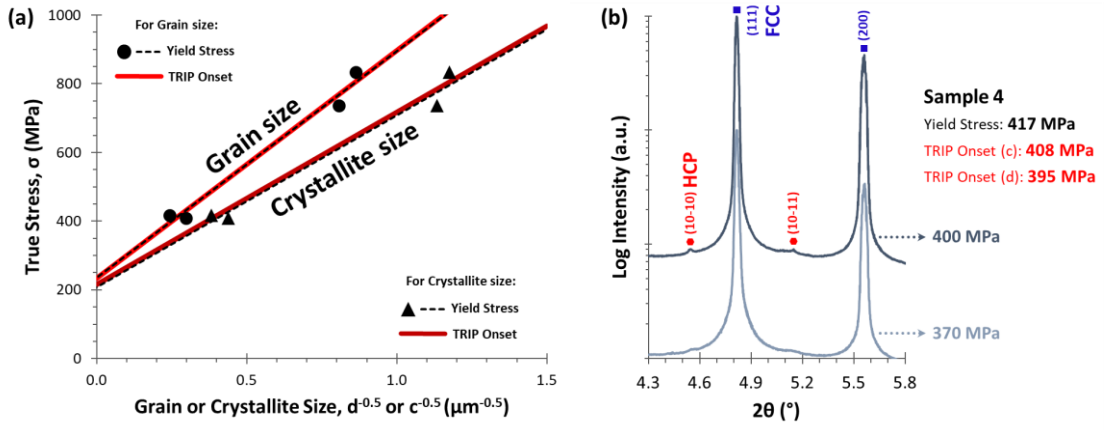

Figure 2.8: (a) Critical stress for TRIP onset (according to the model) and yield stress vs grain/crystallite size. (b) Diffractograms of sample 4 (log scale) collected close to the yield point and TRIP onset, corresponding to stress levels of 370 and 400 MPa, showing HCP peaks at a very low volume fraction even before the macroscopic yield point (in the microplasticity stage).

2.5.3 Deformation level controlling the TRIP effect

Using the modeling presented on this work, it is possible to calculate the HCP fraction formed (f_{HCP}) and the HCP formation rate (f'_{HCP}), as shown in Figures 2.9(a-c) for the grain/crystallite sizes studied here. The model allows us to extrapolate experimental results from higher strains into the early stages of the tensile testing, where the HCP peaks were small and thus unproperly fitted. These results in Figures 2.9(a-c) reveal that the grain/crystallite size influences the TRIP onset in terms of the critical stress but does not significantly alter the TRIP evolution.

In more details, the TRIP onset occurs approximately at the yield point, therefore, in the HCP fraction vs stress plot (Figure 2.9(a)), the curves are out of phase as each sample yields at a different stress level. On the other hand, in the HCP fraction vs strain plot (Figure 2.9(b)), the curves are almost identical, they all start at approximately the same strain level of ~0.35% (close to the yield point) and evolve in a similar way until the fracture point. This similarity can also be observed in the plot of HCP formation rate vs strain (Figure 2.9(c)), obtained by the derivative of the HCP fraction curves. From this data, it is noted that the HCP fraction and the HCP formation rate (i.e. the TRIP evolution) are controlled by the deformation level, which is proportional to the density of mobile dislocations [50]. The dislocation density (vs strain) obtained in this work is almost insensitive to changes in grain/crystallite size (as shown in Figure 2.9(d)), as well as the TRIP evolution (vs strain) also does not depend on the grain/crystallite size (Figure 2.9(b)).

As the grain/crystallite size does not significantly change the TRIP evolution nor the dislocation density, it explains why the work-hardening rate (WHR) is similar for the different grain/crystallite sizes in this work, as shown in Figure 2.9(e). The steady WHR plateaus occur at approximately the same stress level of 1800-2000 MPa, and according to the Considere's criterion, the plastic instability due to necking occurs when the WHR equals the true stress ($d\sigma_{tr}/d\varepsilon_{tr} = \sigma_{tr}$), so the WHR curves reach the necking point at different strain levels due to the difference in the yield stress of each sample.

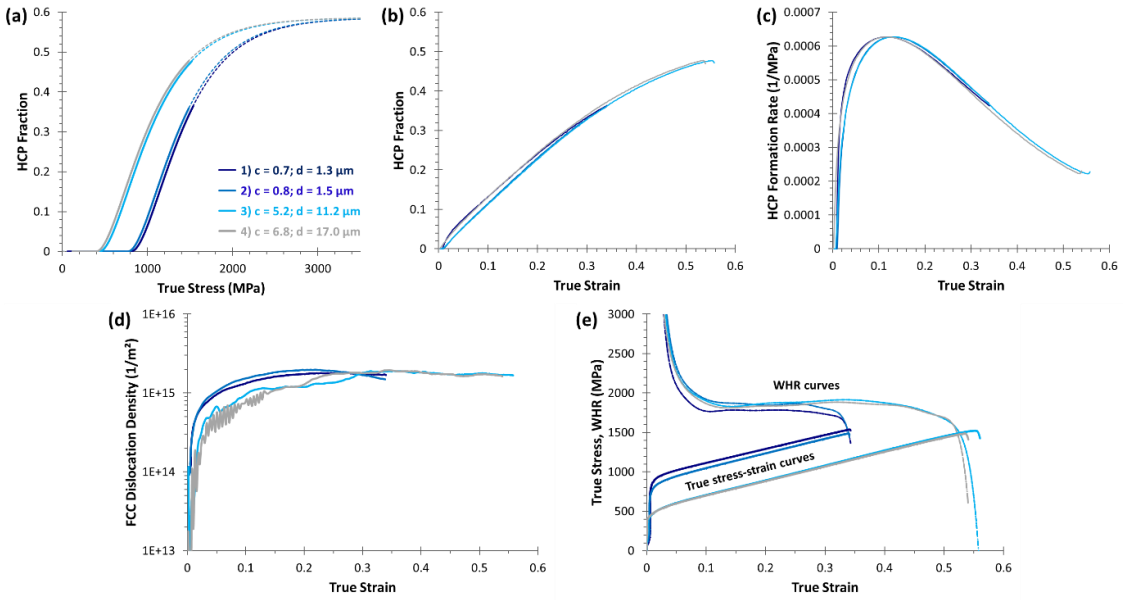

Figure 2.9: HCP fraction calculated by the model for the tensile testing conditions: (a) vs true stress (dotted line is an extrapolation), and (b) vs true strain. (c) HCP formation rate vs true strain. (d) FCC dislocation density. (e) True stress-strain curves and WHR curves. Note that the HCP fraction (TRIP effect) is controlled by the deformation level. HCP vs stress curves are out of phase as each sample yields at a different stress level. On the other hand, HCP vs strain curves are almost identical, in the same way as dislocation density curves, which provide similar WHR for all four samples. In this figure, the model based on grain size was used, but the conclusions are the same considering the model based on crystallite size.

2.5.4 Mechanism for the grain/crystallite size dependence of TRIP onset and evolution

The Hall-Petch model for grain/crystallite refinement strengthening is based on the concept of a dislocation pile-up against grain boundaries [85,86] and annealing twin boundaries [75,77]. Stress is concentrated at the head of the dislocation pile-up. When a certain threshold stress is exceeded, dislocations sources are activated, dislocations are emitted into adjacent grains/crystallites, and macroscopic yielding occurs. A longer dislocation pile-up length leads to more stress being concentrated, but the pile-up length is limited by the grain/crystallite size. In a refined structure, the pile-up length is reduced, less stress is concentrated, and more external stress is needed to reach the yield point. The Hall-Petch pile-up model predicts a linear relation between the yield stress

(σ_y) and the inverse square root of the grain/crystallite size ($1/\sqrt{d}$ or $1/\sqrt{c}$), as shown in Equation 2.5 [85].

Wagner and Laplanche (2023) [74] observed that the twinning stress (TWIP onset) also follows the Hall-Petch behavior in the Cantor alloy (CrMnFeCoNi). The mechanism for the grain size dependence of twinning stress is also based on the pile-up of dislocations at the grain boundary, where the stress concentration allows to overcome the nucleation of a deformation twin into the neighboring grain.

In the present work, it was observed that the onset and evolution of the strain-induced phase transformation (TRIP effect) also followed the Hall-Petch behavior. This is a first indication that the mechanism responsible for the dependence of the TRIP effect on the grain/crystallite size should also be based on the pile-up of dislocations. Indeed, the strain-induced phase transformation is related to dislocation slip. From the literature, it is known that the nucleation and growth of the strain-induced HCP phase depend on the passage of Shockley partial dislocations on every other {111} close-packed planes of the FCC phase [47,52].

According to the model developed in this work (Equations 2.9-2.11), the TRIP onset in the $Cr_{40}Co_{40}Ni_{20}$ alloy is approximately at the yield point, as shown in Figure 2.8(a), and we observe the formation of a small fraction of transformed phase just before the macroscopic yield stress, as shown in Figure 2.8(b). This indicates that the bottleneck for the HCP formation is dislocation slip, which occurs immediately before the yield point, in the microplasticity stage, where limited dislocation slip occurs in the material. In this regime, dislocations are generated and move in grains/crystallites that are preferentially oriented in relation to the applied external stress. Still in the microplasticity stage of FCC metals with low SFE, the dislocations dissociate into Shockey partials, which can initiate the formation of some HCP nuclei in energetically favorable sites, where the partials are organized on every other {111} close-packed plans of the FCC phase. Due to the low SFE, dislocations move more planar and easily form pile-ups that eventually reach grain and annealing twin boundaries. The stress concentrated at the head of the dislocation pile-up allows the emission of dislocations into adjacent grains/crystallites, when it becomes a chain effect, macroscopic yielding occurs. From this point onwards, there are many partial dislocations with mobility, which contribute to the extensive formation and growth of the HCP phase.

HCP phase nuclei tend to form and grow in energetically favorable sites, where there is stress concentration and extensive movement of dislocations, as well as in locations where the local composition leads to a lower SFE, where the stability of the HCP phase is larger.

2.5.5 Hypothesis: short-range order preventing FCC-HCP transformation

In the literature, it was observed that SRO significantly increases the SFE in the CrCoNi alloy [60,64–67], which logically disfavors the TRIP effect [28,35,36]. However, SRO can be easily destroyed by dislocation slip [87].

Hypothetically, if the alloy studied here possesses some degree of SRO, this would likely increase the SFE. Then, the onset of dislocation movement (the yield point) would disrupt the SRO, locally reducing the SFE and facilitating strain-induced transformation (TRIP) for subsequent dislocations. This study observed that the TRIP effect begins around the yield point, regardless of the grain/crystallite size, coinciding with the onset of dislocation movement. It would support the aforementioned hypothesis that the alloy studied here possesses some degree of SRO.

2.5.6 Influence of grain size on stacking fault energy and TRIP effect

It is well known that increasing the SFE, the stability of the HCP phase decrease, disfavoring the TRIP effect [29,35], which would increase the critical stress for TRIP. However, our results indicate that this is not the case for the current alloy. In fact, the critical stress for TRIP increased with grain refinement, but it is not necessary to resort to an explanation that involves SFE, once it is completely explained by the fact that TRIP onset occurs approximately at the yield point for our samples and each sample yields at a different stress level due to the grain refinement strengthening. Samples with smaller grain sizes yield at higher stresses and therefore the TRIP onset is higher.

This is an indication that, at least in this alloy with a very low SFE, the nucleation and growth of the strain-induced HCP phase depend only on the onset of dislocation slip. Even if the critical stress for HCP formation is slightly lower than the yield stress, the strain-induced transformation will only occur close to the yield point, at

least in the microplasticity stage, as the transformation depends on the movement of dislocations. Therefore, although the apparent SFE calculation indicates that grain refinement shifts the SFE in the direction of disfavoring the TRIP effect, the previous analysis makes it clear that this is not the case for the current alloy. In the alloy and grain size range studied in this work, grain refinement did not significantly disfavor the TRIP effect. We observed that grain refinement is effective in hindering dislocation motion, although once slip starts, the strain-induced transformation occurs immediately.

2.5.7 Influence of the TRIP effect and its early activation on mechanical properties

In the $Cr_{40}Co_{40}Ni_{20}$ alloy, the strain-induced HCP phase (responsible for the TRIP effect) initially forms with a thin and elongated morphology, like needles or plates, presenting the $<110>_{FCC}//<11\text{-}20>_{HCP}$; $\{111\}_{FCC}//(0001)_{HCP}$ orientation [7], in agreement with other alloys in the literature [42,47,48]. This orientation corresponds to the alignment of the close-packed planes and directions of both structures. During deformation, the HCP phase lamellae (related to the TRIP effect) may act as additional barriers for dislocation slip, the dynamic Hall-Petch effect, which also occurs in the presence of deformation twins (related to the TWIP effect). These mechanisms, in addition to dislocation slip, provide greater strengthening capacity for these alloys. According to Considere's criterion, the high WHR provided by the TRIP/TWIP effects delays plastic instability, considerably increasing the ductility, and enabling these alloys to withstand higher stresses before failing [21,27,29,88–91].

The early activation of plasticity effects (TRIP/TWIP) leads to superior mechanical properties, as nanotwins and HCP lamellae provide high and steady WHR in an extended strain range [21]. In this work alloy, the TRIP onset was easily reached approximately at the yield point due to: i) the very low SFE, which facilitates the FCC to HCP phase transformation, and ii) the relatively high yield stress, which allows plasticity to begin at higher stresses, thus the critical stress for phase transformation is reached more quickly, at lower strains (~0.35%). Furthermore, this alloy has a high WHR capacity, which delays the plastic instability and fracture point, according to Considere's criterion. This, combined with the early activation of the strain-induced

transformation, allows the TRIP effect to occur in an extended deformation range, providing a great combination of strength and ductility to the $Cr_{40}Co_{40}Ni_{20}$ alloy.

In addition to the effects already discussed on WHR capacity, the TRIP effect can also improve yield stress through a mechanism that induces grain refinement. When a TRIP alloy undergoes the cold rolling process, a partial strain-induced transformation occurs (FCC → FCC + HCP), then during the high-temperature recrystallization heat treatment, this transformation is reversed, and the microstructure returns to FCC with more refined grains. More details about this mechanism can be found in the literature [29,31]. This is quite advantageous in alloys that have a high strengthening potential via grain refinement, such as the $Cr_{40}Co_{40}Ni_{20}$ alloy of this work. For example, after going through the same thermomechanical processing, the TRIP $Cr_{40}Co_{40}Ni_{20}$ alloy (d = 4 to 36 μm) [7] presented much smaller grain sizes than the TWIP $Cr_{40}Co_{30}Ni_{30}$ alloy (d = 8 to 52 μm) [43].

Regarding the mechanical behavior and properties of the $Cr_{40}Co_{40}Ni_{20}$ alloy, it should be noted that its mechanical strength is significantly enhanced due to the high solid solution strengthening component (~250 MPa) [7,24] and the high strengthening potential via grain refinement [7], the latter being optimized due to the mechanism in which the strain-induced phase transformation generates more refined FCC grains. Furthermore, the strain-induced transformation (TRIP effect) and its early activation in the $Cr_{40}Co_{40}Ni_{20}$ alloy provide high work-hardening capacity, resulting in improved ductility, ultimate tensile strength, and toughness [26–29].

2.6 Conclusions

In situ SXRD during tensile tests and complementary analyses in different grain/crystallite sizes of the $Cr_{40}Co_{40}Ni_{20}$ MPEA allowed the study of the partial FCC to HCP strain-induced transformation (i.e., TRIP effect), and its impact on the mechanical behavior. The following conclusions were drawn:

1) The critical stress required to form a certain HCP fraction (TRIP effect) follows the Hall-Petch relation ($\sigma_{TRIP} = \sigma_{TRIP,0} + k_{TRIP}d^{-0.5}$), as well as the yield stress also does. The Hall-Petch slope is approximately the same for the yield stress

and TRIP effect ($k_y \approx k_{TRIP}$: ~660 MPa/μm$^{-0.5}$ for grain size, and ~500 MPa/μm$^{-0.5}$ for crystallite size), and this equality seems to be valid for alloys with SFE low enough to easily activate the TRIP effect.

2) This work proposes a Hall-Petch-based model (Section 2.4.4) and a mechanism (Section 2.5.4) to describe the influence of FCC grain/crystallite size on the onset and evolution of the TRIP effect. It predicts the critical stress required to form a certain HCP fraction, or the fraction formed when a certain stress is applied, for different grain/crystallite sizes. The model was based on the combination of two experimentally observed behaviors: the logistic/sigmoidal growth behavior that classically describes phase transformations; and the Hall-Petch behavior, which classically relates the grain/crystallite size to the yield stress, and here a relationship with the critical stress for phase transformation and its evolution was observed and modeled.

3) In terms of stress, the critical stress for TRIP is proportional to the grain refinement strengthening; and in terms of strain, grain size has no obvious influence on TRIP effect. It is not necessary to resort to an explanation that involves the apparent SFE disfavoring the transformation. It is well explained by the fact that TRIP onset occurs approximately at the yield point for all samples and each sample yields at a different stress level due to the grain refinement strengthening. This is an indication that, at least in this alloy with a very low SFE, the nucleation and growth of the strain-induced HCP phase depend only on the onset of dislocation slip.

4) Regarding the mechanical behavior, the strain-induced transformation (TRIP effect) allowed obtaining more refined grains after cold rolling and annealing, reaching $c = 0.7$ and $d = 1.3$ μm in sample 1. A considerable increase of 100% in yield stress (417 → 834 MPa) was observed due the high grain refinement strengthening of this alloy. Our results and the model indicate that, in current alloy, it is possible to take advantage of grain refinement without compromising the occurrence of the TRIP effect, which is easily activated approximately at the

yield point. As discussed, the TRIP effect and its early activation provide high work-hardening capacity, resulting in improved ductility, ultimate tensile strength, and toughness.

CHAPTER 3 – Effect of C and N additions on phase equilibria and grain refinement

3.1 Introduction

As mentioned earlier, CrCoNi MPEAs have recently gained attention due to their excellent combinations of mechanical properties. The $Cr_{40}Co_{40}Ni_{20}$ MPEA stands out by showing a high mechanical strengthening via grain refining, and high work hardening capacity, resulting from the strain-induced HCP phase formation (TRIP effect) [7]. The previous chapter (Chapter 2) evaluated the influence of grain size on the TRIP effect, and it indicated that it is possible to take advantage of grain refinement without compromising the occurrence and benefits of the TRIP effect.

It is well known in literature that C and N addition can refine the microstructure through the Zener pinning mechanism when precipitates (carbides and nitrides) form [11,12]. On the other hand, it is unclear if C and N atoms in solute form are effective in microstructural refinement. A recent review paper about grain growth in HEAs [11] states that the exploration of solute atoms to inhibit grain growth seems to be an interesting research front in future studies. For the solute drag effect of C and N, there are some reports indicating negligible effects [13–15], while some others showed their noticeable effect [16–19], which necessitates more research in this field.

The use of interstitial elements (such as C and N) as microstructural refiners should be especially advantageous in alloys that have high sensitivity of mechanical properties in relation to grain size, such as CrCoNi MPEAs [38,68], especially the $Cr_{40}Co_{40}Ni_{20}$ alloy [7]. However, small additions of interstitial elements typically have a strong influence on phase equilibrium and microstructure [2], due to the high diffusivity and large lattice distortion caused by these interstitial elements. This chapter (Chapter 3) assess the effect of C and N additions on phase equilibria and grain refinement capacity, using the $Cr_{40}Co_{40}Ni_{20}$ composition as Base alloy.

3.1.1 Objectives

From the $Cr_{40}Co_{40}Ni_{20}$ MPEA, different N- and C-doped alloys were designed, produced, and thermomechanically treated under different conditions. The objective of

this chapter was to evaluate the effect of C and N on phase equilibria, microstructure, precipitate formation, and grain refinement capacity in a CrCoNi alloy.

The XRD and SEM-EBSD analyses in samples treated at different conditions provided data to evaluate the influence of C and N on existing phases, grain size, and grain size distribution at different conditions, as well as on the grain growth kinetics.

3.2 Literature review

3.2.1 Grain refinement strengthening

Grain refinement is a strengthening mechanism that often increases mechanical strength without significant losses in ductility. In some cases, there may even be a concomitant increase in strength and ductility [26,27,92]. Strengthening via grain refinement occurs because a decrease in grain size increases the density of boundaries, which in turn act as obstacles to the movement of dislocations [85].

Traditionally, grain refinement strengthening is evaluated using the Hall-Petch equation (Equation 3.1), which relates the yield stress (σ_y) to the average grain size (d) [85,93,94]. The Hall-Petch slope (k) measures how efficient grain refinement strengthening is, i.e., the resistance offered by grain boundaries to dislocation sliding. High values of k indicate that the mechanical strength increases significantly with decreasing grain size. The term "$kd^{-0.5}$" represents the grain refinement strengthening component. The term "σ_0" is the intrinsic friction stress of the lattice or intrinsic yield stress and refers to the yield stress of a still polycrystalline material (since it considers the effect of the polycrystalline aggregate given by the Taylor constant) but presenting an infinite grain size, i.e., without the reinforcement generated by grain refinement.

$$\sigma_y = \sigma_0 + k.d^{-0,5} \qquad \textbf{Eq. 3.1}$$

Grain refinement strengthening is one of the outstanding aspects of $Cr_{40}Co_{40}Ni_{20}$ MPEA [7], which will be the subject of study in this thesis. As can be seen in Figure 2.1 (previously presented in Chapter 2), this alloy has Hall-Petch coefficients (σ_0 and k) higher than that of similar alloys (CrCoNi [38,68] and CrMnFeCoNi [95]) and much

higher than that of pure FCC metals [85]. It means that mechanical strength improves more efficiently with grain refinement in the $Cr_{40}Co_{40}Ni_{20}$, justifying its use as the Base alloy in this study, where interstitial elements are added to induce grain refinement and improve mechanical properties.

3.2.2 Interstitial elements doping in MPEAs

The addition of interstitial elements and the control of mechanisms induced by them represents an important optimization route already applied in several commercial alloys, such as the importance of C in the steel sector. Small additions of interstitial elements such as H, B, C and N typically have a strong influence on phase equilibria, microstructure and properties [2,12], due to the high diffusivity and large distortion in the crystal lattice caused by these elements.

The addition of interstitial elements can have different purposes: precipitation strengthening, grain refinement, formation of hard primary phases, etc. In this chapter, the literature review will address the different impacts of these elements, but focusing on the grain refinement mechanism, as it is an effective strengthening mechanism for the Base alloy of this work ($Cr_{40}Co_{40}Ni_{20}$). In the next chapter (Chapter 4), the literature review will focus on the influence of interstitial elements on deformation mechanisms and SFE.

Interstitial elements can induce grain refinement by different mechanisms. The "solute drag effect" is able to reduce boundary mobility, because a moving boundary has to overcome or drag a solute atmosphere that exerts a delaying force on it [96–100]. In the “grain boundary segregation” mechanism, an element is segregated at the grain boundaries in the form of solute (not in the form of another phase), it can assist in the formation of more refined microstructures in two ways: i) by reducing the mobility of the grain boundaries due to the drag effect generated by the solute atoms at the boundaries; and/or ii) by reducing the interfacial energy of the grain boundaries and decreasing the thermodynamic driving force for the migration of these boundaries; both mechanisms act to retard grain growth [101,102]. Another mechanism is known as “Zener pinning”, in which interstitial elements form particles of other phases (carbides, nitrides, etc.). In this case, moving boundaries encounter these particles and have their

movement limited due to the difficulty or impossibility of traversing them [101]. Microstructural refinement is optimized if there is a large volume fraction of small and well-distributed particles. At high temperatures, the particles can coalesce or dissolve, which decreases the efficiency of this mechanism; furthermore, some grain boundaries may break free from this mechanism before others, generating heterogeneous (abnormal) grain growth. As grain size increases, the driving force for grain growth decreases and may become insufficient to overcome the particles, so grain growth stagnates [101].

The following is a compilation of the main publications involving the addition of C and N in CrCoNi alloys or similar systems. In general, the literature agrees that the formation of precipitates (carbides and nitrides) is effective in refining the grains of CrCoNi-like alloys through the pinning mechanism, although it depends on the precipitate fraction and average size. On the other hand, Zamani et al. (2023) [11], in a recent review paper about grain growth in HEAs, state that the exploitation of solute atoms to inhibit grain growth seems to be an interesting research front in future studies. For the solute drag effect of C and N, there are some reports indicating negligible effects [13–15], while some others showed their noticeable effect [16–19], which necessitates more research in this field.

3.2.3 Effect of C-doping in MPEAs

Bertoli et al. (2021) [103] developed CrCoNi alloys with high C concentrations, one of them starting from the composition $Cr_{40}Co_{40}Ni_{20}$, the subject of study in this work. It is estimated that a small fraction of C (up to 0.5 at%) is soluble in the FCC matrix, after the solubility limit an $M_{23}C_6$ carbide precipitates. Higher C contents favor the formation of the M_7C_3 carbide. These carbides tend to be rich in Cr, but both exhibit appreciable solubility of Co and to a lesser degree of Ni [103,104]. The $M_{23}C_6$ carbide is of the same space group (Fm-3m) as the FCC matrix [105], which should facilitate precipitation [106].

Moravcik et al. (2020) [16], studying CrCoNi alloys doped with C, observed that C significantly retards recrystallization kinetics by decorating grain boundaries (impurity drag or solute drag) and impeding interface motion through carbides (pinning

mechanism). The addition of 0.5 and 1.0 at% C decreased the grain size from 3.3 to 2.7 and 2.1 μm, respectively. The addition of C also increased the mechanical strength with little loss in ductility.

Shang et al. (2019) [14] studied minor additions of C in the equiatomic CrCoNi alloy, and found that the presence of C in solid solution (without carbide formation) does not significantly influence grain size, but improves the mechanical strength of the alloy, reduces ductility losses, and also increases the SFE, postponing the TWIP effect [14,107].

Klimova et al. (2021) [108] observed grain refinement by the pinning mechanism, increased mechanical strength and increased recrystallization temperature due to the addition of C in a CrMnFeCoNi alloy. Qin et al. (2019) [109] and Fan et al. (2018) [110], by adding C to AlCrFeCoNi alloys, also observed that carbide formation was quite effective in grain refinement by the pinning mechanism.

In summary, the literature indicates that C addition in CrCoNi-like MPEAs can influence the microstructure through two distinct regimes depending on its solubility. When retained in solid solution, C primarily contributes to solid-solution strengthening and to modifications in deformation behavior, with inconsistent impact on grain refinement through solute drag effects. Once the solubility limit is exceeded, the precipitation of Cr-rich carbides becomes a dominant microstructural factor. These carbides effectively restrict grain boundary motion through the pinning mechanism. C-doping has been consistently associated with delayed recrystallization, higher recrystallization temperatures, and refined grain structures, leading to increased strength with relatively moderate losses in ductility. Therefore, C stands out as a versatile interstitial element capable of simultaneously affecting precipitation behavior, grain boundary mobility, and mechanical performance.

3.2.4 Effect of N-doping in MPEAs

Chung; Luan; Shek (2022) [17] observed considerable grain refinement (192 to 130 μm) when adding 0.5 at% N to the CrFeCoNi alloy, even without nitride precipitation, but the paper does not focus on the grain refinement mechanism.

Moravcik et al. (2020) [13] added 0.5 at% N to the equiatomic CrCoNi alloy, and Traversier et al. (2021) [15] added up to 1.2 at% N to a CrFeMnNi alloy. Both observed that all the N remained in solid solution, with no nitride formation. The N in solution was not able to refine the microstructure of the material, but it improved the tensile mechanical properties.

Feng et al. (2018) [111] added 1.75 at% N to the equiatomic CrCoNi alloy, N was observed to be uniformly distributed in the FCC matrix and in the form of Cr-rich M_2N nitrides, which induced significant grain refinement by the pinning mechanism. There was an improvement in mechanical and corrosion resistance in the sample doped with N.

Jodi et al. (2019, 2020) evaluated the addition of ~1 at% N in the equiatomic CrCoNi alloy [112] and in Cantor alloy [113], and found that N induced the formation of Cr-rich M_2N nitrides, which helped to inhibit grain growth by the pinning mechanism.

Klimova et al. (2020) [114] studied additions of 0.5; 1.0 and 2.0 at% N in Cantor alloy (CrMnFeCoNi). Only with 2 at% N, they observed the formation of M_2N nitride and appreciable grain refinement. The N addition improved the tensile mechanical properties, according to the authors, mainly due to the solid solution strengthening caused by N-doping.

N also has other influences on these alloys. Moravcik et al. (2020) [13] reported that N in solid solution increases the Hall-Petch coefficients (σ_0 and k) of the CrCoNi alloy. It was observed that the addition of N in the Cantor's alloy (CrMnFeCoNi) was able to suppress/decrease the formation of sigma phase [115], in this case, both the N-doped and undoped samples showed similar grain size, since both precipitates, M_2N and sigma phase, respectively, contributed similarly to microstructural refinement by the pinning mechanism.

Overall, N-doping in CrCoNi-like MPEAs presents a composition-dependent effect on grain refinement. At lower concentrations, N often remains in solid solution, where its primary contribution is solid-solution strengthening and modification of intrinsic strengthening parameters such as the Hall-Petch coefficients, with inconsistent influence on grain size. At higher N contents, the formation of Cr-rich nitrides becomes possible, and these precipitates can effectively inhibit grain boundary migration through

the pinning mechanism, leading to appreciable grain refinement. In addition to its role in boundary mobility, N has been reported to influence phase stability (suppressing sigma phase formation) and mechanical behavior. The effectiveness of N as a grain growth inhibitor depends critically on its concentration, distribution, and precipitation behavior, reinforcing the need for systematic studies such as the one proposed in this thesis.

3.3 Experimental Procedure

3.3.1 Alloy design, production, and chemical analysis

The $Cr_{40}Co_{40}Ni_{20}$ alloy was selected as the "Base alloy" for this project due to its high strengthening potential via grain refinement. The selection of the C and N contents to be added was based on information from the literature of similar alloys, on the knowledge acquired from preliminary work, and on computational thermodynamic calculations (CALPHAD method). CALPHAD calculations were performed in Pandat (databases: PanHEA2021b for C and PanNi2021a for N) and ThermoCalc (database: TCHEA5 for both C and N) software, both presented similar results. Figures 3.1 and 3.2 show the isopleths obtained via CALPHAD, which helped not only in the choice of compositions, but also in the planning of heat treatments. Two compositions with N (between 0.1 and 1.0 at% N) and three compositions with C (between 0.1 and 0.5 at% C) were selected, in addition to the Base alloy ($Cr_{40}Co_{40}Ni_{20}$), totaling six alloys to be studied in this project.

Ingots weighing between 50 and 80 g (variable length, width 13.5 mm, thickness ~8.5 mm) were produced in an arc melting furnace with an argon atmosphere. The ingots were turned and remelted at least five times to ensure compositional homogeneity. High purity Cr (9.995% purity), Co (99.9+%) and Ni (99.99%) were used as raw materials. Carbon was added in the form of C graphite (99.9%) and nitrogen was added in the form of chromium nitride powder (CrN).

Chemical analyses were performed to measure the C and N contents in the N-32 (0.32 at% N), C-30 (0.30 at% C), and C-45 (0.45 at% C) alloys. The composition of the other alloys is being estimated as N-10 (~0.10 at% N) and C-17 (0.17 at% C) based on

alloys previously produced by similar methods. C was measured by the combustion technique in LECO CS844 Series Elemental Analyzer, and N by thermal conductivity in LECO ONH836 Series Elemental Analyzer. The Cr, Co, and Ni contents were adjusted from the nominal values and confirmed by energy-dispersive X-ray spectroscopy (EDS). The resulting compositions for this work are also shown in Figures 3.1 and 3.2 (dashed lines).

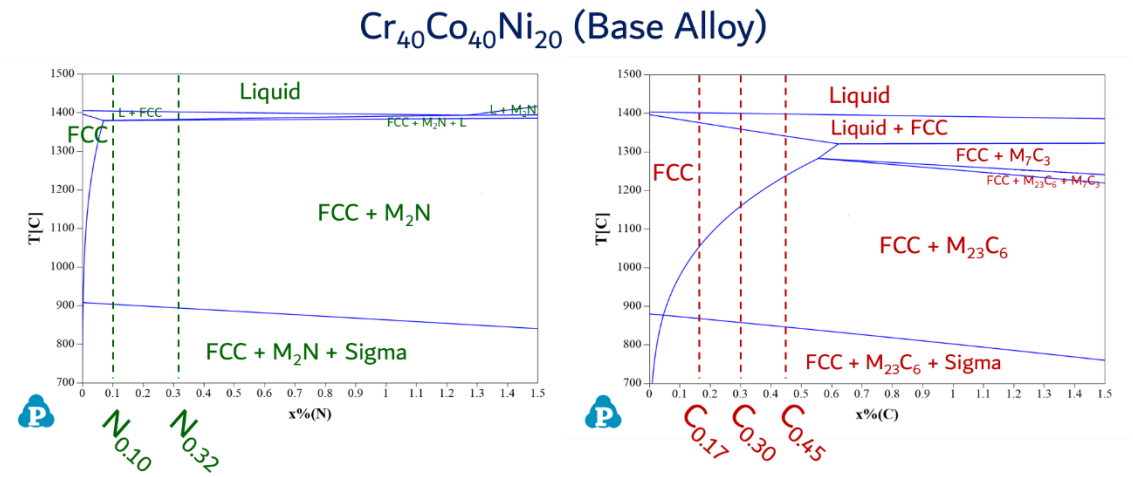

Figure 3.1: Isopleths obtained via CALPHAD (Pandat software, databases: PanHEA2021b for C and PanNi2021a for N) and alloys selected for the project. The dashed lines show the phase equilibria of the compositions obtained in this study.

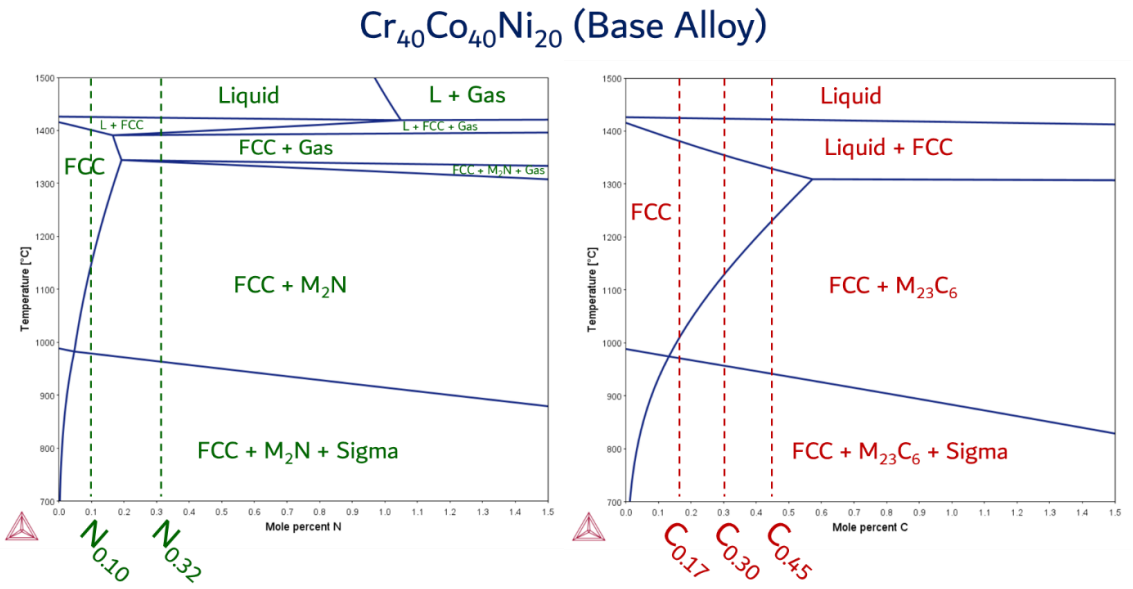

Figure 3.2: Isopleths obtained via CALPHAD (ThermoCalc software, database: TCHEA5) and alloys selected for the project. The dashed lines show the phase equilibria of the compositions obtained in this study.

3.3.2 Thermomechanical processing

The six alloys underwent the same thermomechanical processing. First, homogenization heat treatment at 1200 °C for 2 hours with water quenching was done. Samples in homogenized condition were cut to be characterized.

The alloys then underwent several cold-rolling and intermediate heat treatments steps, in more detail: the ~8.5 mm thick ingots were cold-rolled to ~5 mm, heat treated at 1200 °C for 10 minutes, cold-rolled to ~3 mm, heat treated at 1200 °C for 10 minutes, and finally cold-rolled to a final thickness of ~1.5 mm, resulting in a cold rolling thickness reduction of ~50%. Samples in cold-rolled condition were cut to be characterized.

From the cold-rolled sheets, recrystallization heat treatments were performed in a muffle furnace, for 1 hour, at different conditions of temperatures: 750, 900, 1000, 1100, and 1200 °C. For each treatment, the furnace was heated and maintained at the treatment temperature for 1 hour to ensure thermal homogeneity before placing the samples. Then, the samples of the six different alloys were placed together inside the furnace, and after 1 hour of heat treatment, the samples were removed and rapidly quenched in water. Furthermore, heat treatments were carried out at 1000 °C for 1, 4, and 12 hours to evaluate grain growth kinetics.

3.3.3 Sample preparation and XRD/SEM analysis methodology

Samples were carefully prepared according to standard metallographic preparation, up to a final stage of at least 15 h in a vibratory polisher with a 0.04 μm colloidal silica suspension. This stage is important in TRIP alloys for removing any transformed phase layer from the surface region formed in the cutting and grinding processes.

XRD experiments were done in a PanAnalytical Empyrean XRD. This XRD was equipped with a Mo source, which generates significantly less X-ray fluorescence with 3d transition metals (the main constituents of CrCoNi alloys) than the more commonly used Cu source. This was crucial for having less background, which better revealed phases present with low volume fractions. The beam was calibrated to focus on the

sample in a rectangular region of ~6x7 mm to ensure that multiple grains could be analyzed even in the larger grain size samples. A camera was used to center the samples.

SEM analyses were done in FEI Helios Nanolab 600i SEM and Tescan S8252G Raman SEM, to perform basic SEM in addition to energy-dispersive X-ray spectroscopy (EDS) and electron backscatter diffraction (EBSD) analyses. In the last one, the EDAX Velocity™ Pro EBSD camera offered high-speed EBSD mapping up to 2500 pps using a CMOS sensor. The EBSD maps were post-processed in the EDAX OIM Analysis™ software using the "grain dilation" cleanup routine, with the parameters adjusted according to the magnification and step size (spatial resolution) used in each analysis.

3.3.4 Grain and crystallite size counting

From the SEM-EBSD analyses of the recrystallized samples, both the grain size (excluding annealing twin boundaries) and the crystallite size (accounting for both grain and annealing twin boundaries) were determined for the FCC phase, as the contribution of annealing twins to alloy strength is still a matter of debate in the literature [74]. The FCC grain/crystallite size were obtained by the intercept procedure, according to the ASTM E112 standard [79], using ten horizontal and ten vertical lines per field.

3.4 Results

3.4.1 Microstructural characterization of homogenized samples

A sample of each alloy in homogenized condition (1200 °C for 2 hours, with water quenching) was characterized. SEM-EBSD images at the same magnification (100x) were shown in Figure 3.3. All samples were indexed as single-phase FCC structure. No evidence of precipitates and other phases (carbides and nitrides) was found in the homogenized condition, even in high magnification analyses. Grain size counting resulted in values greater than 200 μm, but the exact values are not reliable in this condition due to the low number of grains present in the images.

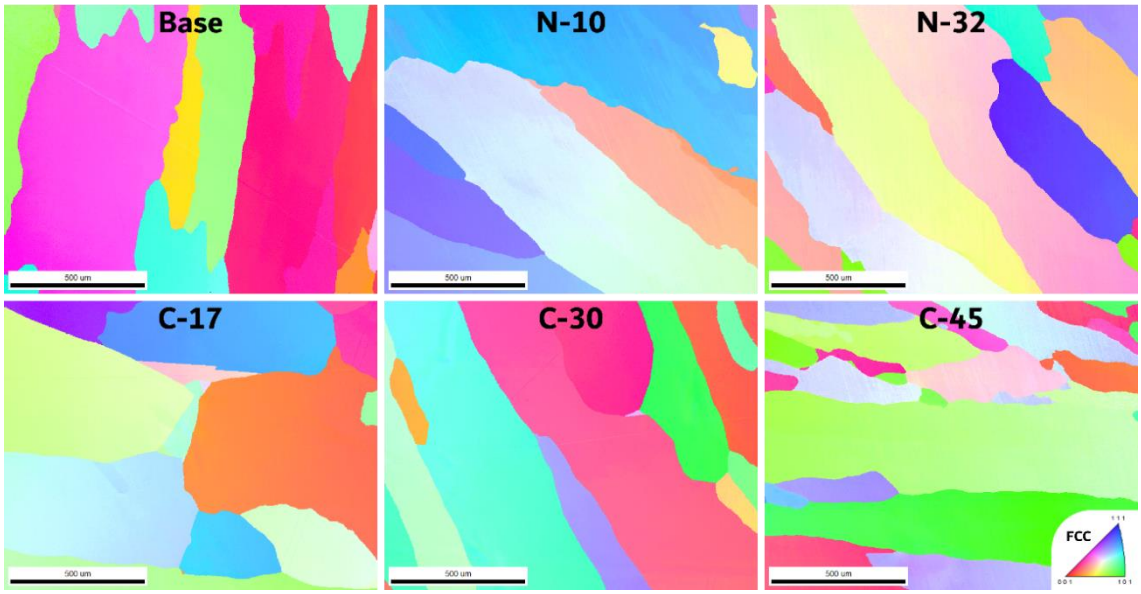

Figure 3.3: SEM-EBSD (inverse pole figure) images of the homogenized condition (1200 °C, 2h). Images at the same magnification (100x).

3.4.2 Microstructural characterization of cold-rolled samples

A sample of each alloy in the cold-rolled condition (50% cold rolling thickness reduction) was characterized. All samples presented a dual phase microstructure (FCC + HCP), highlighting the strain-induced phase transformation (TRIP effect) during cold-rolling process. These results will be presented and discussed in the next chapter (Chapter 4: Effect of C and N additions on stacking fault energy and TRIP deformation mechanism).

3.4.3 Microstructural characterization of recrystallized samples

Figures 3.4 to 3.8 show the XRD analyses of the recrystallized samples. First, no evidence of carbides and nitrides was found in any of the samples analyzed via XRD.

The HCP phase (from the TRIP effect during cold rolling) was not observed under any condition, indicating that it was completely dissolved during the recrystallization heat treatment.

The samples recrystallized at 1200 (Figure 3.4), 1100 (Figure 3.5), and 1000 °C (Figure 3.6) were indexed as FCC phase only. The samples recrystallized at 900 (Figure 3.7) and 750 °C (Figure 3.8) were indexed as FCC phase with a small fraction of sigma phase. The non-indexed peaks, such as the peaks at ~18, 20.5, 29, and 34°, refer to the K-β reflections of the FCC phase, and they are present in all samples.

Regarding the stability of the sigma phase, it is noted that the addition of either C or N disfavors the sigma phase. In Figure 3.7 (900 °C), the sigma phase is basically suppressed in samples N-32 and C-45, and in Figure 3.8 (750 °C), the sigma phase fraction is lower in sample N-32.

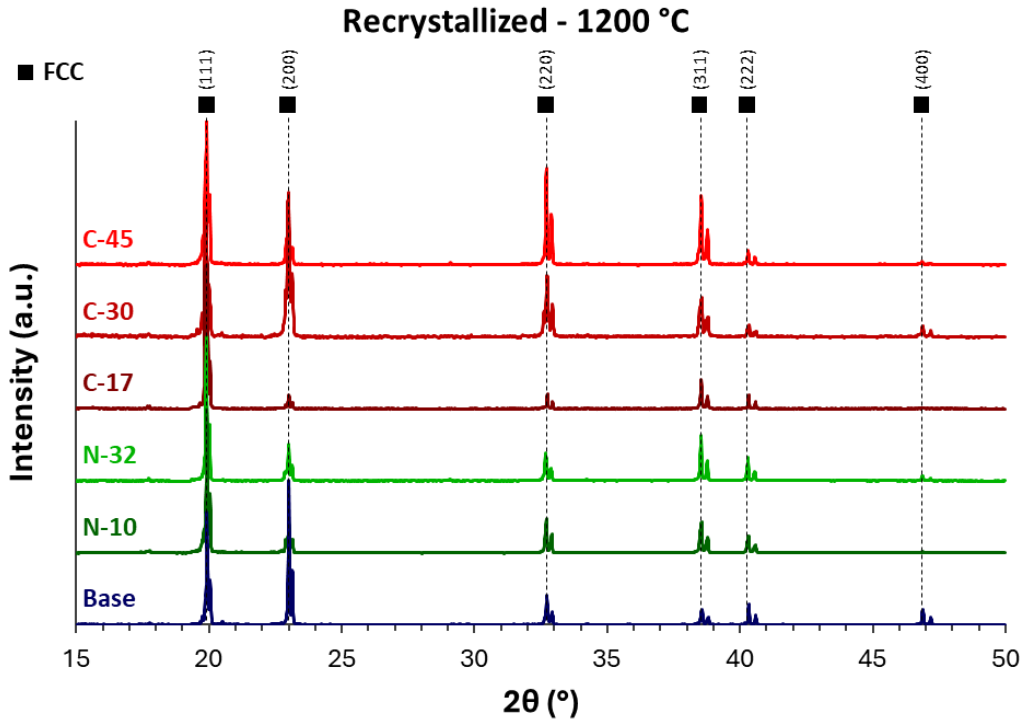

Figure 3.4: XRD analyses of the recrystallized condition (1200 °C, 1h), indexed as FCC phase only. No evidence of sigma phase, carbides, and nitrides in the diffractograms. Unindexed peaks (18, 20.5, 29, and 34°) are the K-β reflections of the FCC phase.

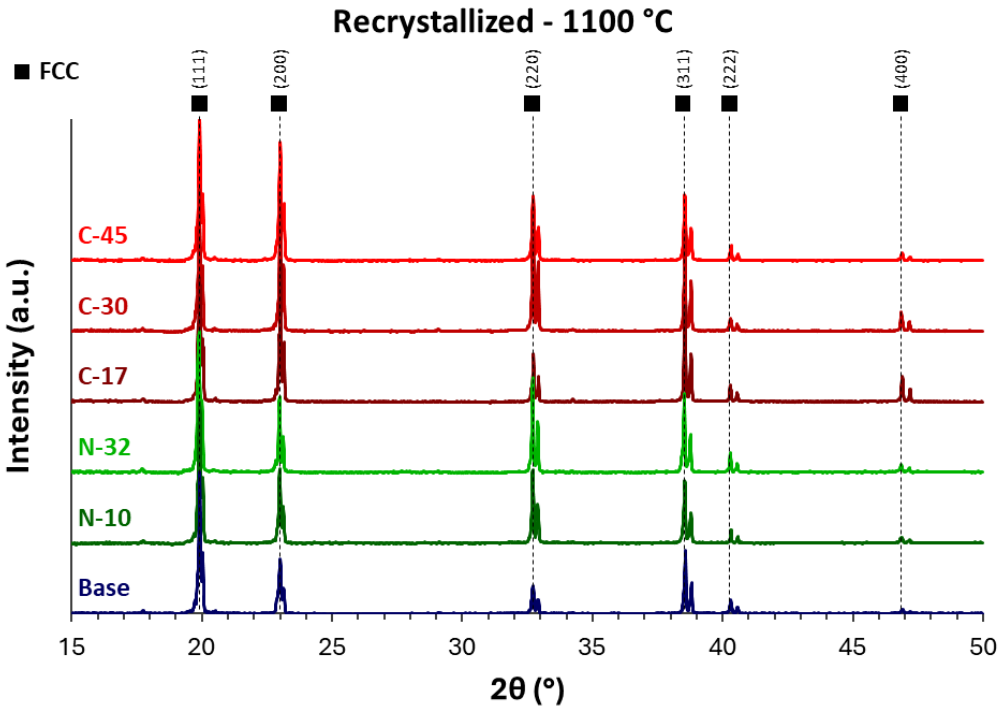

Figure 3.5: XRD analyses of the recrystallized condition (1100 °C, 1h), indexed as FCC phase only. No evidence of sigma phase, carbides, and nitrides in the diffractograms. Unindexed peaks (18, 20.5, 29, and 34°) are the K-β reflections of the FCC phase.

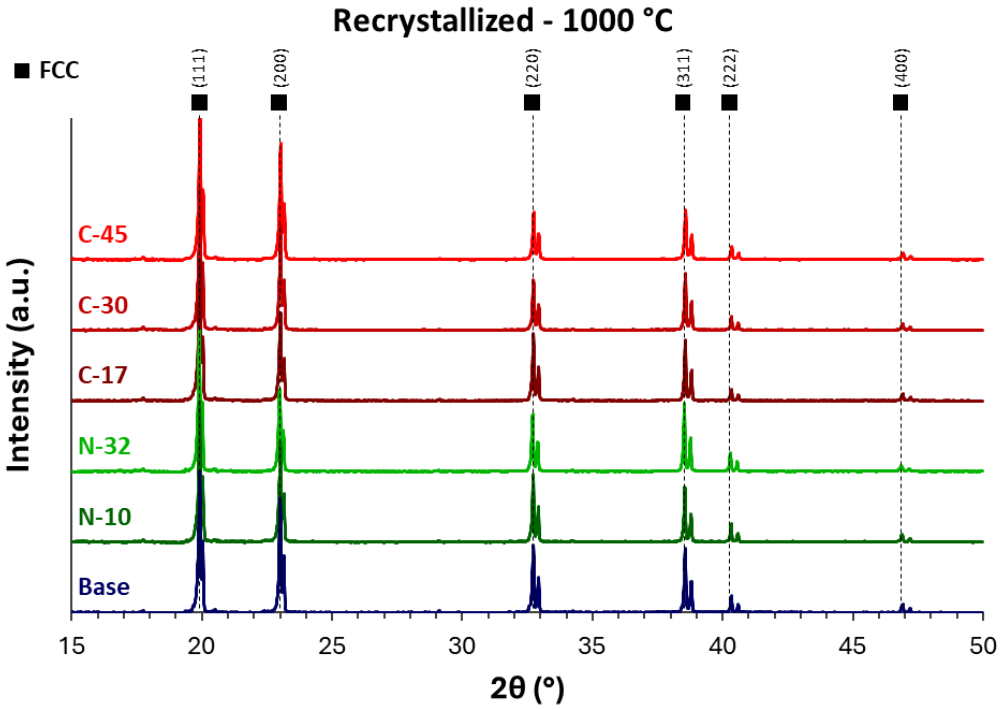

Figure 3.6: XRD analyses of the recrystallized condition (1000 °C, 1h), indexed as FCC phase only. No evidence of sigma phase, carbides, and nitrides in the diffractograms. Unindexed peaks (18, 20.5, 29, and 34°) are the K-β reflections of the FCC phase.

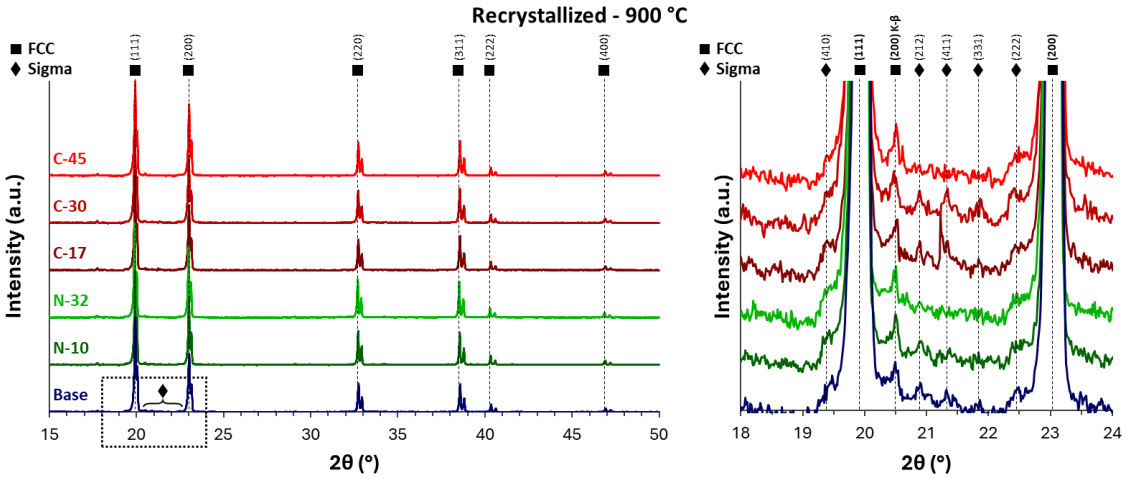

Figure 3.7: XRD analyses of the recrystallized condition (900 °C, 1h), indexed as FCC phase with a small fraction of sigma phase. No evidence of carbides and nitrides in the diffractograms. Unindexed peaks (18, 20.5, 29, and 34°) are the K-β reflections of the FCC phase.

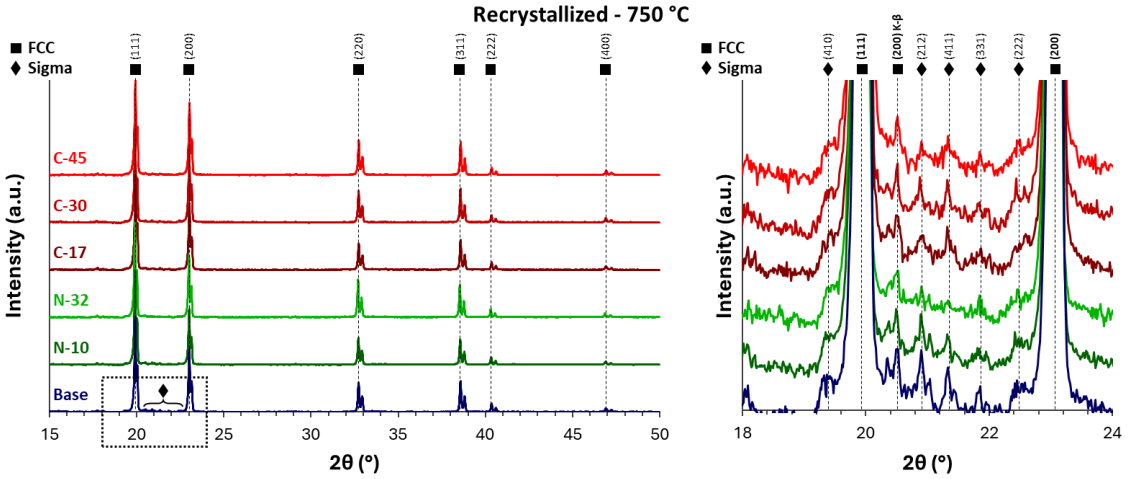

Figure 3.8: XRD analyses of the recrystallized condition (750 °C, 1h), indexed as FCC phase with a small fraction of sigma phase. No evidence of carbides and nitrides in the diffractograms. Unindexed peaks (18, 20.5, 29, and 34°) are the K-β reflections of the FCC phase.

SEM-EBSD analyses were performed on recrystallized samples treated at 750, 900, 1000, 1100, and 1200 °C, as shown in Figures 3.9 to 3.13. In each figure, the samples are shown at the same magnification. From these analyses it was possible to identify the presence of equiaxed grains of the FCC phase with annealing twins in all samples and the presence of precipitates in some samples. It was also possible to

quantify the grain size (excluding annealing twin boundaries) and crystallite size (accounting for both grain and annealing twin boundaries).

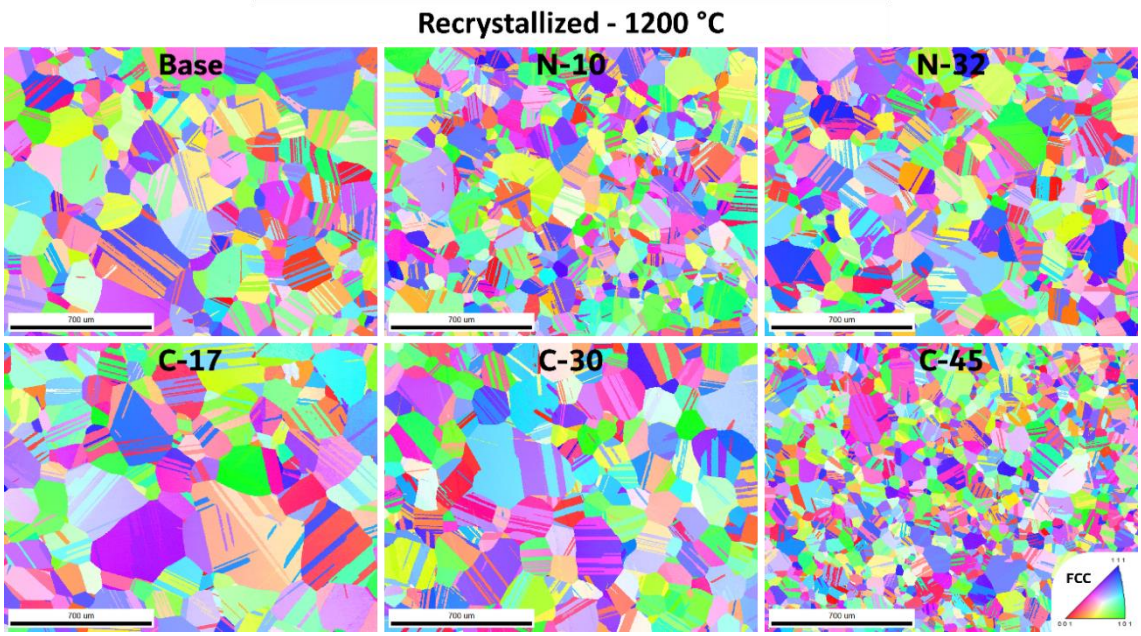

Figure 3.9: SEM-EBSD (inverse pole figure) images of the recrystallized condition (1200 °C, 1h). Images at the same magnification (75x).

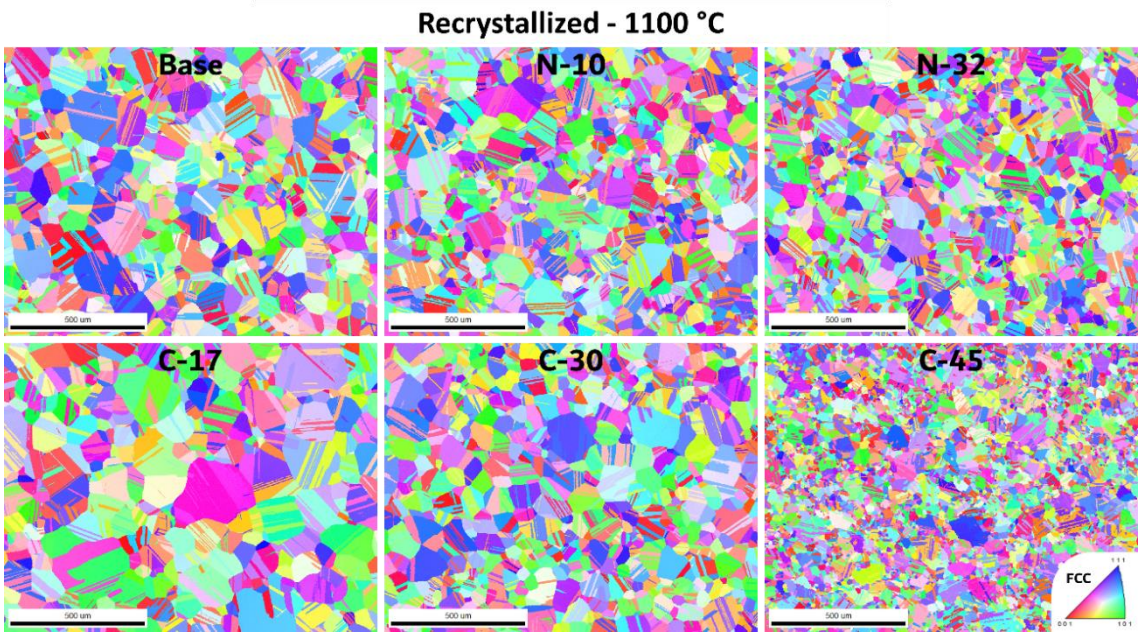

Figure 3.10: SEM-EBSD (inverse pole figure) images of the recrystallized condition (1100 °C, 1h). Images at the same magnification (100x).

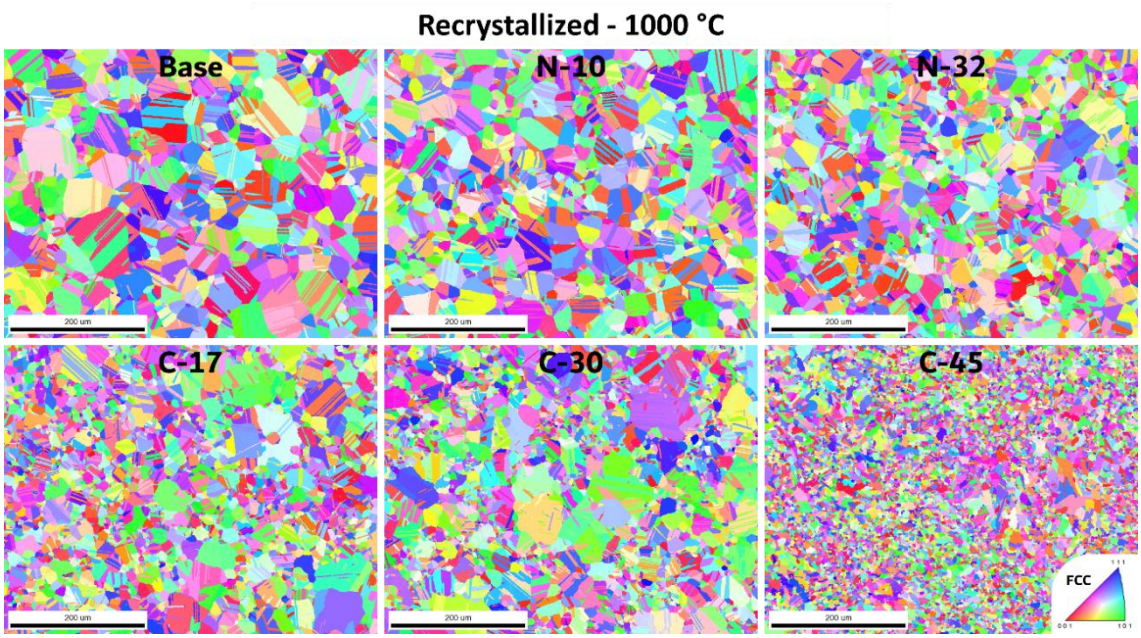

Figure 3.11: SEM-EBSD (inverse pole figure) images of the recrystallized condition (1000 °C, 1h). Images at the same magnification (250x).

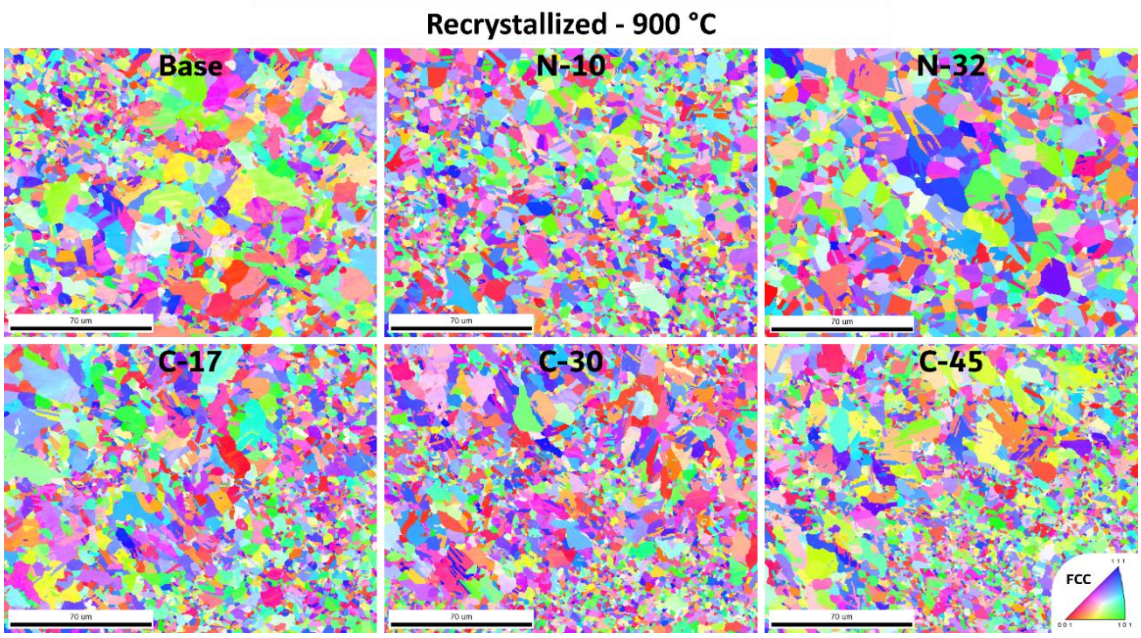

Figure 3.12: SEM-EBSD (inverse pole figure) images of the recrystallized condition (900 °C, 1h). Images at the same magnification (750x).

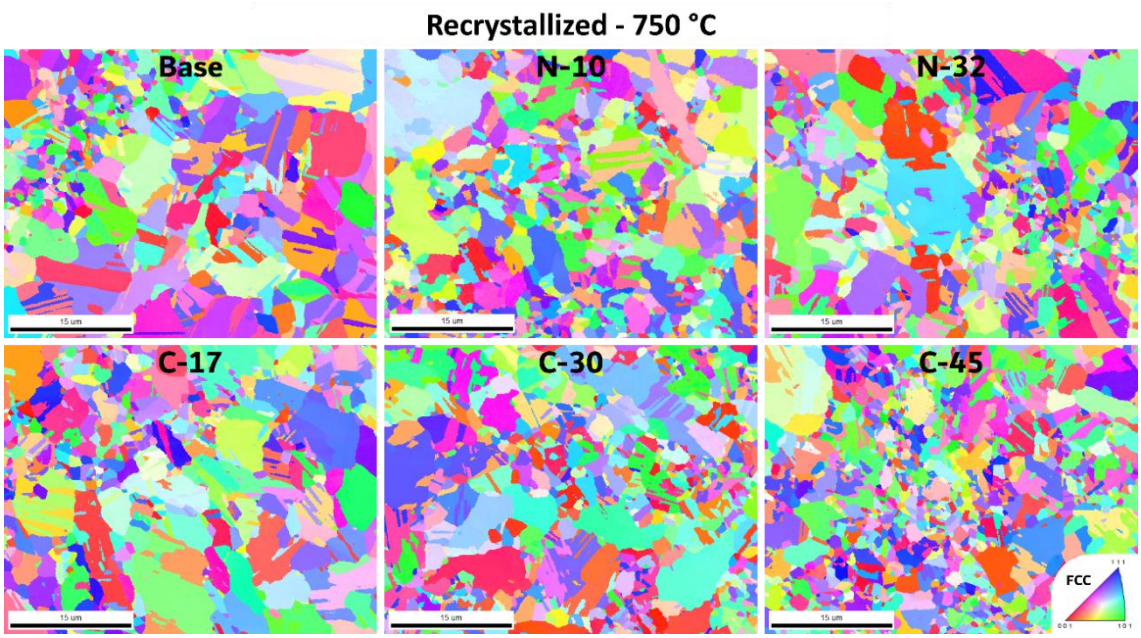

Figure 3.13: SEM-EBSD (inverse pole figure) images of the recrystallized condition (750 °C, 1h). Images at the same magnification (3000x).

Through SEM-EBSD analyses, it was possible to identify the presence of precipitates (sigma and/or $M_{23}C_6$ carbides, in this case) and measure their area fraction. Figures 3.14 to 3.19 show the conditions under which precipitation occurred for each alloy. For example, for the Base alloy (Figure 3.14), the formation of ~1.8% sigma phase was identified at 750 °C (for 1 h), ~1.1% sigma at 900 °C, and above 1000 °C there was no precipitation. For the N-doped samples, sigma phase precipitation also occurred, although in some cases it was not possible to satisfactorily measure the fraction of precipitates through EBSD indexing. For the C-doped samples, sigma phase and $M_{23}C_6$ carbides may form, but the indexing was not satisfactory enough to indicate the fraction of each phase separately, therefore, the fraction obtained refers to the precipitate fraction (sigma + carbides, when both are present). Despite this, it is possible to conclude about the presence or absence of these phases with the aid of other analyses, such as XRD and EDS, which will be discussed later.

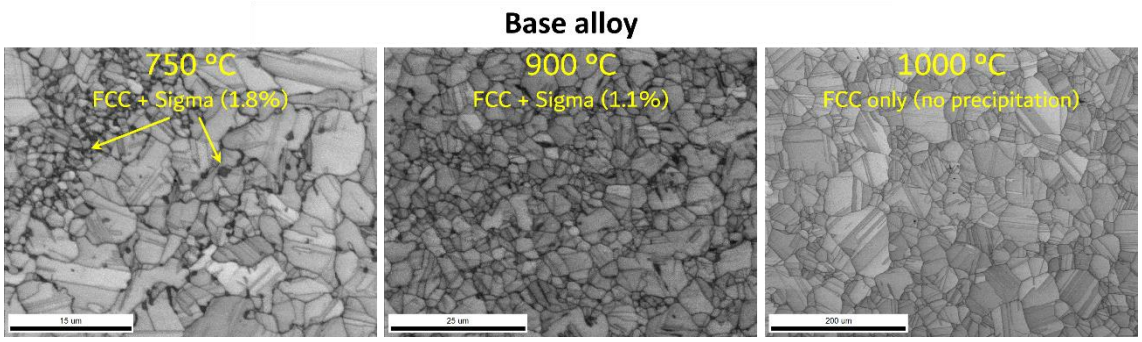

Figure 3.14: SEM-EBSD (image quality) images of the recrystallized samples in different temperatures (Base alloy, heat treated for 1h), with the indication of existing precipitates and its fraction.

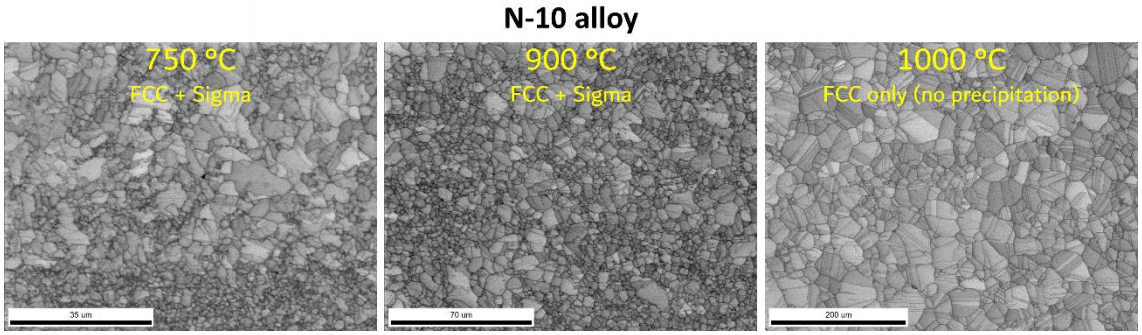

Figure 3.15: SEM-EBSD (image quality) images of the recrystallized samples in different temperatures (N-10 alloy, heat treated for 1h), with the indication of existing precipitates. It was not possible to satisfactorily measure the fraction of precipitates in these analyses.

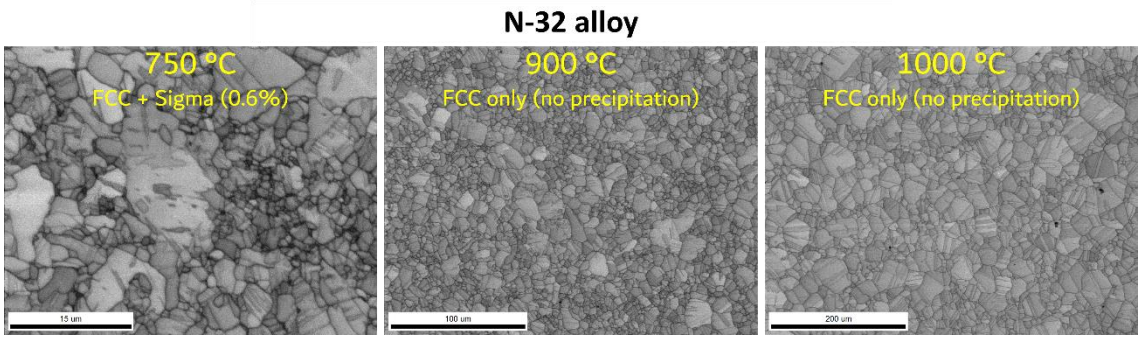

Figure 3.16: SEM-EBSD (image quality) images of the recrystallized samples in different temperatures (N-32 alloy, heat treated for 1h), with the indication of existing precipitates and its fraction.

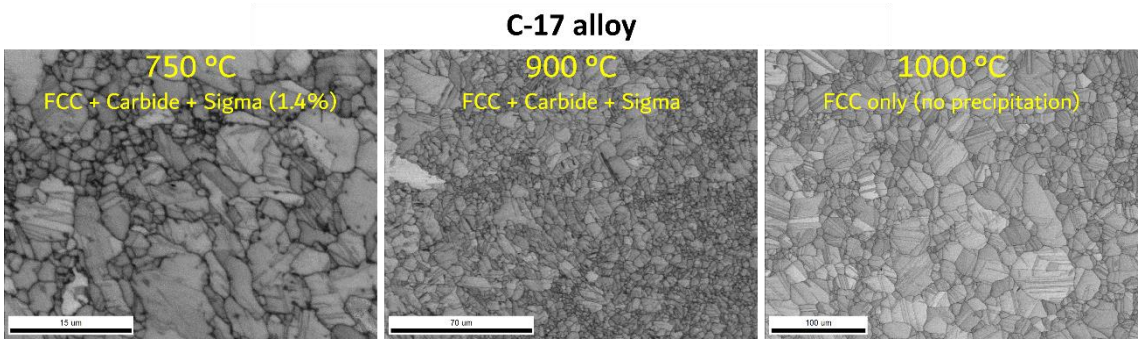

Figure 3.17: SEM-EBSD (image quality) images of the recrystallized samples in different temperatures (C-17 alloy, heat treated for 1h), with the indication of existing precipitates and its fraction.

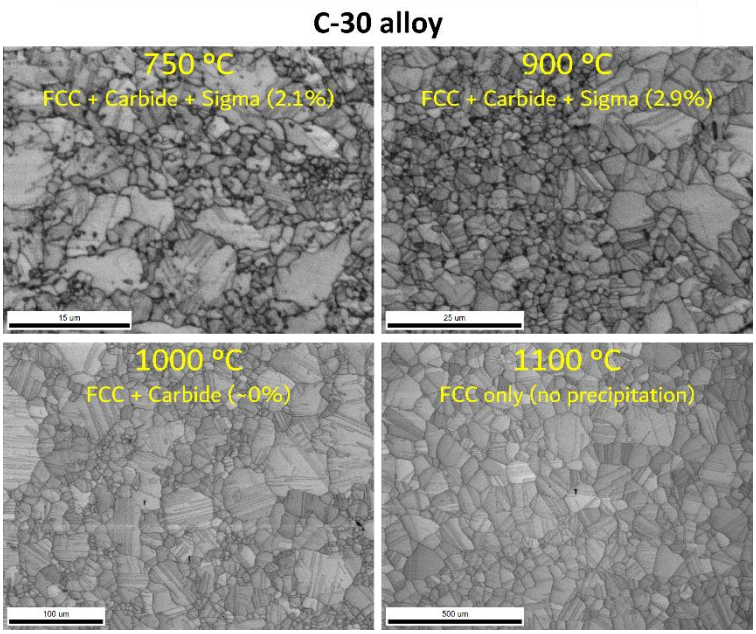

Figure 3.18: SEM-EBSD (image quality) images of the recrystallized samples in different temperatures (C-30 alloy, heat treated for 1h), with the indication of existing precipitates and its fraction.

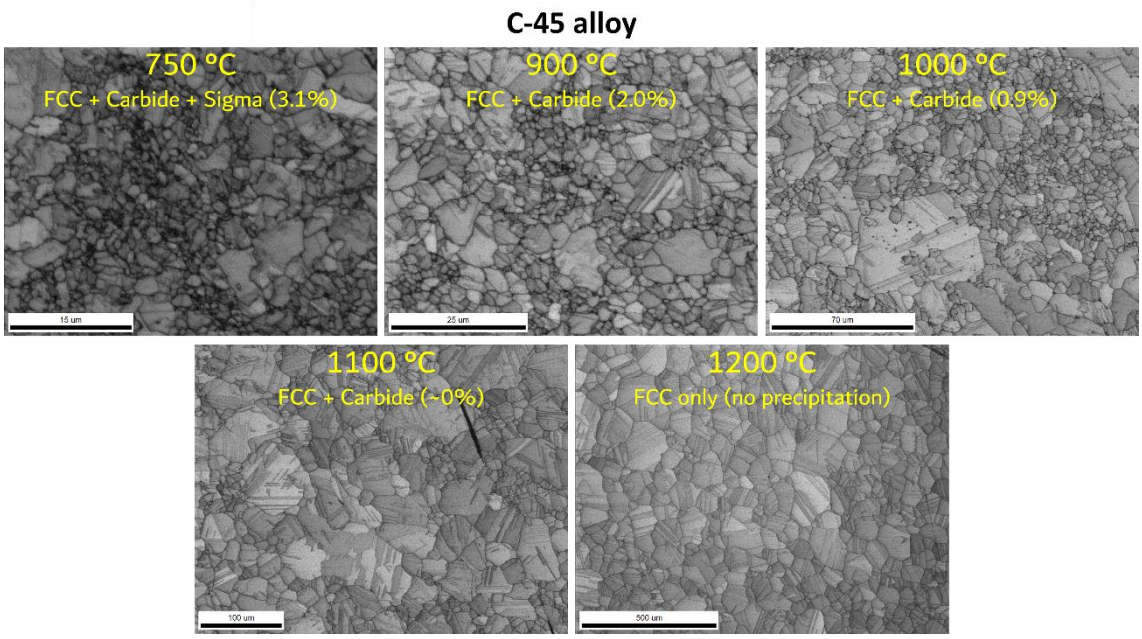

Figure 3.19: SEM-EBSD (image quality) images of the recrystallized samples in different temperatures (C-45 alloy, heat treated for 1h), with the indication of existing precipitates and its fraction.

3.5 Discussion

3.5.1 Phase identification

Based on the XRD and SEM-EBSD-EDS analyses, combined with information from literature and CALPHAD simulations, it was possible to determine the phases present in the different conditions studied, as compiled in Table 3.1. The phase fraction indicated in Table 3.1 was determined via SEM-EBSD.

Table 3.1: Phases present in the recrystallized conditions (1 h). All samples have a matrix of FCC phase, and some samples have a small fraction of other phases as listed in the table. The phase fraction was determined via SEM-EBSD.

	Phases at each recrystallization heat treatment temperature (°C)				
	1200	**1100**	**1000**	**900**	**750**
Base	-	-	-	Sigma 1.8%	Sigma 1.1%
N-10	-	-	-	Sigma	Sigma
N-32	-	-	-	-	Sigma 0.6%
C-17	-	-	-	Carbide + Sigma	Carbide + Sigma 1.4%
C-30	-	-	Carbide ~0%	Carbide + Sigma 2.9%	Carbide + Sigma 2.1%
C-45	-	Carbide ~0%	Carbide 0.9%	Carbide 2.0%	Carbide + Sigma 3.1%

As shown previously, XRD analyses show that all samples have an FCC matrix, and almost all samples treated at 900 and 750 °C have a small fraction of sigma phase, except for N-32 and C-45 (both at 900 °C) which seems to have no sigma phase. It is noted that the addition of either C or N decreases the stability of the sigma phase, since the sigma phase is basically suppressed in samples with higher concentrations of N and C (at 900 °C). This behavior is predicted by CALPHAD simulations, as shown in Figures 3.1 and 3.2 of the experimental procedure section. In literature, Jodi, Park and Park (2020) also observed that N decreases the stability of the sigma phase in Cantor's alloy (CrMnFeCoNi) [115]. It is an interesting result because the sigma phase is typically considered detrimental due to its brittle nature [45], and its suppression expands the processing window for achieving a single-phase FCC matrix.

No evidence of carbides and nitrides was found in any diffractogram. Light atoms such as C and N have low atomic scattering factor, which results in a low structure factor for carbides and nitrides, and therefore very small peaks in the diffractogram compared to the FCC matrix [116]. For low phase fractions, the peaks related to carbides and nitrides can be undetectable via conventional XRD.

Although XRD does not indicate the presence of carbides and nitrides, SEM-EDS analyses confirmed the presence of carbides in almost all C-doped samples, as illustrated in Figure 3.20. Above 1000 °C the sigma phase does not form in these alloys,

so the observed precipitates in Figure 3.20 are likely only $M_{23}C_6$ carbides. These carbides are formed mainly by Cr but have some Co and Ni content in their composition, which agrees with the literature and previous studies of the group [103]. No carbides were observed in samples C-17 above 1000 °C, in C-30 above 1100 °C, and in C-45 above 1200 °C, which is close to what CALPHAD simulations predicted in Figures 3.1 and 3.2.

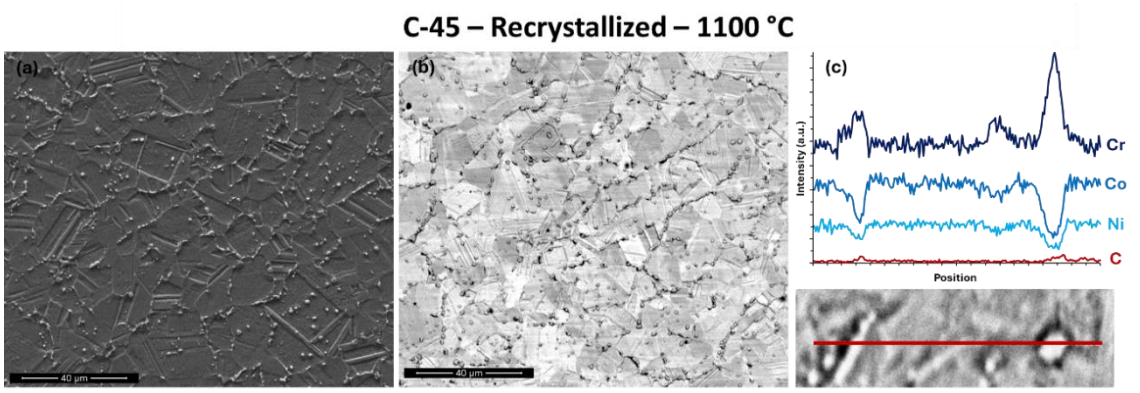

Figure 3.20: SEM analysis of the C-45 alloy in recrystallized condition (1100 °C, 1h) Illustrating the presence of carbides. (a) SE image; (b) BSE-ECCI image; and (c) EDS line scan.

On the other hand, neither XRD nor SEM-EDS-EBSD analyses show evidence of nitrides in the N-doped samples, although CALPHAD simulations (Figures 3.1 and 3.2) indicated that, under thermodynamic equilibrium conditions, there should be a fraction of M_2N-type nitrides for most of the conditions studied in this work. The absence of these nitrides may be justified by the kinetic factors or because, contrary to what CALPHAD indicates, these nitrides are not stable under the temperatures and compositions studied. $M_{23}C_6$ carbides have the same cubic crystal structure as the FCC matrix (space group Fm-3m, nº 225), which favors their rapid formation. On the other hand, M_2N nitrides have a trigonal structure (space group P-31m, nº 162), considerably hindering their formation. In the literature of similar alloys [111–114], the formation of M_2N nitrides was only reported for higher N contents, around 1.0 to 2.0 at%, which requires other production methods than conventional melting.

Finally, phase indexing via EBSD was not satisfactory to differentiate sigma phase and carbides, but it is possible to conclude about the presence of these phases with XRD and EDS analyses, as discussed in this topic. Despite this, SEM-EBSD

allows the measurement of the precipitate fraction (sigma + carbides, when both are present).

3.5.2 Grain and crystallite size

The grain/crystallite size data are compiled in Tables 3.2 and 3.3, respectively, and for ease of interpretation, only grain size data are plotted against the C or N content (at%) in Figure 3.21, since crystallite size follows the same trends that will be discussed below for grain size. Before interpreting grain size data, it is essential to contextualize an important grain refinement mechanism known as Zener pinning [108,112,117]. During grain growth, moving grain boundaries can be pinned by precipitates and have their movement limited due to the difficulty or impossibility of crossing these precipitates. As grain size increases, the driving force for grain growth decreases and may become insufficient to overcome the precipitates, so that grain growth stagnates. In summary, the presence of precipitates can contribute to a reduction in grain size, depending on the fraction, size and distribution of the precipitates, in addition to the heat treatment conditions.

Table 3.2: FCC grain size (excluding annealing twin boundaries) (μm) in recrystallized conditions (1 h).

FCC grain size (μm) at each recrystallization heat treatment temperature (°C)					
	1200	**1100**	**1000**	**900**	**750**
Base	103.3 ± 7.5	50.6 ± 0.3	20.0 ± 0.3	3.1 ± 1.1	1.5 ± 0.03
N-10	67.5 ± 2.2	41.0 ± 3.0	16.9 ± 0.7	2.6 ± 1.1	1.7 ± 0.9
N-32	71.1 ± 6.4	34.4 ± 1.4	13.6 ± 0.3	4.9 ± 0.7	1.8 ± 0.4
C-17	130.7 ± 9.5	68.7 ± 1.4	11.8 ± 0.7	2.8 ± 1.3	1.8 ± 0.3
C-30	97.2 ± 19.4	45.1 ± 1.3	11.6 ± 0.1	2.1 ± 0.4	1.5 ± 0.2
C-45	44.5 ± 2.5	18.8 ± 0.1	4.1 ± 0.7	2.1 ± 0.6	1.6 ± 0.7

Table 3.3: FCC crystallite size (accounting for both grain and annealing twin boundaries) (μm) in recrystallized conditions (1 h).

FCC crystallite size (μm) at each recrystallization heat treatment temperature (°C)					
	1200	**1100**	**1000**	**900**	**750**
Base	31.5 ± 0.01	19.2 ± 2.0	9.3 ± 1.4	1.8 ± 0.7	0.9 ± 0.1
N-10	23.3 ± 1.3	15.4 ± 2.4	7.7 ± 1.5	1.6 ± 0.6	0.9 ± 0.3
N-32	23.1 ± 2.0	14.4 ± 1.5	7.0 ± 1.4	2.6 ± 0.3	0.9 ± 0.2
C-17	40.7 ± 4.3	22.5 ± 2.3	4.8 ± 0.4	1.7 ± 0.5	0.9 ± 0.2
C-30	31.1 ± 5.3	18.2 ± 1.5	4.9 ± 0.4	1.2 ± 0.4	0.8 ± 0.1
C-45	17.8 ± 1.5	7.6 ± 2.4	2.6 ± 0.8	1.2 ± 0.4	0.8 ± 0.4

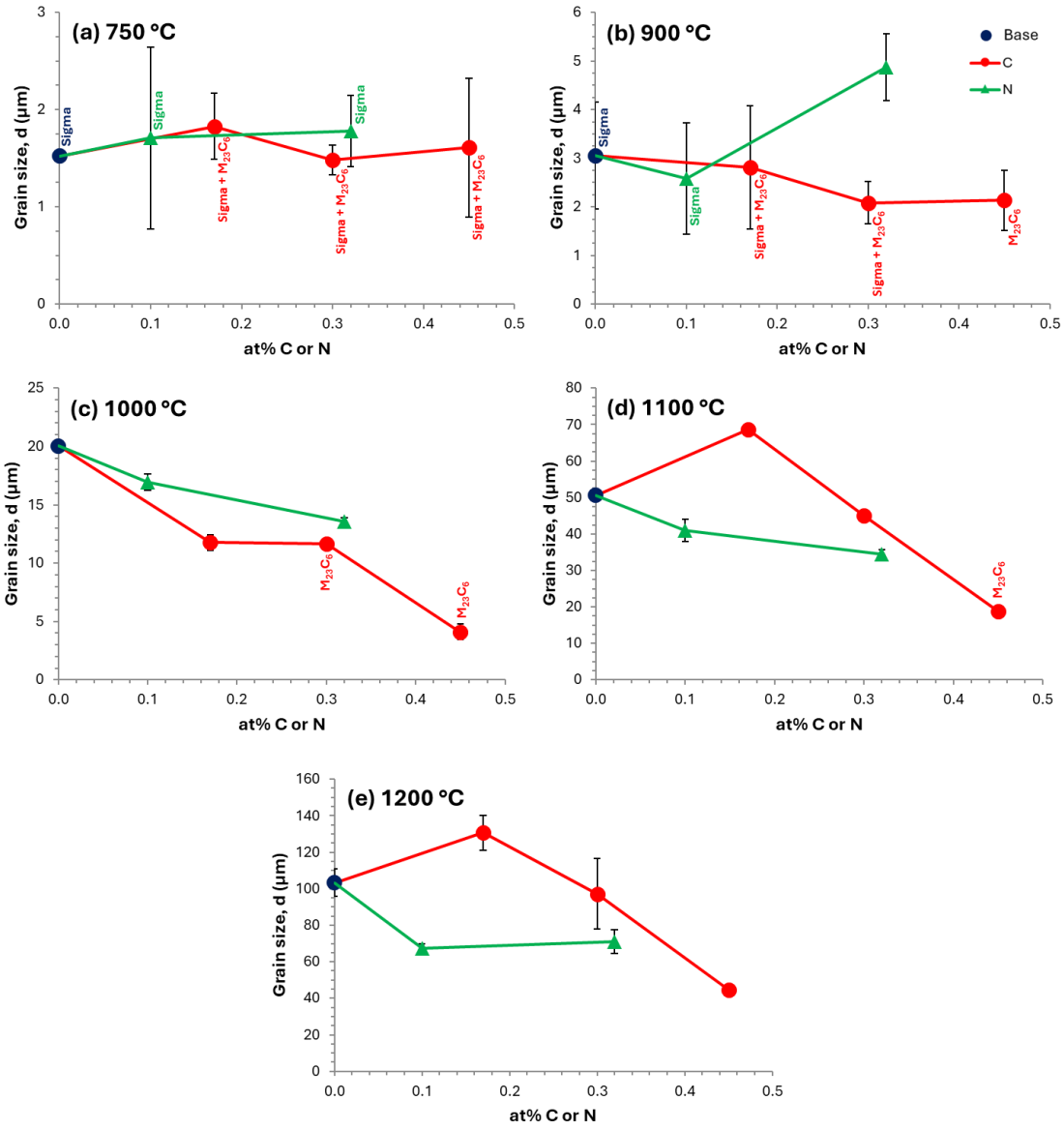

Figure 3.21: FCC grain size (excluding annealing twin boundaries) in recrystallized conditions (1 h) plotted against the C or N content (at%). Indication of existing precipitates (sigma and/or $M_{23}C_6$ carbides) next to each icon. When uncertainty bars are not visible, they are smaller than the corresponding icon.

Analyzing the N-doped samples (in green), at temperatures where the Base alloy presents sigma phase (750 and 900 °C), the N addition tends to increase the grain size because it disfavors the sigma phase precipitation, which was pinning the grain boundaries. Therefore, with fewer sigma phase precipitates in the N-doped samples, the tendency is for the grains to grow more. Sigma precipitates were suppressed in sample N-32 (900) and the grain size increased significantly. On the other hand, at temperatures

where the Base alloy does not present sigma phase precipitates (1000, 1100, and 1200 °C), N showed a tendency to decrease the grain size. It can be explained by the slower grain growth kinetics in the N-doped samples, as will be discussed further in Section 3.5.3 (Grain growth kinetics).

Analyzing the samples doped with C (in red), at temperatures where the Base alloy presents sigma phase (750 and 900 °C), the C addition tends to maintain or slightly decrease the grain size, since C disfavors the sigma phase, but forms carbides. Then one precipitate is replaced by the other, although carbides seem to be slightly more efficient than the sigma phase in pinning the grain boundaries, most likely due to differences in the fraction, size and/or distribution of precipitates. On the other hand, at temperatures where the Base alloy does not present sigma phase precipitates (1000, 1100, and 1200 °C), C has a more complex effect, as it increases grain size in some cases, and in other cases C decreases grain size due to both the pinning effect of $M_{23}C_6$ precipitates and the slower grain growth kinetics in the C-doped alloys, the latter case will be discussed further in Section 3.5.3 (Grain growth kinetics).

3.5.3 Grain size distribution

Figure 3.22 shows the FCC grain size distribution in recrystallized conditions (different temperatures for 1 h). The existing precipitates, sigma and/or $M_{23}C_6$ carbides, are shown in parentheses in the legend. It can be observed that all samples have a monomodal grain size distribution.

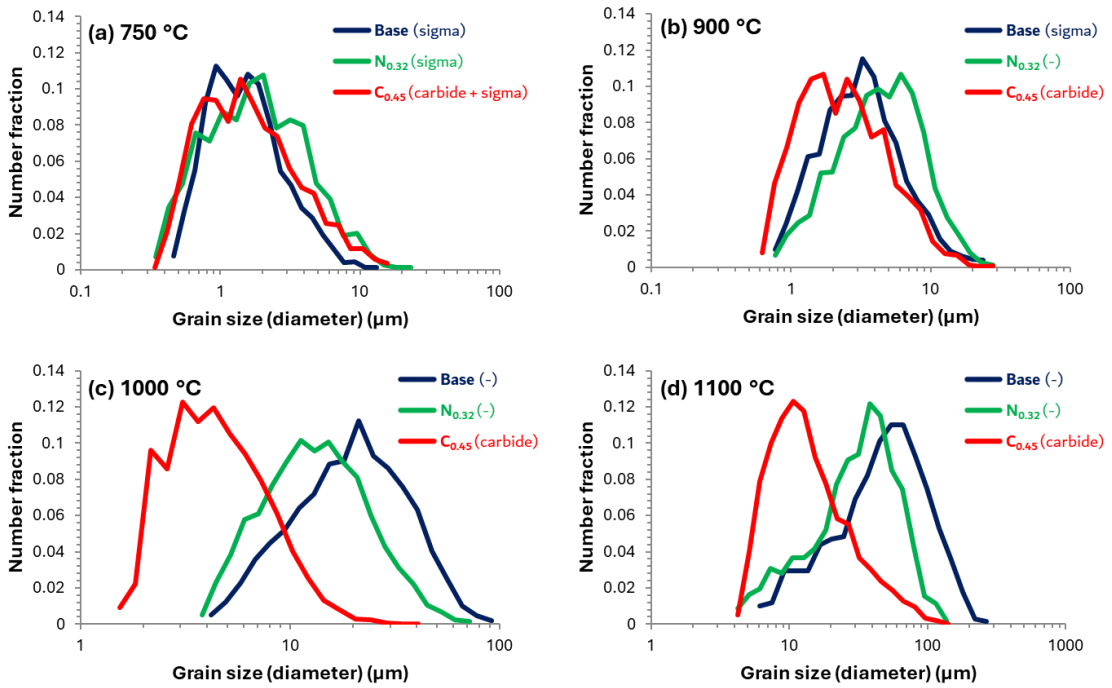

Figure 3.22: FCC grain size distribution in recrystallized conditions (1 h). Indication of existing precipitates (sigma and/or $M_{23}C_6$ carbides) in parentheses.

In the presence of precipitates, where grain refinement occurs through the pinning mechanism, heterogeneous (abnormal) grain growth can occur at high temperatures if the particles coalesce or dissolve, and some grain boundaries break free from this mechanism before others [101]. Although visually in SEM-EBSD images some samples show a high frequency of both small and large grains, the grain size distribution graphs reveal that no sample showed a bimodal distribution due to heterogeneous grain growth. Actually, it is observed that all samples showed a monomodal grain size distribution. In cases where there are precipitates, a positive skewness (or right-skewed) distribution is observed, characterized by a longer tail on the right side.

3.5.4 Grain growth kinetics

To further explore the effect of C- and N- doping on grain size, the grain growth kinetics were evaluated according to the classical kinetic theory for grain growth [97,118]. This theory can be described by Equation 3.2, where d (µm) is the grain size

after t hours of annealing, d_0 (μm) is the initial grain size before the recrystallization, n is the grain growth exponent, and K is a kinetic constant, both are temperature dependent. Some references use the inverse exponent in this equation (n instead of $1/n$), care must be taken because in this formulation the physical trends related to the grain growth exponent are reversed.

$$d^{1/n} - d_0^{1/n} = K.t \quad \textbf{Eq. 3.2}$$

Typically, d_0 loses its physical meaning and is much smaller than d for cold-rolled specimens [97,119], so the expression can be simplified as Equation 3.3, and it can be linearized as Equation 3.4, where the grain growth exponent (n) becomes the slope in a ln(d) vs ln(t) plot.

$$d^{1/n} = K.t \quad \textbf{Eq. 3.3}$$

$$ln(d) = n.ln(K) + n.ln(t) \quad \textbf{Eq. 3.4}$$

For this analysis, the alloys underwent heat treatments at 1000 °C for different times (1, 4, and 12 h), allowing for recrystallization and grain growth. The grain size results are shown in Table 3.4 and Figure 3.23(a). At this condition, the Base, N-10, N-32, and C-17 alloys were FCC single-phase without precipitates. The C-30 alloy showed some carbide precipitates, but these carbides accounted for an insignificant phase fraction, so these alloys were included in the grain growth kinetics analysis. On the other hand, the C-45 alloy was not included in this analysis due to the significant fraction of carbide precipitates and the variation in the carbide fraction for the different treatment times, which makes the grain growth kinetics analysis by this method inconsistent and unreliable. Figure 3.23(b) shows the ln(d) vs ln(t) plot, where the slope corresponds to grain growth exponent (n). The Base alloy has n = 0.32, and this value decreases to 0.22 with N additions, and to 0.26 and 0.15 with gradual C additions.

Table 3.4: FCC grain size (excluding annealing twin boundaries) (μm) after heat treatment at 1000 °C for different times (1, 4, and 12 h), and grain growth exponent (*n*) of the doped alloy compared to the Base alloy.

FCC grain size (μm) after t (h) at 1000 °C				
	1 h	**4 h**	**12 h**	**Grain growth exponent (*n*)**
Base	20.0 ± 0.3	31.9 ± 1.8	44.8 ± 3.0	0.32
N-10	16.9 ± 0.7	20.2 ± 1.2	29.4 ± 1.2	0.22 (**-31%**)
N-32	13.6 ± 0.3	19.3 ± 0.1	23.2 ± 0.8	0.22 (**-31%**)
C-17	11.8 ± 0.7	15.9 ± 0.7	22.7 ± 4.6	0.26 (**-19%**)
C-30	11.6 ± 0.1	15.7 ± 0.6	16.6 ± 0.1	0.15 (**-53%**)

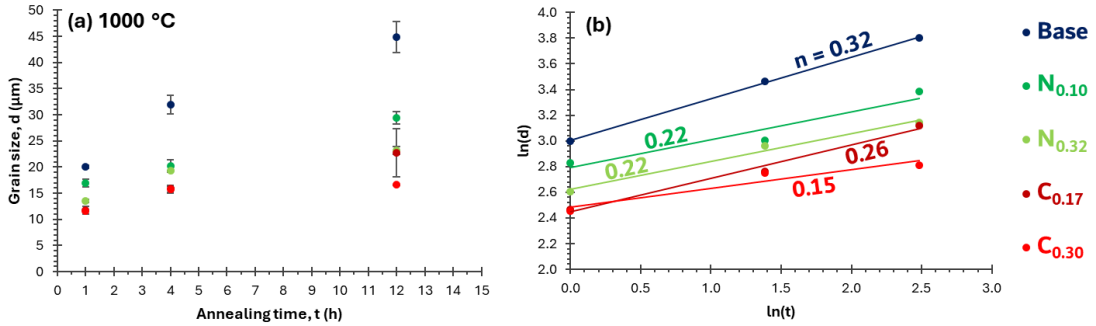

Figure 3.23: (a) Grain size (*d*) as a function of annealing time (*t*) after heat treatment at 1000 °C; and (b) ln(*d*) vs ln(*t*) plot, where the slope corresponds to grain growth exponent (*n*). When uncertainty bars are not visible, they are smaller than the corresponding icon.

Physically, the reduction of *n* represents a reduction in boundary mobility, making grain growth slower [96–99]. The smaller the *n* value, the easier it is to obtain a more refined grain structure. The N addition (both 0.10 and 0.32 at%) reduced *n* from 0.32 to 0.22, while the addition of 0.17 at% C reduced *n* from 0.32 to 0.26, and the addition of 0.30 at% C reduced it even further to 0.15. Through this analysis, it is possible to infer that both N and C retard the grain growth kinetics of the $Cr_{40}Co_{40}Ni_{20}$ alloy, facilitating the obtaining of more refined structures.

The grain growth kinetics can be delayed by different factors [11], such as: the sluggish diffusion effect due to lattice distortion; the solute drag effect due to the presence of solute atoms and their possible segregation to the grain boundaries; the pinning effect due to the presence of precipitates that pin the grain boundaries; etc.

The pinning effect by precipitates is not relevant in this case, because the grain growth exponent (*n*) was obtained from samples without precipitates (or with a negligible fraction of precipitates). The sluggish diffusion effect may occur due to lattice distortion caused by interstitial atoms, but this mechanism is not considered one of the most relevant with regard to microstructural refinement. The solute drag effect of C and N solute atoms is still a controversial topic in literature [11], some works observed negligible effects [13–15], while some others observed noticeable effect on grain refinement [16–19]. Basically, the solute drag mechanism should reduce grain boundary mobility, because the moving boundaries has to overcome or drag a solute atmosphere that exerts a delaying force on it [96–100]. In the current work, it is not possible to reliably conclude about the mechanism that retards grain growth kinetics, but based on the literature, it most likely occurs by the solute drag effect, although the sluggish diffusion effect cannot be ruled out.

Regardless of the mechanism, the slower grain growth kinetics in doped alloys justifies the reduction in grain size of the N- and C-doped samples, compared to the Base alloy, in cases where there are no precipitates in Section 3.5.2 (Grain and crystallite size). In cases where precipitation occurs, grain refinement also happens through the pinning mechanism.

3.6 Conclusions

From the $Cr_{40}Co_{40}Ni_{20}$ MPEA, different N- and C-doped alloys were designed, produced, and thermomechanically treated under different conditions. This allowed the study of phase equilibria, precipitate formation, and grain refinement capacity. The following conclusions were drawn:

1) For all alloys, the homogenization heat treatment (1200 °C, 2h) resulted in a single-phase FCC structure, with no precipitation. Cold-rolling process triggered a strain-induced phase transformation, the TRIP effect, where the FCC phase was partially transformed into an HCP phase. The martensitic HCP phase was completely dissolved after recrystallization heat treatments (>750 °C, 1h).

2) Sigma phase precipitates (less than 1.8%) in heat treatments below 1000°C (for 1h), but N and C increase the stability of the FCC phase against the sigma phase, reducing or suppressing sigma phase precipitation in N- and C-doped samples. It is an interesting result since sigma phase is often undesirable due to its brittle character, and its suppression broadens the processing window of these alloys.

3) No nitride precipitation was observed under any condition in the N-doped alloys, even the addition of 0.32 at% N did not lead to the formation of nitrides in $Cr_{40}Co_{40}Ni_{20}$ alloy. On the other hand, $M_{23}C_6$ carbide precipitation (less than ~2%) was observed under various conditions in the C-doped alloys.

4) When precipitation did not occur, the slower grain growth kinetics of C- and N-doped alloys induced grain refinement. When precipitation occurred (sigma and/or carbides, in this case), the Zener pinning mechanism also induced grain refinement.

5) All samples showed a monomodal grain size distribution. In cases where precipitation occurred, a positive skewness (or right-skewed) distribution is observed, characterized by a longer tail on the right side.

CHAPTER 4 – Effect of C and N additions on the strain-induced martensite formation and reversion

4.1 Introduction

The previous chapter (Chapter 3: Effect of C and N additions on phase equilibria and grain refinement) focused on inducing grain refinement by interstitial doping in the $Cr_{40}Co_{40}Ni_{20}$ MPEA, and its impacts on phase equilibria. The addition of interstitial elements such as C and N was shown to induce grain refinement through different mechanisms, and this effect is especially favorable in alloys with high grain refinement strengthening component, such as the $Cr_{40}Co_{40}Ni_{20}$ alloy.

However, interstitial doping can significantly modify the deformation mechanisms, and according to review papers [12,20], the influence of C and N on the SFE and TRIP/TWIP effects is still controversial in the literature, and the related explanation is not completely convincing. It is well known that by adjusting the SFE, it is possible to control the deformation mechanisms: only dislocation slip is expected for high SFE alloys (> ~45 mJ/m²), TWIP effect is activated for low/medium SFEs (15 ~ 45 mJ/m²), and FCC to HCP strain-induced transformation (TRIP) is activated for very low SFEs (< ~15 mJ/m²) [28,35,36].

In summary, the addition of C and N should change the SFE and the TRIP/TWIP behavior, depending on the alloy, but their influence is not yet fully understood in the literature. So, there is a need for a more in-depth understanding of how the SFE and TRIP effect are impacted by C- and N-doping, since this addition represents an important microstructural refinement route, and it modifies an important deformation mechanism (TRIP) of the $Cr_{40}Co_{40}Ni_{20}$ alloy.

In this chapter, the analysis of deformed samples allows us to evaluate the influence of the C and N addition on the TRIP deformation mechanism, that is, FCC to HCP strain-induced transformation. In Chapter 2 (Influence of grain size on strain-induced phase transformation), it was observed that grain size has no effect on TRIP as long as the evaluation is done at the same deformation level. Therefore, in this chapter, precautions were taken to ensure that all samples had the same deformation level through controlled cold rolling processing.

Furthermore, *in situ* SXRD analyses during heating (dilatometry) allow the study of the reversion (HCP to FCC transformation) of HCP martensite formed during deformation. SXRD analyses during heating also contribute to the study of the influence of C and N on recrystallization and grain growth. This last piece of information can complement the study in Chapter 3 (Effect of C and N additions on phase equilibria and grain refinement) regarding the grain refinement capacity of doped samples.

4.1.1 Objectives

At this chapter, the $Cr_{40}Co_{40}Ni_{20}$ alloy doped with different C and N contents were studied under cold deformation and continuous heating. The goal of this chapter was to evaluate the strain-induced martensite transformation (TRIP effect), the SFE, the martensite reversion during annealing, the recrystallization and grain growth temperatures, and the influence of C and N interstitial elements on these features.

The XRD and SEM-EBSD analyses in deformed samples (cold-rolled) revealed the occurrence and extent of the TRIP effect by measuring the fraction of martensite HCP phase formed. XRD in different recrystallized samples provided data to evaluate the SFE of these alloys. *In situ* SXRD analyses during heating provided data to evaluate the martensite reversion by measuring the phase fraction along continuous heating, and to evaluate the recrystallization and grain growth temperatures through the dislocation density quantification and the texture of FCC Debye-Scherrer rings along the azimuthal angle (using coefficient of variation).

4.2 Literature review

4.2.1 Effect of C-doping on deformation mechanisms and SFE

Stepanov et al. (2017) [120], studying Cantor alloy (CrMnFeCoNi) doped with 1.0 at% C, observed that the C addition retards mechanical twinning (TWIP effect) during deformation. The changes in the contribution of different deformation mechanisms were attributed to increase in SFE due to C-doping.

Li (2019) [121], studying Cantor alloy (CrMnFeCoNi) doped with 0.2, 0.5, and 0.8 at% C, observed that the C addition decreases the density of mechanical nano-twins (TWIP effect), an indication that C acts to increase the SFE. They also showed that C leads to a higher energy barrier to recrystallization during annealing, retards the recrystallization while compositional homogeneity is not crucial to that.

Shang et al. (2019) [14] measured the SFE of C-doped CrCoNi samples using the distance between partial dislocation in transmission electron microscopy (TEM), and observed that C addition (at least in higher contents) increased the SFE, in addition to postponing the TWIP effect. Samples doped with 0.10, 0.25 and 0.75 at% C showed SFE equal to 21 ± 2, 24 ± 2 and 29 ± 3 mJ/m², respectively, while SFE of the undoped CrCoNi alloy was reported between 18 ± 4 mJ/m² [25] and 22 ± 4 [21]. In other alloy systems such as TWIP steels [122] and Fe-Cr-Ni-based stainless steels [123], it is also reported that C increases SFE.

Ikeda et al. (2019) [124], studying C-doping in the Cantor alloy (CrMnFeCoNi) by first-principles calculations, observed that C stabilizes the FCC phase as compared to the HCP phase, indicating that SFE increases due to C alloying. In the ideal quenched condition, the SFE change is 7 mJ/m² for each 1 at% C added to the alloy.

Moravcik et al. (2022) [125] concluded that C alloying increases the SFE in the CrCoNi alloy, through calculations based on both density functional theory and thermodynamic modeling of the Gibbs free energy with the CALPHAD method.

Bae et al. (2022) [126] compiles some works showing that C increases the SFE in steels, as shown in Figure 4.1, but in their own work they find a non-linear relationship in which low C content slightly decreases the SFE, and the addition of higher C contents increases the SFE (red lines in Figure 4.1). The same behavior was observed by Petrov (2005) [127] (black line in Figure 4.1). The literature suggests that this non-linear behavior is caused by competition between the effects of short-range order and dynamic strain aging [114][128], as detailed in the next section on N-doping.

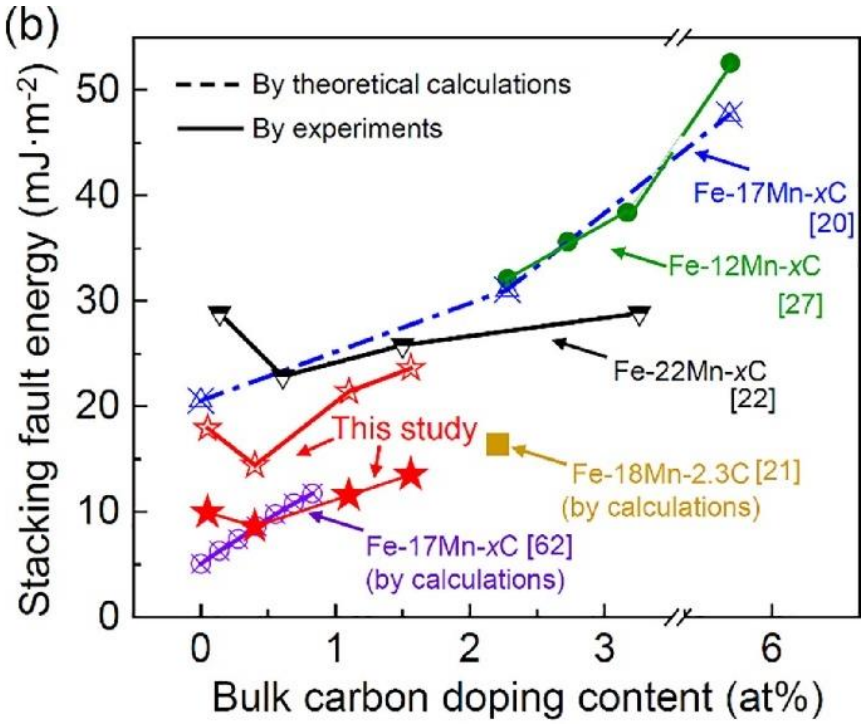

Figure 4.1: SFE as a function of C content in Fe-Mn-C systems (by at%), determined from theoretical calculations (dotted lines) and experiments (continuous lines) [126].

On the other hand, Wu; Parish; Bei (2015) [129] observed that mechanical twinning (TWIP) is more pronounced when adding 0.5 at% C in the Cantor alloy (CrMnFeCoNi), suggesting that the SFE is decreased by the addition of C.

Wang et al. (2016) [130], studying the $Fe_{40}Ni_{11}Mn_{35}Al_8Cr_6$ alloy doped with 0.07, 0.16, 0.30, 0.55 and 1.10 at% C, concluded that SFE decreases with increasing C content, which also contributes to the transition from wavy slip to planar slip. They measured SFE using the distance between partial dislocation in TEM and the obtained values were 22.2 ± 1.9, 20.1 ± 1.0, and 10.2 ± 0.9 mJ/m² for 0.00, 0.07, and 1.10 at% C, respectively. They argue that this occurs once the C has also found to inhibit dislocation cross-slip because of the increase of lattice friction stress [131].

Abbasi et al. (2011) [132], using first-principles calculations, conclude that C-doping increases the SFE of Fe-C alloys, and this increase is more significant when the C is located near the stacking faults. They argue that although some experimental work reports that C decreases or does not alter SFE, this is due to local heating during measurement, which causes C to diffuse away from the stacking faults, reducing the experimentally measured SFE.

Overall, the effect of C-doping on the SFE remains a matter of active debate in literature [12]. Most studies report that C addition increases the SFE [14,120–125,132], based on both indirect evidence from suppressed TWIP activity during deformation and direct or semi-direct estimations of SFE, including TEM measurements of partial dislocation separation and first-principles or CALPHAD-based calculations. In contrast, other works suggest that C may decrease the SFE [129,130], mainly inferred from enhanced mechanical twinning or transitions in deformation mode, which are interpreted as signatures of lower SFE, or from direct measurements of SFE. Additionally, some authors report non-linear or composition-dependent behavior [126,127], where low C contents slightly reduce SFE while higher additions increase it. Therefore, discrepancies arise not only from differences in alloy systems and compositions, but also from the methodology used to estimate SFE, making it clear that the influence of C on SFE cannot be treated as universal and must be analyzed in the context of composition, temperature, and measurement approach.

4.2.2 Effect of N-doping on deformation mechanisms and SFE

Klimova et al. (2020) [114] and Xiong et al. (2020) [133] observed that N-doping in the Cantor alloy (CrMnFeCoNi) suppresses the TWIP effect, indicating an increase in SFE in these alloys. The same conclusion was obtained by Traversier (2021) [15] in the CrMnFeNi alloy. A similar evidence was found by Moravcik et al. (2020) [13] in the CrCoNi alloys, in which N alloying reduces deformation twinning (TWIP), also indicating an increase in SFE.

Petrov (2022) [134], through thermodynamic calculations, observed that N alloying increases the SFE of FeCrNiMn austenitic steels.

Moravcik et al. (2022) [125] concluded that N-doping increases the SFE of the CrCoNi alloys, through both simulation and experimental method. They use calculations based on density functional theory and thermodynamic modeling of the Gibbs free energy with the CALPHAD method. Experimentally, TEM measurements of the width of partials showed that the SFE of CrCoNi increases from 22 to 43 mJ/m² by adding 0.5 at% N. Furthermore, they showed that N is more effective than C in increasing SFE at room temperature.

On the other hand, Chung et al. (2021) [18], studying the Cantor alloy (CrMnFeCoNi) with high N content (3.5 at% N), observed an earlier appearance of mechanical twins (TWIP effect) in N-doped alloy, suggesting that N addition decreases the SFE in Cantor alloy. Gavriljuk and Berns (1999) [135] showed that N addition in a Cr15Mn17 steel reduces the SFE and led to a pronounced twinning during deformation.

Simmons (1996) [20], in a review paper on high-N alloying in stainless steels, discusses that the literature is divided on the effect of N on SFE and deformation mechanisms, and compiles papers that show contradictory effects. Some works indicate that N increases tendency to planar slip and TWIP (indicating a decrease in SFE), other works indicate that N suppresses TRIP in austenitic stainless steels (indicating an increase in SFE), and some authors discussed that N and C promotes planar slip regardless of the SFE value.

Overall, in the case of N-doping, the literature also presents conflicting trends regarding its influence on SFE [12,20]. Most studies report that N addition increases the SFE [13,15,114,125,133,134], in some cases even more pronounced than C-doping at comparable concentrations, while other studies report a decrease in SFE [18,20,135]. The other assumption commonly encountered in literature is the addition of certain amounts of N can suppress mechanical twinning in TWIP steels due to short-range order (SRO). Strong affinity between Cr and N atoms result in atom couple formation which in turn leads to SRO, which benefits planar slip and suppresses twinning because local SRO needs to be destroyed on certain planes for twin growth. On the other hand, at higher N concentrations, dynamic strain aging makes slip more difficult and twinning can prevail again [114]. Similar questions are considered about the impact of C on the SFE [128], it seems possible that C might have a similar effect to that of N.

4.3 Experimental procedure

4.3.1 Alloy design, production, and thermomechanical processing

The same six alloys designed in Chapter 3 were used in this chapter, namely: Base alloy ($Cr_{40}Co_{40}Ni_{20}$), N-10, N-32, C-17, C-30, and C-45 (with 0.10 and 0.32 at% N; and 0.17, 0.30, and 0.45 at% C, respectively). Alloy production, thermomechanical processing, and recrystallization heat treatments are the same as those described in

Chapter 3. Basically, samples were homogenized at 1200 °C for 2 h with water quenching and cold-rolled with a thickness reduction of ~50% to study the formation of HCP phase (TRIP effect) during deformation. Recrystallization heat treatments were performed in a muffle furnace, for 1 h, at different conditions of temperatures: 750, 850, 900, 1000, 1100, 1150, and 1200 °C, to study the deformation/stacking fault probability (SFP) and stacking fault energy (SFE) via XRD peak shift. More details about SFP and SFE calculations will be shown in Section 4.5.1.

4.3.2 Sample preparation and XRD/SEM analysis methodology

Samples were carefully prepared according to standard metallographic preparation, up to a final stage of at least 15 h in a vibratory polisher with a 0.04 μm colloidal silica suspension. This stage is important in TRIP alloys for removing any transformed phase layer from the surface region formed in the cutting and grinding processes.

XRD experiments were done in a PanAnalytical Empyrean XRD, as shown in Figure 4.2. The beam was calibrated to focus on the sample in a rectangular region of ~6x7 mm to ensure that multiple grains could be analyzed even in the larger grain size samples. A camera (Figure 4.2(a)) was used to center the samples, and a height adjustment device (Figures 4.2(b,c)) was used to ensure that all analyses were performed at the same height. These adjustments were essential for this work, since a change in the sample height can alter the position of the peaks and severely impair the SFP and SFE calculations that depend on the comparison between the peak positions of different samples. SEM analyses were done in Tescan S8252G Raman SEM (Figure 4.2(d)) equipped with energy-dispersive X-ray spectroscopy (EDS) and electron backscatter diffraction (EBSD) detectors.

The phase fractions were quantified by two methods: i) area fraction via EBSD analyses; and ii) volumetric fraction through the area below the XRD peaks using Equations 2.3 and 2.4, as detailed in Chapter 2.

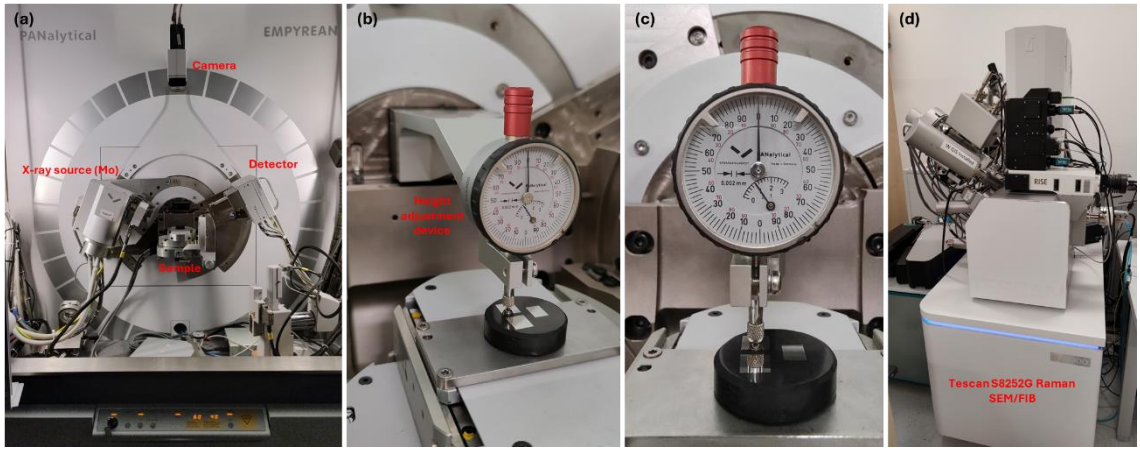

Figure 4.2: (a) PanAnalytical Empyrean XRD; (b,c) height adjustment device in the XRD; and (d) Tescan S8252G Raman SEM (EBSD).

4.3.3 *In situ* synchrotron X-ray diffraction analysis during heating (dilatometry)

Three alloys (Base, N-32, and C-30) were previously deformed by cold rolling (from ~9 mm to ~5 mm, ~44% cold reduction) to generate an FCC + HCP structure, samples were machined into cylinders 10 mm long by 3 mm in diameter. The main purpose of this analysis was to evaluate the effect of N and C on the HCP dissolution and the FCC recrystallization and grain growth during heating.

In situ SXRD was performed during a heating cycle and dilatometry, at the P07 beamline at Deutsches Elektronen-Synchrotron (DESY/ PETRA III), Hamburg, Germany [136]. A heating rate of 20 °C/min was used. A monochromated 102.85 KeV high-energy beam was used, with a corresponding wavelength of 0.120548 Å. This high photon energy allowed to perform diffraction experiments in transmission mode in relatively thick samples, enabling the determination of bulk microstructural information. LaB_6 powder was used as a standard for the calibration of the instrument parameters and to determine the sample-to-detector distance (1615 mm). A two-dimensional Perkin Elmer detector (pixel size of 200 µm x 200 µm, array size of 2048 x 2048) was used to collect the 2D raw Debye-Scherrer rings at different temperatures, as shown in Figure 4.3(a).

In order to index the phases, calculate the phase fraction and the FCC dislocation density, the 2D Debye-Scherrer rings were converted into conventional 1D diffraction patterns (intensity vs 2θ) by integrating along the full azimuthal angle (φ range from -180 to 180°) using 1024 points, the maximum resolution of the PerkinElmer detector, as represented in Figure 4.3(a) and 4.3(b). Integration was done using a combination of Python-based tools [137]. Peaks were individually fitted by a pseudo-Voigt function to determine key peak parameters such as peak position, peak intensity, full width at half maximum (FWHM), and area under the peak. The phase fraction was quantified through the area below the SXRD peaks using Equations 2.3 and 2.4, as detailed in Chapter 2. The FCC dislocation density was determined by the modified Williamson-Hall method using the full azimuthal integration data from six FCC peaks (111, 200, 220, 311, 222, and 400), after subtracting the instrumental broadening via the LaB_6 standard. More details about the methodology for calculating dislocation density via the modified Williamson-Hall method can be found in the supplementary material (Section S2).

In order to assess the temperature at which recrystallization and grain growth occurs, the 2D Debye-Scherrer rings were converted into 2D diffraction patterns (intensity vs 2θ vs azimuthal angle φ) along the full azimuthal angle (φ range from -180 to 180°) using 1024 points, and along a radial range of 2.5 to 4.5° to include the 111 and 200 FCC rings, using 1080 points, as represented in Figure 4.3(a) and 4.3(c). Integration was done using a combination of Python-based tools [137]. A region of interest (ROI) was delimited around 111 (2θ = 3.31 ± 0.12°) and 200 (2θ = 3.81 ± 0.12°) FCC rings, as shown in Figure 4.3(c). This ROI was integrated into a 1D intensity profile (intensity vs azimuthal angle φ), as represented in Figure 4.3(c) and 4.3(d). A metric called coefficient of variation (CV) (Equation 4.1) was applied, which measures the relative variation of the intensity profile, capable of identifying when a textured Debye-Scherrer ring becomes homogeneous (the moment when recrystallization occurs) and when discrete spots appear (grain growth).

$$CV = \frac{std(I)}{mean(I)} \quad \textbf{Eq. 4.1}$$

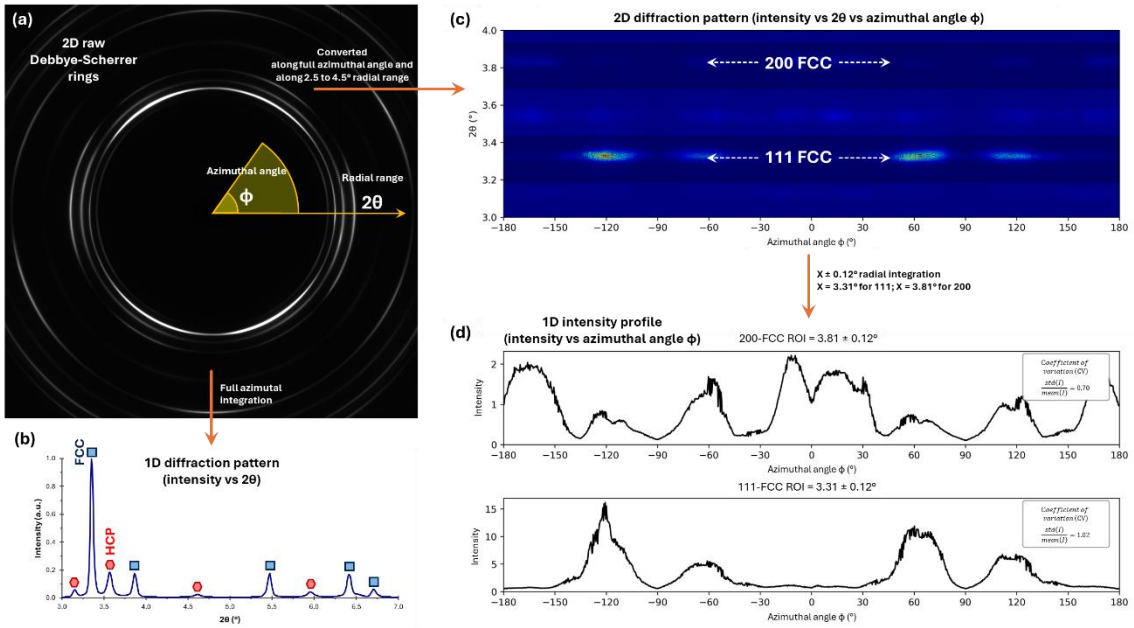

Figure 4.3: *In situ* SXRD data processing representation. (a) 2D raw Debye-Scherrer rings collect at each temperature. (b) Conventional 1D diffraction patterns (intensity vs 2θ) obtained by integration along the full azimuthal angle, to index the phases and calculate the phase fraction. (c) 2D diffraction patterns (intensity vs 2θ vs azimuthal angle φ) and (d) 1D intensity profile (intensity vs azimuthal angle φ) obtained by integration along a radial range around 111 and 200 FCC rings. A metric called coefficient of variation (CV) was applied to assess the temperature at which recrystallization and grain growth occurs.

To the author's knowledge to date, the method used in this work (evaluating the texture of Debye-Scherrer rings along the azimuthal angle through the CV to finding the temperature at which recrystallization and grain growth occurs) has not yet been published in the literature. Most published methods related to this topic tend to use quantifications based on peak parameters such as relative orientation intensity, peak width for calculating dislocation density, or other parameters [138–141].

Peak broadening and dislocation density analyses are sensitive to detecting recovery and recrystallization. In contrast, the azimuthal CV proposed here remains responsive to the statistical distribution of diffracting grains, enabling not only the detection of recrystallization through angular homogenization of the Debye-Scherrer rings, but also the identification of subsequent diffraction-detectable grain growth via the emergence of spotty diffraction patterns. Therefore, defect-based metrics track the annihilation of stored deformation via recovery and recrystallization, whereas the CV analysis captures the recrystallization and the transition to microstructural coarsening (grain growth), making both approaches physically complementary.

4.4 Results

4.4.1 Strain-induced martensite formation in cold-rolled samples

A sample of each alloy in the cold-rolled condition (50% cold rolling thickness reduction) was characterized. Figure 4.4 shows the diffractograms and Figure 4.5 shows the microscopy analyses at the same magnification (1000x), both indexed with the FCC + HCP phase, highlighting a strain-induced phase transformation (TRIP effect), where the FCC phase partially transforms into HCP phase during deformation. Microscopy images show that the HCP phase (in green in Figure 4.5) has a lamellar morphology that mostly crosses the original grains throughout their entire length, which agrees with a previous work with the Base alloy [7,142].

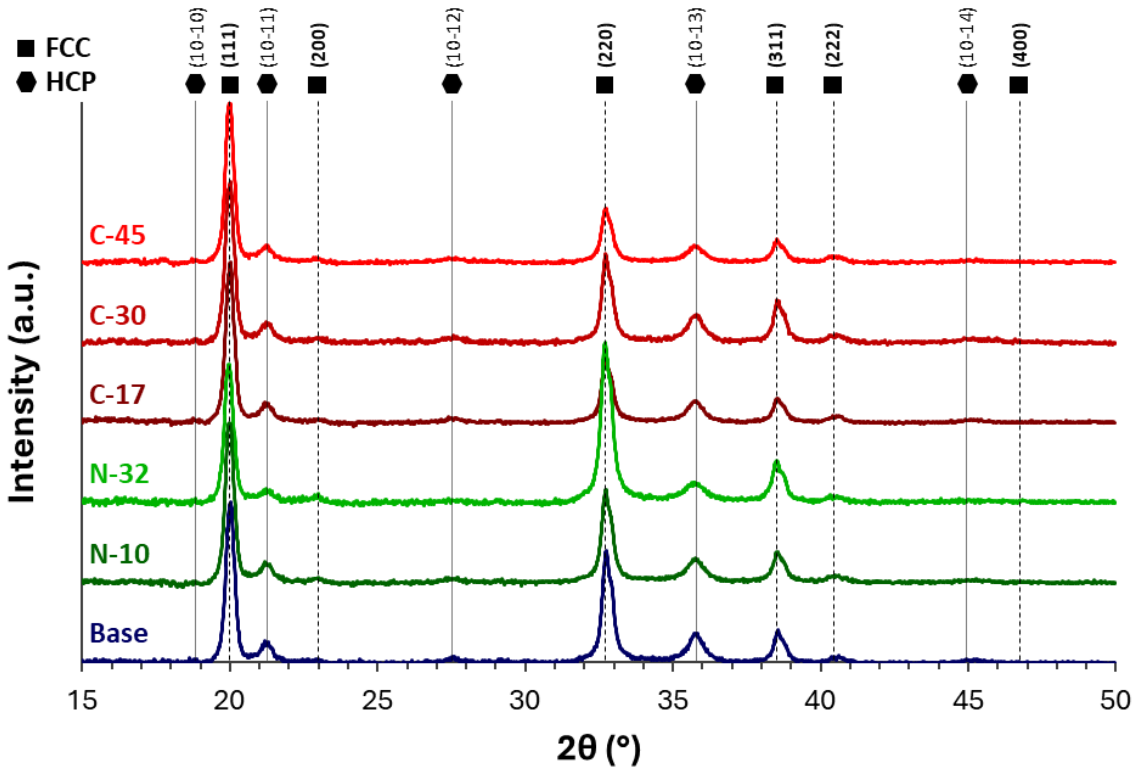

Figure 4.4: XRD analyses of the cold-rolled condition (50% cold reduction). The FCC phase partially transforms into HCP phase during deformation (TRIP effect).

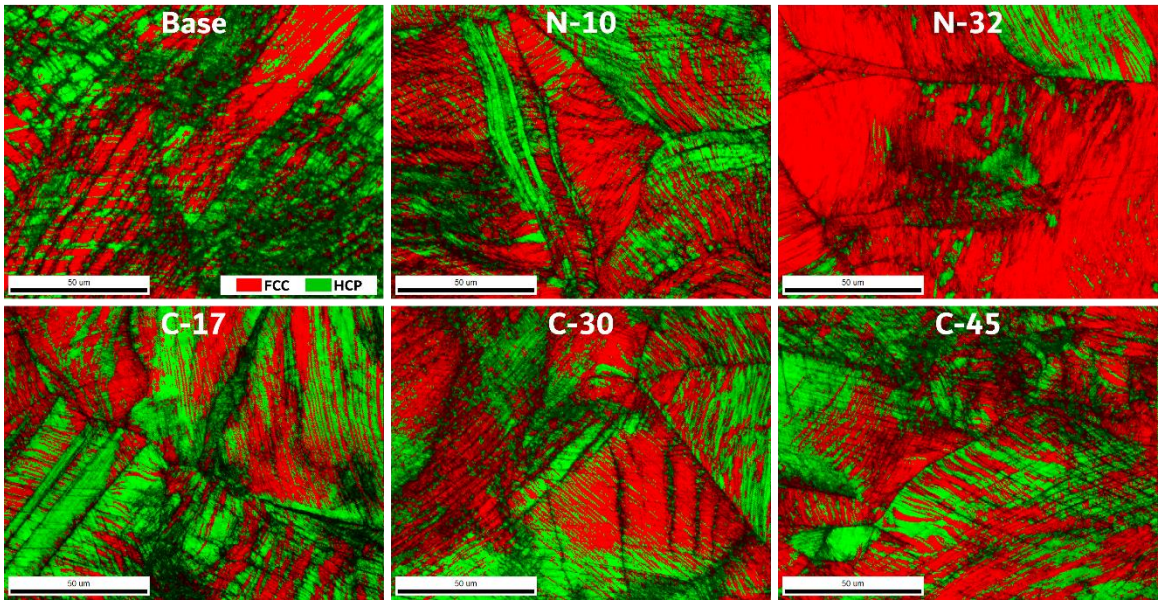

Figure 4.5: SEM-EBSD (phase + image quality) images of the cold-rolled condition (50% cold reduction). Images at the same magnification (1000x). The FCC phase partially transforms into HCP phase during deformation (TRIP effect).

The phase fractions quantified by both methods, XRD and EBSD, are shown in Table 4.1 and Figure 4.6. Although the phase fraction analysis via EBSD has its limitations as it evaluates a relatively small and superficial region (~ 140 x 110 μm, in this case), the values obtained by both methods are relatively close for each sample.

It is observed that the N addition has a strong tendency to reduce the transformed phase fraction (HCP), that is, disfavoring the TRIP effect. Regarding the C addition, there is no obvious trend, but higher C levels lead to a slight decrease in the HCP fraction, also hindering TRIP effect. It is important to note that this comparison between samples is valid since all samples underwent the same strain level of ~50% during the cold-rolling stage. The effect of N and C additions on SFE, and consequently on the characteristics of the TRIP effect, will be discussed in a dedicated section later.

Table 4.1: HCP fraction obtained by both XRD and EBSD methods. The value in parentheses is the HCP fraction of the doped alloy compared to the Base alloy.

Sample	HCP fraction via XRD (%)	HCP fraction via EBSD (%)
Base	45.3	56.4
N-10	43.3 (**-4%**)	45.4 (**-20%**)
N-32	29.2 (**-36%**)	20.1 (**-64%**)
C-17	48.4 (**+7%**)	58.0 (**+3%**)
C-30	47.7 (**+5%**)	47.2 (**-16%**)
C-45	43.6 (**-4%**)	48.7 (**-14%**)

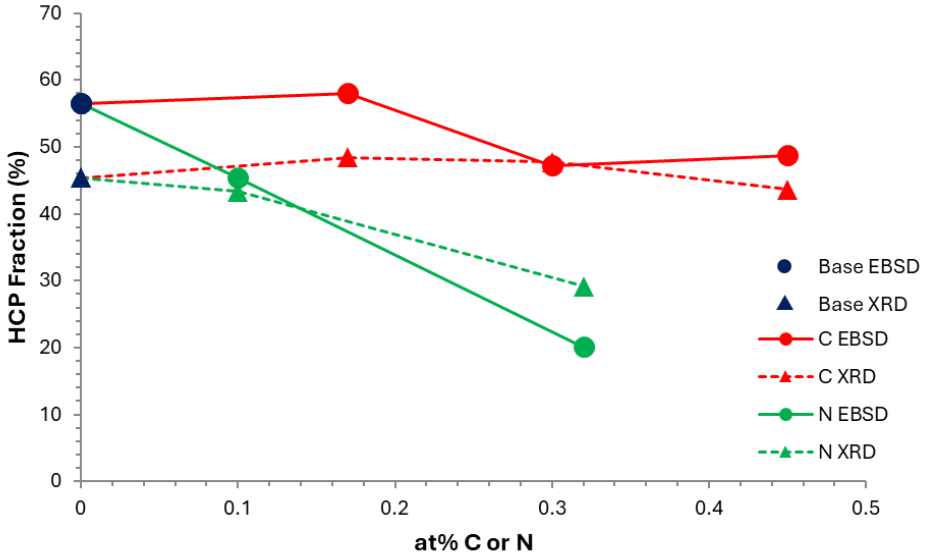

Figure 4.6: Strain-induced HCP fraction obtained by both XRD and EBSD methods.

4.4.2 Strain-induced martensite reversion, recrystallization and grain growth by *in situ* heating

Three alloys (Base, N-32, and C-30), previously deformed by cold rolling to generate an FCC + HCP structure, were analyzed by *in situ* SXRD during a heating cycle and dilatometry. The main purpose of this analysis was to evaluate the effect of N and C on the HCP dissolution and the FCC recrystallization and grain growth during heating.

Figure 4.7 shows the area diffraction patterns of the Base alloy during heating (the other samples exhibit similar general behavior). The previously deformed sample has FCC + HCP rings (Figure 4.7(a)). By increasing temperature, two simultaneous processes occur: i) the dissolution of the HCP phase after the disappearance of the HCP rings; and ii) the recrystallization of the FCC phase after the textured FCC rings become homogeneous (Figure 4.7(b)). Subsequently, at higher temperatures, the FCC grain growth occurs, and the FCC rings become a set of resolvable spots (Figure 4.7(c)). The HCP dissolution temperature and the FCC recrystallization and grain growth temperatures for each alloy will be obtained and discussed later.

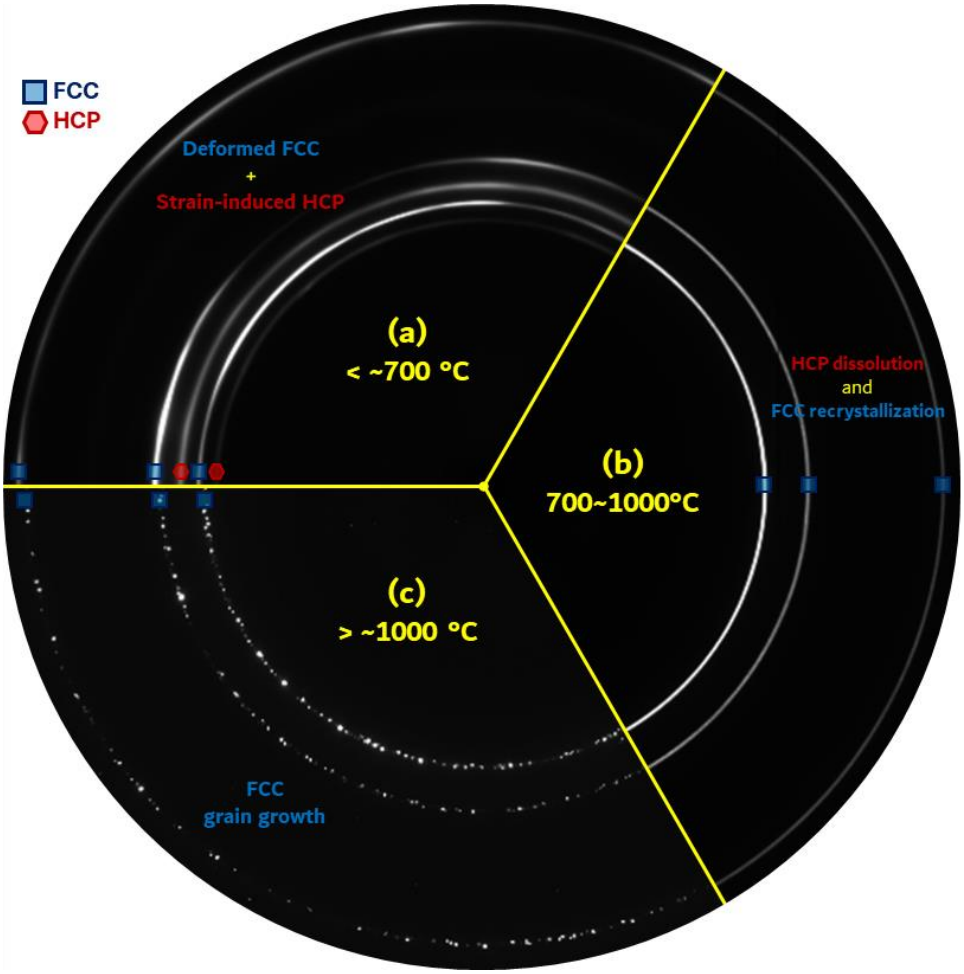

Figure 4.7: Area diffraction pattern during heating in the dilatometry test for the Base alloy. The other alloys exhibit the same general behavior: (a) the previously deformed sample has FCC + HCP rings; (b) dissolution of the HCP phase after the disappearance of the HCP rings, and recrystallization of the FCC phase after the textured FCC rings become homogeneous; and then (c) FCC grain growth that causes the FCC rings to become a set of resolvable spots.

In order to index the phases, calculate the phase fraction and dislocation density, a full azimuthal integration was performed. The Debye-Scherrer rings were converted into conventional diffraction patterns (intensity vs 2θ), which are shown in Figure 4.8. Figure 4.8(a) shows the X-ray diffractograms throughout the test vs temperature for the Base alloy (the other alloys exhibit the same general behavior). Initially, at room temperature (23 °C), all alloys have an FCC + HCP structure (see Figure 4.8(b)), then the HCP phase is completely dissolved at ~800°C. A small fraction of the sigma phase forms and is dissolved between ~800 and 1000°C. It is estimated that the sigma phase appears in a very small fraction, since the sigma peaks are less than 1% of the height of the main FCC peak for Base alloy, they are even smaller in the C-doped alloy, and there is no sigma in the N-doped alloy (see Figure 4.8(c)), therefore, the sigma phase will not be included in the phase fraction calculation. Finally, all alloys have a single-phase FCC structure above ~1000°C (see Figure 4.8(d)).

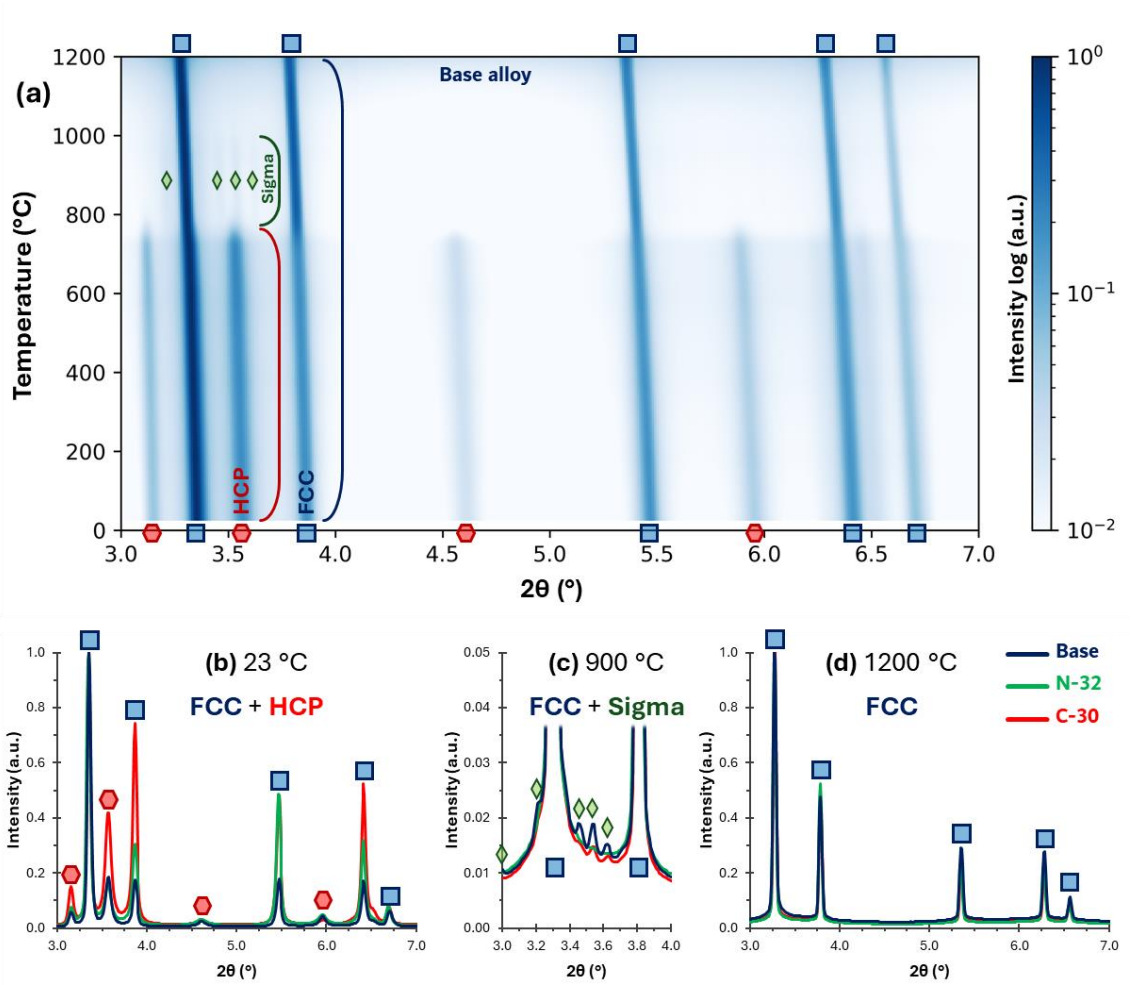

Figura 4.8: *In situ* SXRD during heating in the dilatometry test. (a) X-ray diffractograms throughout the test vs temperature for the Base alloy (the other alloys exhibit the same general behavior). Initially, all alloys have an FCC + HCP structure; the HCP phase is dissolved at ~800°C; a small fraction of the sigma phase forms and is dissolved between ~800 and 1000°C for Base and C-doped alloys (N-doped alloy has no sigma); and all alloys have a single-phase FCC structure above ~1000°C. (b) Diffractogram at 23 °C, illustrating an FCC + HCP structure for all alloys. (c) Diffractogram at 900 °C, with zoom showing the small fraction of sigma phase in the FCC matrix for Base and C-doped alloys (N-doped alloy has no sigma). (d) Diffractogram at 1200 °C, illustrating a single-phase FCC structure for all alloys.

The phase fraction for all alloys was calculated through the area below the SXRD peaks, and it is plotted during heating in Figure 4.9 along with its temperature derivative to facilitate the identification of the HCP to FCC transformation onset and end. For all alloys, the HCP phase maintains a constant fraction up to ~700 °C and only then begins to dissolve, respecting a logistic or sigmoidal behavior, typical of phase transformations [29]. The transformation inversion point (minimum on the derivative

plot) occurs at a slightly lower temperature for the Base alloy (~745 °C) compared to the doped alloys (~765 °C).

It is not possible to reliably measure the end of phase transformation (when HCP fraction becomes zero), because, at the end of transformation, HCP peaks exhibit similar intensities to the background noise, hindering their detection. In the script programmed to find and fit the peaks, it was determined that HCP peak fitting were reliable as long as the peak height was higher than 0.02% of the maximum intensity of the diffractogram or as long as the uncertainty related to height was less than the height of the HCP peak itself. As a result, the data becomes unreliable after a certain point in the test (~800 °C in this case), and the transformation end is not accurately detected. However, extrapolating from the curves, it is estimated that the HCP phase is completely dissolved at ~810 °C for Base alloy and ~830 °C for doped alloys.

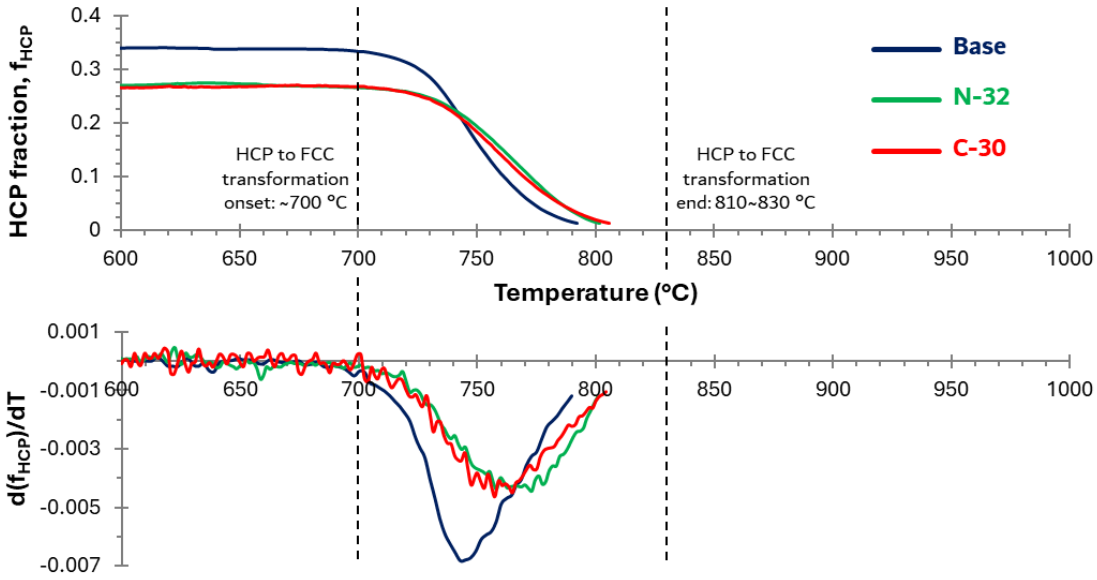

Figure 4.9: Dissolution of the HCP phase during heating in the dilatometry test: HCP phase fraction (f_{HCP}) and its temperature derivative (df_{HCP}/dT) for identifying the HCP to FCC transformation onset and end (which occurs between ~700 and 830 °C).

The FCC dislocation density for all alloys was determined by the modified Williamson-Hall method, and it is plotted during heating in Figure 4.10 along with its temperature derivative. Initially, all alloys present a high dislocation density plateau, since they are deformed. Doped alloys exhibit a higher density of dislocations than the undoped alloy, and this is consistent with what is observed in the literature, both for C

[14,120] and N [133,143] doping. The dislocation density remains at a plateau followed by a slight decrease above ~600 °C, which is likely related to a weak recovery process, which tends to be almost or completely suppressed in low SFE alloys. Then, a sharp decrease occurs at ~700 °C, indicating the recrystallization process of the FCC matrix. Finally, all alloys reach a plateau of lower dislocation density: above ~760 °C for Base alloy, and above ~800 for doped alloys. It is an indication that N- and C-doping slightly delays the recrystallization process, similar to what was observed in the HCP dissolution.

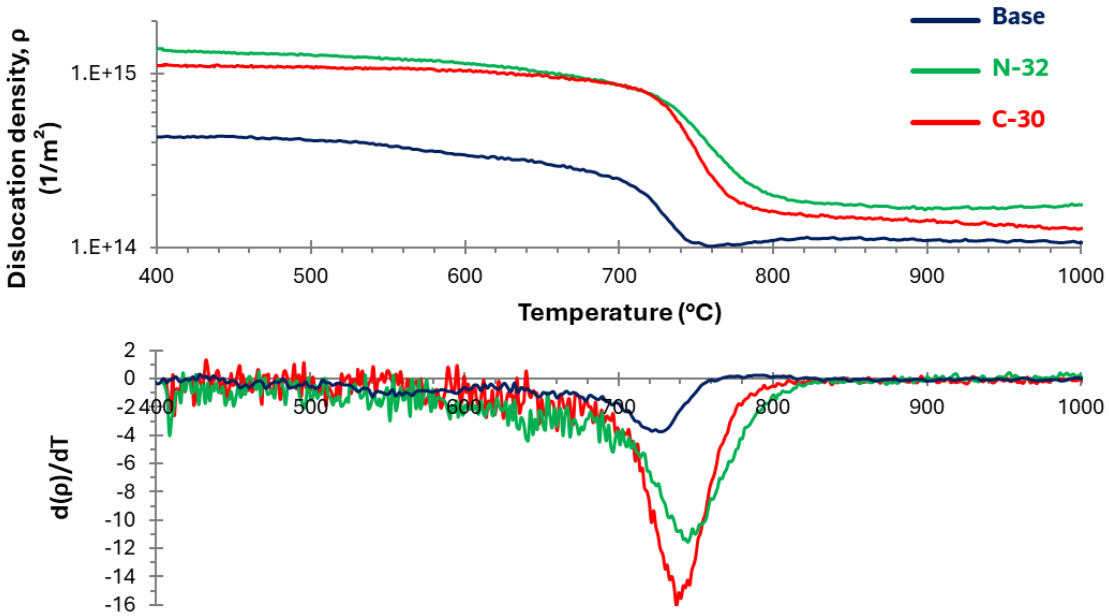

Figure 4.10: Dislocation density (ρ) of the FCC phase during heating and its temperature derivative ($d\rho/dT$).

In order to assess more deeply the temperature at which recrystallization and diffraction-detectable grain growth occurs, an integration along a radial range around 111 and 200 FCC rings was performed, as already shown in Figure 4.3 in the methodology. The Debye-Scherrer rings were converted into 1D intensity profile (intensity vs azimuthal angle φ) for each temperature. The coefficient of variation (CV = std/mean) (Equation 4.1) was calculated for each intensity profile throughout the heating to assess the temperature at which FCC recrystallization and diffraction-detectable grain growth occurs.

The CV measures the relative variation of the intensity profile along the azimuthal angle. In the initial deformed condition, the FCC rings are textured along the azimuthal angle (see Figure 4.7(a) previously shown), resulting in higher CV values. After recrystallization, the FCC rings tend to become much more homogeneous along the azimuthal angle (Figure 4.7(b) previously shown), resulting in lower CV values. Finally, with grain growth, the FCC rings become a set of resolvable and intense spots (Figure 4.7(c) previously shown), resulting again in higher CV values, but now occurring at higher temperatures. Therefore, CV is capable of identifying when a textured Debye-Scherrer ring becomes homogeneous, the moment when recrystallization occurs, due to the initial drop in CV value (see Figure 4.11 below), and identifying when discrete spots appear, the onset of diffraction-detectable grain growth regime, which is related to grain growth, due to the increase in CV value at higher temperature (see Figure 4.11 below).

Figure 4.11 shows the CV and its temperature derivative for the 111 and 200 FCC rings for all three alloys. According to CV-111 and its derivative (Figure 4.11(a)), recrystallization begins at ~700 °C for all samples and ends at ~800 °C for the C-doped sample and ~850 °C for the others. According to CV-200 and its derivative (Figure 4.11(b)), recrystallization also begins at ~700 °C for all samples but ends at ~800 °C for the non-doped sample and ~830 °C for the others. Basically, CV-111 and CV-200 do not indicate a strong influence of N and C on the FCC recrystallization temperature, although there is a difference of up to ~50 °C in CV-111, this difference does not occur for the same sample in CV-200.

Regarding FCC diffraction-detectable grain growth regime, according to both CV-111 and CV-200 and their derivatives, it begins at ~1000-1010 °C for Base alloy, ~1020-1030 °C for C-doped alloy, and ~1040-1050 °C for N-doped alloy. It indicates that doping with C and especially N delays the onset of the grain growth process, which agrees with the literature [11,144].

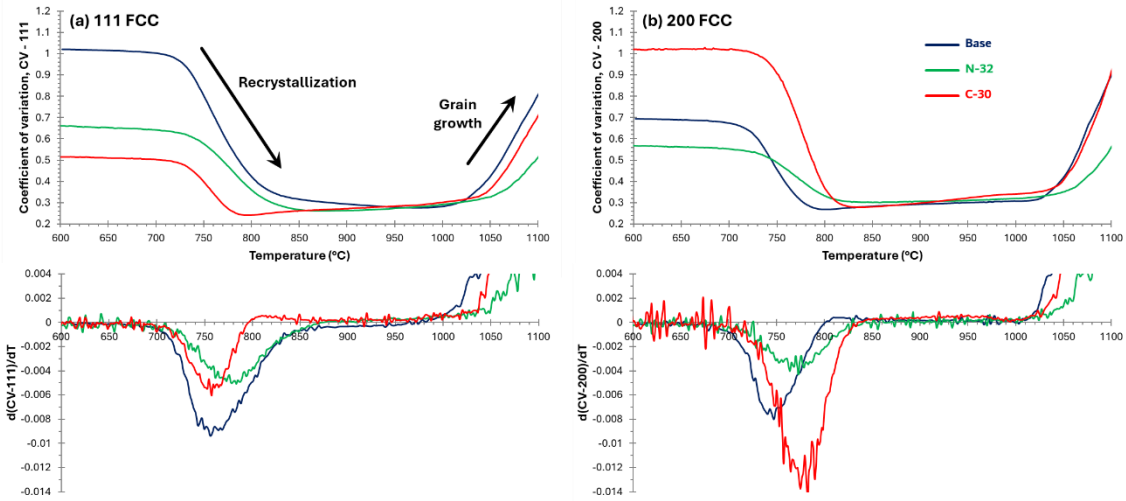

Figure 4.11: Coefficient of variation (CV) and its temperature derivative (dCV/dT) during heating for identifying the temperature at which FCC recrystallization and grain growth occurs, calculated for (a) 111 FCC and (b) 200 FCC rings.

In analyses with continuous heating, there is a dynamic component that must be considered, the temperatures at which the HCP to FCC phase transformation, recrystallization, and grain growth occur were obtained for a heating rate of 20 °C/min. Altering the heating rate, these phenomena can occur at different temperatures due to the shorter or longer time available for them to happen during heating. The use of heat treatments at constant temperature can generate different results from continuous heating. For example, the heat treatment at 750 °C for 1 h, shown in Chapter 3, led to a fully recrystallized single-phase FCC microstructure. In this chapter, using continuous heating, the HCP dissolution and recrystallization were still incomplete at 750 °C, since there was not enough time during heating at 20 °C/min to complete these processes at that temperature. Furthermore, the recrystallization temperature depends on several factors, such as the deformation level previously applied to the material. The greater the deformation, the greater the stored energy, and the lower the temperature required for recrystallization [138]. In this work, the comparison between the alloys is valid because they all underwent the same thermomechanical processing and prior cold deformation.

In order to assess if the FCC recrystallization and HCP dissolution processes occur simultaneously, Figure 4.12 shows HCP fraction, CV-111, and CV-200 with their temperature derivative for all three alloys. The results show that the onset of HCP dissolution and FCC recrystallization are indeed simultaneous for all alloys, occurring

at a temperature of ~700 °C. The FCC dislocation density also shows a sharp drop at ~700 °C for all alloys (previously shown in Figure 4.10), indicating the onset of FCC recrystallization. This is strong evidence that the dissolution of the HCP phase, that is, the HCP to FCC transformation, occurs due to the formation of new deformation-free FCC grains during recrystallization. These new FCC grains should preferentially form in regions of higher stored energy (such as HCP/FCC interfaces, stacking faults, grain boundaries, etc.) and consume the HCP regions in the same way that they consume the deformed FCC regions through grain boundary migration [138]. More details about the mechanism of the martensitic HCP dissolution will be discussed in a dedicated section later.

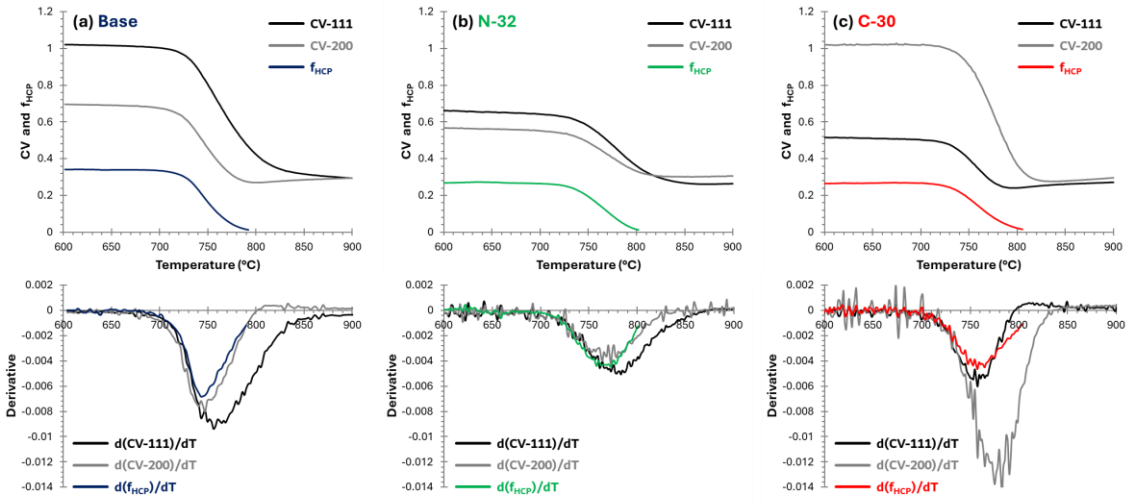

Figure 4.12: HCP phase fraction (f_{HCP}) and coefficient of variation (CV-111 and CV-200) with their temperature derivative (df_{HCP}/dT and dCV/dT) during heating for all alloys: (a) Base alloy, (b) N-32, and (c) C-30. Results show that the onset of HCP dissolution and FCC recrystallization are simultaneous at ~700 °C.

Figure 4.13 shows the dilatometry results at a heating rate of 20 °C/min. The black curves (read on the left vertical axis) correspond to the thermal expansion during heating, and the colored curves (read on the right vertical axis) are the linear thermal expansion coefficient (LTEC), obtained by the temperature derivative of the thermal expansion. The shaded region corresponds to the temperature range in which the HCP dissolution and FCC recrystallization occur (~700 to 830 °C), as observed in the

previous results of this chapter. In this region, a peak-shaped response is observed in the LTEC curve for all alloys, consistent with previous results.

Furthermore, a second phenomenon was observed between 500 and 700 °C for all alloys, which is suspected to be related to short-range order (SRO), already reported in CrCoNi alloys in this temperature range [69,71], but not yet for the composition of this work ($Cr_{40}Co_{40}Ni_{20}$). The first drop in the LTEC value at ~500-550 °C may correspond to the creation of SRO tending to reach the equilibrium quantity at this temperature from the moment diffusion becomes appreciable. Then, the increase in the LTEC value at ~600-650 °C corresponds to the destruction or dissolution of SRO, as it becomes less stable at higher temperatures, similarly to what was observed by Bacurau et al. (2024) [71] when analyzing the specific heat of the CrCoNi alloy via differential scanning calorimetry. In Section 2.5.5 of this thesis (Hypothesis: SRO preventing FCC-HCP transformation), the hypothesis that the $Cr_{40}Co_{40}Ni_{20}$ alloy possesses a certain degree of SRO was also discussed. However, a more detailed study of SRO is beyond the scope of this work.

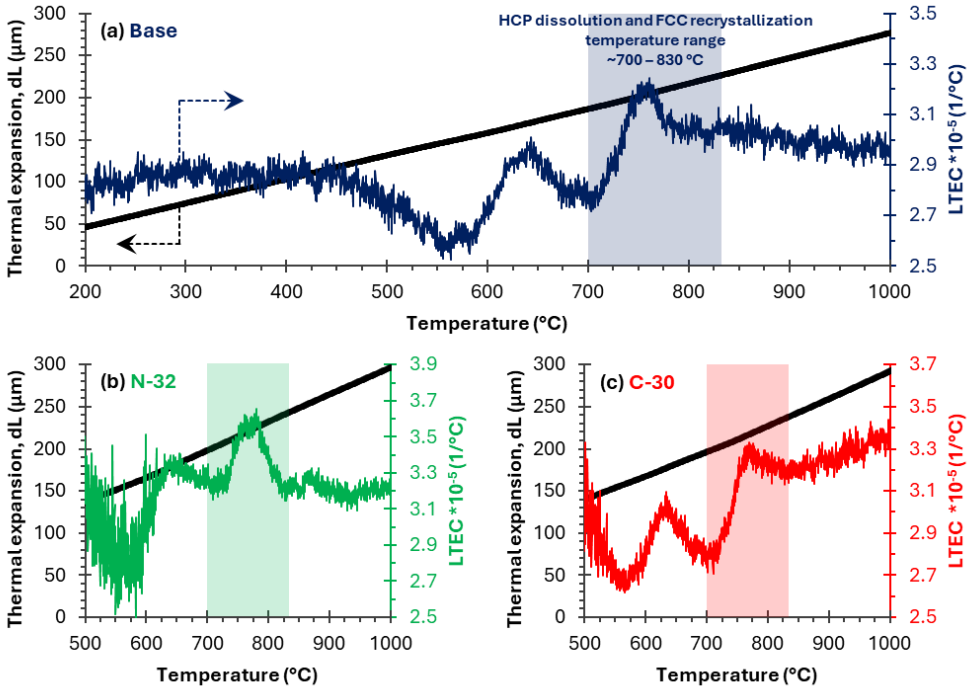

Figura 4.13: Dilatometry results at a heating rate of 20 °C/min. Thermal expansion (black curves) and linear thermal expansion coefficient (LTEC) (colored curves) as a function of temperature for all alloys: (a) Base alloy, (b) N-32, and (c) C-30. The shaded region corresponds to the temperature range in which the HCP dissolution and FCC recrystallization occur (~700 to 830 °C), consistent with previous results of this chapter.

4.5 Discussion

In this section, the effect of C and N additions on SFE and on the formation of strain-induced HCP phase (TRIP effect) will be discussed. The mechanism by which the strain-induced HCP is dissolved during heating will also be discussed.

The effect of C and N additions on recrystallization and grain growth will be discussed in Chapter 5 (General discussion and conclusions) along with the grain refinement and grain growth kinetics results obtained in Chapter 3 (Effect of C and N additions on phase equilibria and grain refinement).

4.5.1 Stacking fault energy (SFE) via X-ray measurements

According to the literature, changes in the type and/or extent of deformation mechanisms (such as the TRIP effect) can be related to changes in the SFE [28,35,36], with the addition of C and N being responsible for these changes. In this section, the SFP and SFE of the alloys were estimated using a method, based on the shift of the XRD pattern peaks, as detailed below. This method is widely used in literature [31,126,145–150], and regardless of its quantitative accuracy, in this work it can be used as a basis for discussion by, at least, enabling a qualitative comparison of the SFE of the alloys.

Strain-hardening in FCC metals can generate stacking faults, mechanical twinning (TWIP) and/or strain-induced HCP phase (TRIP). They can all be interpreted as deformation faults in close-packed planes (111 planes for FCC). In the diffraction pattern, these faults changes the position of FCC peaks in the diffraction angle axis. Interestingly, it changes each hkl peak differently, in different directions for some peaks (as shown in Figure 4.14), which can be used to estimate the deformation/stacking fault probability [151–153]. This method was deduced from the analytical calculation of the diffracted intensities of faulted and perfect crystals.

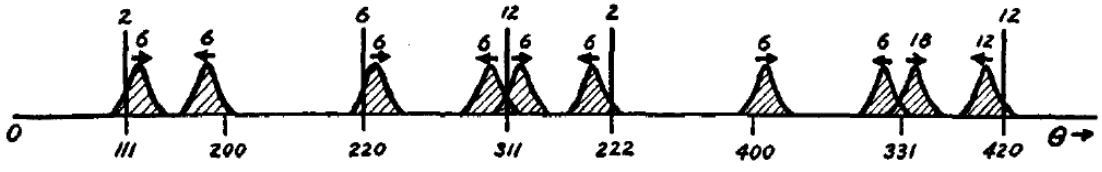

Figure 4.14: Representation of FCC peak displacement due to deformation faults [152].

The deformation/stacking fault probability (α) can be determined through Equation 4.2 [151–153] using the position of the peaks (2θ, in degrees). It is necessary to compare the same sample in two conditions, with faults (wF) and without faults (woF), to obtain the fault probability. C_{hkl} is a constant that depends on the hkl peak (C_{111} = 3.95; and C_{222} = –7.9).

$$\alpha = \frac{\Delta(2\theta)^\circ}{\tan\theta . C_{hkl}} = \frac{2\theta^\circ_{woF} - 2\theta^\circ_{wF}}{\tan\theta . C_{hkl}} \quad \textbf{Eq. 4.2}$$

The displacement of the peaks due to faults is very small and can be camouflaged by other sources of displacement, such as the position of the sample in the diffractometer and changes in the interplanar distance. Therefore, it is advisable not to use the absolute position of a single hkl peak. A more accurate method is to use the relative distance between two peaks, preferably corresponding peaks like 222 and 111, as shown in Equation 4.3.

$$\alpha = \frac{\Delta(2\theta_{222} - 2\theta_{111})^\circ}{(\tan\theta_{222} . C_{222} - \tan\theta_{111} . C_{111})} = \frac{(2\theta_{222} - 2\theta_{111})^\circ_{woF} - (2\theta_{222} - 2\theta_{111})^\circ_{wF}}{(\tan\theta_{222} . C_{222} - \tan\theta_{111} . C_{111})} \quad \textbf{Eq. 4.3}$$

From the XRD data of the samples treated at 750, 850, 900, 1000, 1100, 1150, and 1200 °C, the peaks 111 and 222 of the FCC phase were fitted using a pseudo-Voigt function to measure the 2θ position and the associated measurement uncertainty. Figure 4.15 shows the difference between the positions of the peaks 222 and 111 ($2\theta_{222}$ - $2\theta_{111}$ parameter) for all conditions analyzed. In the plots of Figure 4.15, after removing a few outliers, it was possible to identify two plateaus in all samples, the first one formed between the temperatures of 750 and 900 °C (defined as wF condition), and the second one between the temperatures of 1100 and 1200 °C (defined as woF condition). Then, the parameter $\Delta(2\theta_{222}$ - $2\theta_{111})^\circ$ was obtained for each alloy through the difference between these plateaus, and the fault probability (α) was calculated through Equation 4.3. The values obtained are shown in Table 4.2 and Figure 4.15.

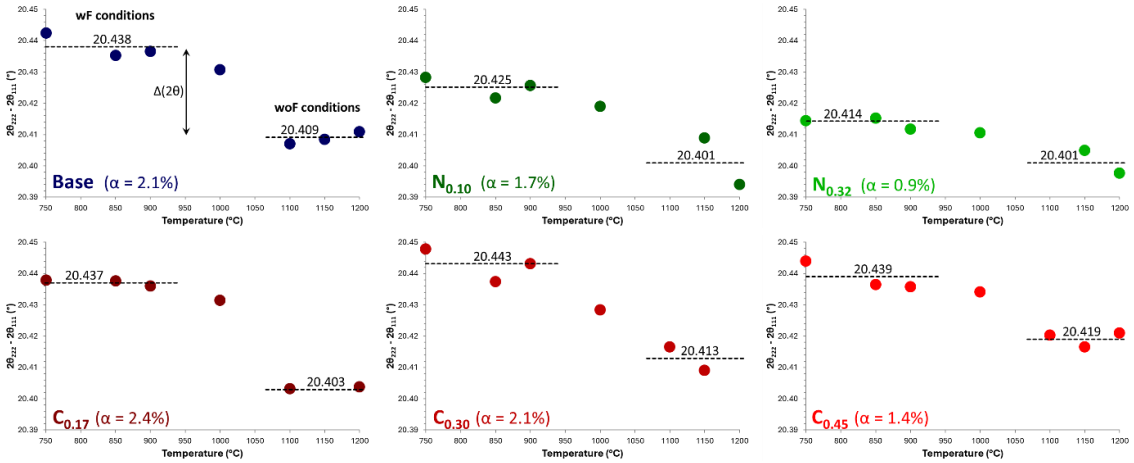

Figure 4.15: Plot of the 2θ separation between (111) and (222) as a function of temperature to calculate the deformation/stacking fault probability (α). The associated uncertainties are on the order of 0.0005 and smaller than the plotted icons.

To obtain the stacking fault energy (γ), it was still necessary to calculate the microstrain in the [111] direction (ε_{111}). According to the literature [31], ε_{111} can be calculated using Equation 4.4, where B is the full width at half maximum (FWHM in radians) and θ is the position, both of the (111) peak of a sample in the condition with faults (wF) (sample treated at 750 °C was used), and ν is Poisson's ratio, used as 0.3. The ε_{111} values and uncertainty are shown in Table 4.2.

$$\varepsilon_{111} = \frac{B^2 \cot^2\theta}{1 + 2\nu^2} \qquad \textbf{Eq. 4.4}$$

Finally, the stacking fault energy (γ) was calculated according to Equation 4.5 [154], where $K_{111}\omega_0$ is a proportionality constant (6.6 for FCC), G_{111} is the shear modulus in the (111) fault plane that is equal to $1/3(C_{44} + C_{11} - C_{12}) = 68.33$ GPa, C_{ij} is an elastic stiffness coefficient ($C_{11} = 193$; $C_{12} = 116$; $C_{44} = 128$ GPa) [155], a_0 is the lattice parameter, A is the Zener anisotropy that is equal to $2C_{44}/(C_{11} - C_{12}) = 3.32$, ε_{111} is the microstrain in the [111] direction, and α is the fault probability for each alloy. The values obtained for SFE and the associated uncertainty are shown in Table 4.2 and Figure 4.16(a). The strain-induced HCP fraction was shown again in this section as Figure 4.16(b) for comparison purposes with the SFE plot.

$$\gamma = \frac{K_{111}\omega_0 \, G_{111} \, a_0 \, A^{-0.37}}{\pi\sqrt{3}} \frac{\varepsilon_{111}}{\alpha} \qquad \textbf{Eq. 4.5}$$

Table 4.2: Deformation/stacking fault probability (α), microstrain (ε_{111}), and stacking fault energy (γ).

	$\Delta(2\theta_{222} - 2\theta_{111})°$ (10^{-4})	SFP, α (%)	$FWHM_{111}$ at 750 °C (Radians, 10^{-6})	Microstrain at 750 °C, ε_{111} (10^{-6})	SFE, γ (mJ/m²)
Base	-293 ± 4	2.06 ± 0.03	1535 ± 7	5.80 ± 0.05	5.3 ± 0.1
N-10	-237 ± 5	1.67 ± 0.03	1477 ± 5	5.47 ± 0.04	6.2 ± 0.1
N-32	-125 ± 5	0.88 ± 0.03	1375 ± 7	4.87 ± 0.05	10.5 ± 0.4
C-17	-337 ± 5	2.37 ± 0.03	1607 ± 7	6.27 ± 0.05	5.0 ± 0.1
C-30	-300 ± 6	2.11 ± 0.04	1719 ± 7	7.43 ± 0.06	6.6 ± 0.1
C-45	-194 ± 4	1.37 ± 0.03	1648 ± 7	6.62 ± 0.06	9.1 ± 0.2

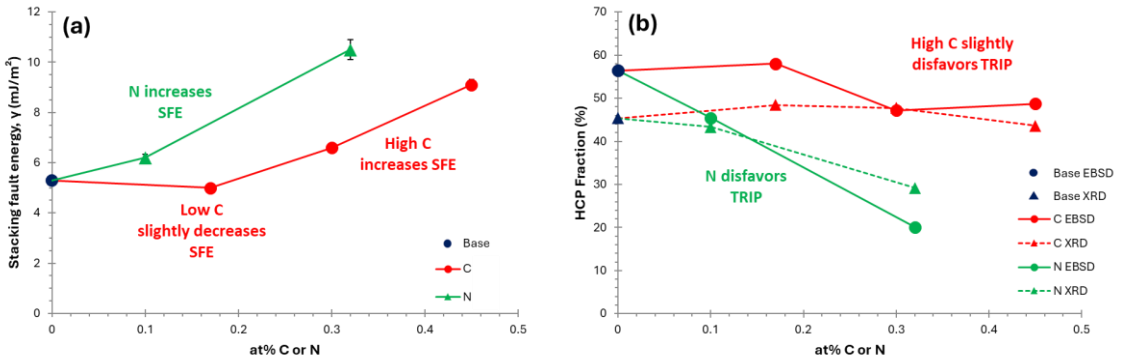

Figure 4.16: (a) Effect of C and N on stacking fault energy (when uncertainty bars are not visible, they are smaller than the corresponding icon), and (b) strain-induced HCP fraction (TRIP effect) revealing an inversely proportional relationship between SFE and transformed phase fraction.

The results showed that the N addition increases the SFE in the $Cr_{40}Co_{40}Ni_{20}$ alloy, while the C addition only increases the SFE for higher C levels. It is observed that N is more effective in increasing SFE compared to C, which agrees with Moravcik et al. (2022) [125] in the CrCoNi alloy. Although the literature presents controversial results regarding the influence of interstitials on SFE [12,20], at least two studies with C observed a trend similar to that seen in this study. Bae et al. (2022) [126] and Petrov (2005) [127] observed in steels that low C levels decrease SFE and higher C levels increase SFE, similar to that seen in Figure 4.16(a).

It is known that the SFE controls the deformation mechanisms [28,35,36], and the strain-induced phase transformation (TRIP effect) is typically activated for very low SFEs (<15 mJ/m²) [35]. In this work, the alloys presented SFE between 5 and 10.5 mJ/m², in the range where the TRIP effect is expected, and as shown in Section 4.4.1

(Strain-induced martensite formation in cold-rolled samples), all alloys indeed present the TRIP effect, although to different extents.

Lastly, increasing the SFE should disfavor the TRIP effect and induce a lower fraction of transformed phase. This behavior was observed in this work, comparing Figures 4.16(a) and 4.16(b), an inversely proportional relationship is observed between the SFE and the strain-induced HCP fraction (TRIP effect). The N addition increases the SFE and disfavors the TRIP effect (green lines), while higher C contents increase the SFE and slightly disfavors TRIP (red lines).

4.5.2 Strain-induced HCP phase dissolution via recrystallization

In the *in situ* dilatometry/heating tests of Section 4.4.2, the FCC matrix was initially cold-deformed, that is, it had high stored energy due to the high density of dislocations (see Figure 4.10). This dislocation elastic energy is the thermodynamic driver for the recrystallization process [138]. Furthermore, being a low SFE FCC alloy, it also presented a martensitic HCP fraction due to the TRIP effect.

Upon heating, atomic diffusion becomes significant and dislocations tend to gain mobility. In this scenario, recovery (pre-recrystallization) tends to occur, the dislocations reorganize themselves through cross-slip and other interactions in a subgrain structure.

Next, if the material has sufficient driving force, recrystallization occurs. Nuclei arise in regions of higher stored energy (such as old grain boundaries, regions with high dislocation density, shear bands, HCP/FCC interfaces, stacking faults, etc.), which give rise to new deformation-free grains. These new grains are approximately equiaxed, have low dislocation density, and possess crystallographic orientations unrelated to the original grain. After nucleation, the new grains grow by consuming the deformed microstructure through grain boundary migration. The driving force is the energy difference between deformed and undeformed regions. Growth continues until all the deformed structure is replaced or the stored energy becomes insufficient to drive the process [138].

If heating continues after complete recrystallization, the grain growth process occurs. Recrystallized grains grow at the expense of smaller grains, as the reduction in the total area of grain boundaries is energetically favorable.

In low SFE FCC alloys, 1/2<110>{111} perfect dislocations are dissociated into pairs of 1/6<112>{111} Shockley partial dislocations, which need to recombine for cross-slip and recovery to occur. In alloys with very low SFE, as is the case with the alloy in this work ($Cr_{40}Co_{40}Ni_{20}$) [7], the separation between the partials is significantly greater, making their recombination and the cross-slip mechanism energetically unfavorable. Therefore, recovery is almost or completely suppressed in alloys with very low SFE. The dislocations cannot efficiently reorganize before recrystallization, and the internal stresses remain high. During heating, the stored energy is not gradually released, the system reaches a critical condition, and recrystallization occurs discontinuously and abruptly, which was observed in the present work. In Figure 4.10, it is possible to see a slight decrease in dislocation density above ~ 600 °C followed by a sharp decrease at ~700 °C, indicating a weak recovery process followed by an abrupt recrystallization process. In Figure 4.11, the CV value decreases sharply from ~700 °C, another indication of an abrupt recrystallization process.

In this work, the $Cr_{40}Co_{40}Ni_{20}$ alloy presents a strain-induced phase transformation (TRIP effect), where the FCC matrix phase partially transforms into an HCP phase when the alloy is deformed. The formation of the martensitic HCP phase (TRIP) during deformation, as well as mechanical twins (TWIP), can be understood as the propagation of a stacking fault along close-packed planes. In more detail: in FCC metals with low SFE, a 1/2<110>{111} perfect dislocation dissociates into a pair of 1/6<112>{111} Shockley partial dislocations, the first partial dislocation alters the crystal stacking and the second repairs it, creating a stacking fault in the region between the partials [50]. From the FCC structure (...ABC ABC... stacking): the passage of a set of partial dislocations in consecutive {111} close-packed planes generates a twin (...A/B/C/B/A... stacking); while the passage of partials every 2 {111} planes generates martensitic HCP phase (...AB/AB/AB... stacking) [29,31,47,51,52].

Basically, it is well known in literature that the formation of martensitic strain-induced HCP phase occurs in FCC alloys through the ordered passage of Shockley

partial dislocations, and not by diffusion. It is a displacive martensitic transformation, crystallographically well defined and reversible by different mechanisms [29,31].

Upon heating a previously deformed TRIP alloy (with a deformed FCC matrix + strain-induced HCP), the FCC phase becomes thermodynamically more stable above a certain temperature, and the martensitic HCP phase is expected to be transformed back into an FCC phase. This transformation (martensitic reversion) can occur through different mechanisms that depends on the chemical composition, the annealing temperature, and/or the heating rate [29]. The possible mechanisms are: i) diffusionless transformation by movement of partial dislocations; ii) diffusional transformation; or iii) recrystallization of the FCC matrix, consuming the strain-induced HCP phase.

In the case of diffusionless transformation, partial dislocations move in a way that undoes the transformation, so that the HCP reverts to FCC [29,31]. This transformation occurs below the recrystallization temperature, maintains crystallographic continuity [31,156], preserves texture, and does not completely eliminate dislocation density, that is, the resulting FCC laths will still be highly deformed [29,31,157]. In this work, the results indicate that there was no martensitic reversion by diffusionless transformation, since the HCP fraction remains constant and does not decrease until recrystallization onset at ~700 °C, as observed in Figure 4.12.

In the case of a HCP to FCC diffusional transformation below the recrystallization temperature, a decrease in the HCP fraction before recrystallization is expected, and the original FCC regions (which were not transformed) are expected to remain deformed, but this was not observed.

Finally, in the case of HCP phase dissolution via FCC matrix recrystallization, the HCP fraction should decrease in the same temperature range as the FCC matrix recrystallization. This behavior was observed in Figure 4.12, for all three alloys, the HCP fraction remains constant up to ~700 °C and then decreases to zero, similarly, the CV remains constant up to ~700 °C and decreases sharply to a lower level, indicating FCC matrix recrystallization. Furthermore, the FCC dislocation density (Figure 4.10) also decreases abruptly at ~700 °C for all alloys, indicating the onset of FCC recrystallization. Both HCP dissolution and FCC recrystallization processes occur in the same temperature range of ~700 to 800 °C. Therefore, it is possible to conclude that, for the low SFE alloys in this work, the martensitic HCP phase is transformed back into the

FCC phase by recrystallization. The HCP dissolution occurs due to the formation of new deformation-free FCC grains during recrystallization. These new FCC grains preferentially form in regions of higher stored energy (such as HCP/FCC interfaces, etc.) and consume the HCP regions in the same way that they consume the deformed FCC regions through grain boundary migration.

Martensitic reversion occurring by recrystallization indicates that the recrystallization temperature was lower than the temperature at which an HCP to FCC transformation would occur, whether diffusional or not. Coury et al. (2019) [24] estimated the T_0 temperature for CrCoNi alloys. T_0 is the temperature at which the Gibbs free energy of the FCC and HCP phases are equal (at T_0: $\Delta G^{FCC} = \Delta G^{HCP}$), HCP is more stable below T_0, and FCC is more stable above T_0. According to Coury et al. (2019) [24], the T_0 temperature for the Base alloy of this work ($Cr_{40}Co_{40}Ni_{20}$) is ~400 °C, but this does not mean that the HCP to FCC transformation occurs immediately above T_0, as there are other factors involved. Dislocations must have mobility for a displacive (diffusionless) martensitic transformation to occur, and diffusion must be appreciable for a diffusional transformation to occur. In the case of continuous heating in this chapter, it was observed that the FCC recrystallization occurred before the mobility of dislocations and atoms (by diffusion) was appreciable enough to lead to the HCP to FCC transformation.

Regarding the effect of C and N interstitial doping, in both the undoped and doped alloys, the onset of HCP dissolution occurs due to FCC recrystallization at approximately the same temperature (~700 °C). It was estimated in this work that the SFE of the C- and N-doped alloys is higher than that of the Base alloy, and the temperature T_0 is inversely proportional to the SFE, such that the doped alloys should have a lower T_0 than the Base alloy (lower than ~400 °C). However, even with the higher SFE and lower T_0 of the doped alloys, it was not sufficient for the HCP to FCC transformation to occur before recrystallization. In all the alloys studied here, the SFE is low enough that partial dislocations are quite resistant to gaining mobility before the recrystallization temperature.

Although the onset of HCP dissolution seems to occur at approximately the same temperature (~700 °C) for all alloys, Figure 4.9 indicates that the transformation inversion point and end occur at a higher temperature for the doped alloys, ~20 °C

above the Base alloy. Since HCP dissolution occurs through FCC recrystallization, in these alloys, this difference in final temperature most likely occurs because N- and C-doping slightly delays the end of recrystallization by ~40 °C, as seen in Figure 4.10, where the doped alloys reach a plateau of lower dislocation density at a higher temperature than the Base alloy. The literature suggests that interstitial doping can lead to a higher energy barrier for recrystallization and grain growth during annealing and delaying their kinetics [16,108,121,138], it occurs through the interaction of solute atmospheres and precipitates with grain boundaries, which limits the migration of these boundaries.

4.6 Conclusions

From the $Cr_{40}Co_{40}Ni_{20}$ MPEA (Base alloy), different N- and C-doped alloys were designed, produced, and thermomechanically processed. The analysis of deformed samples allow us to evaluate the influence of the C and N addition on the FCC to HCP strain-induced transformation (TRIP effect). *In situ* SXRD analyses during heating allow the study of the reversion of HCP martensite formed during deformation. SXRD analyses during heating also contribute to the study of recrystallization and grain growth. The following conclusions were drawn:

1) After deformation, all alloys exhibited HCP strain-induced transformation (TRIP effect) to different extents. Compared to the Base alloy, N addition decreased the strain-induced HCP fraction, hindering the TRIP effect, while the C addition did not show monotonic behavior, but for higher C contents a decrease in the strain-induced HCP fraction was also observed, also hindering the TRIP effect. The decrease in the extent of TRIP effect in the doped samples can be justified by the increase in SFE, with N-doping being more effective in increasing SFE than C-doping.

2) At room temperature (23 °C), all deformed alloys presented a highly deformed FCC matrix + strain-induced HCP structure. During continuous heating, the martensitic HCP phase maintained a constant fraction up to ~700 °C and only

then began to dissolve. It was estimated that the HCP phase was completely dissolved between 810~830 °C. A small fraction of the sigma phase formed and was dissolved (between 800~1000°C) for Base and C-doped alloys, N-doped alloy had no sigma. At higher temperature (above ~1000°C), all alloys had a single-phase FCC structure.

3) Initially, the previously deformed alloys presented a high dislocation density plateau. Between 600~700 °C, a slight decrease in dislocation density indicated a possible weak recovery process, then a sharp decrease at ~700 °C indicated the recrystallization process of the FCC matrix. Finally, all alloys reached a plateau of lower dislocation density above 760~800 °C.

4) This work used a methodology that made it possible to find the temperature at which recrystallization and diffraction-detectable grain growth occurred by evaluating the characteristics and texture of FCC Debye-Scherrer rings along the azimuthal angle and quantifying it using the coefficient of variation (CV). For all alloys, recrystallization began at ~700 °C when the textured FCC rings became homogeneous along the azimuthal angle and the CV dropped abruptly, and it ended between 800~850 °C when CV reached a plateau again. Furthermore, the onset of grain growth was assessed when the FCC rings became a set of resolvable spots and the CV increased again at higher temperatures. The results indicated that doping with C and especially N delayed the onset of the grain growth process.

5) For low SFE alloys of this work, the martensitic HCP phase was transformed back into the FCC phase upon heating (martensitic reversion) due to the formation of new deformation-free FCC grains during recrystallization, and not by a displacive or diffusional transformation before recrystallization. These new FCC grains consume the HCP regions in the same way that they consume the deformed FCC regions through grain boundary migration.

6) N- and C-doping had no significant effect on the onset of recrystallization, but it slightly delayed the end of recrystallization (by ~40 °C). Consistently, it was also observed that C- and N-doping had no significant effect on the onset of HCP dissolution and delayed the transformation inversion point and end (by ~20 °C), since HCP dissolution occurs through FCC recrystallization in these alloys.

CHAPTER 5 – General discussion and conclusions

5.1 General discussion

5.1.1 Central question of this thesis

This thesis was motivated by a central question: how grain refinement and interstitial alloying (C and N) interact with each other and with the TRIP effect in the $Cr_{40}Co_{40}Ni_{20}$ MPEA, and how these interactions can be exploited to design alloys with a desired combination of properties?

This problem arises from the fact that the $Cr_{40}Co_{40}Ni_{20}$ alloy combines two relevant mechanisms: (i) a strong grain refinement strengthening component, described by high Hall–Petch coefficients, and (ii) a strain-induced phase transformation (FCC to HCP), i.e. the TRIP effect, which provides high work hardening and ductility [7]. In addition, the use of interstitial elements can improve the grain refinement capacity of this alloy, but it can also modify the phase equilibria and the acting deformation mechanisms. These features are individually beneficial, but their interaction is not trivial and sometimes contradictory in the literature [11,12,20], reinforcing the importance of studies on these topics and their interactions.

To address this problem, this work was structured into three main chapters. Chapter 2 evaluated the influence of grain size on the activation and evolution of the TRIP effect. Chapter 3 investigated the effects of C and N on the phase equilibria and microstructure refinement in the $Cr_{40}Co_{40}Ni_{20}$ alloy. Chapter 4 evaluated how C and N addition affects the strain-induced martensite formation and the martensite reversion during heating. Together, these three chapters provide a consistent answer to the question introduced in Chapter 1.

5.1.2 Grain refinement and TRIP

A key outcome from Chapter 2 is that grain refinement did not suppress and did not alter the early onset of the TRIP effect in the $Cr_{40}Co_{40}Ni_{20}$ alloy, within the microstructural range studied in this work. In other words, it is possible to significantly increase yield strength through grain refinement, while maintaining a strain-induced

phase transformation that activates close to the yield point and contributes to a sustained work hardening capacity. This result is particularly relevant for the $Cr_{40}Co_{40}Ni_{20}$ alloy, which shows a high grain size sensitivity with respect to mechanical strength and therefore benefits considerably from refined grains [7]. In fact, grain refinement produced a significant strengthening response with yield stress increasing by ~100% (417 to 834 MPa) for the smallest grain size sample.

Chapter 2 also demonstrated that the critical stress required to activate and progress the FCC to HCP transformation follows the Hall-Petch relation, similarly to the yield stress, and the Hall-Petch slopes for both yield stress and TRIP effect were found to be approximately equal ($k_y \approx k_{TRIP}$). In other words, the critical stress for TRIP is proportional to the grain refinement strengthening. These results provide a direct answer to a central concern in TRIP alloys: while some studies report that grain refinement may suppress TRIP/TWIP due to changes in the effective SFE, the present work shows that for a sufficiently low SFE alloy, TRIP activation is governed by the onset of dislocation slip, which occurs near yielding for all grain sizes. Therefore, in terms of strain, grain size has no obvious influence on the TRIP effect, since the transformation is triggered once plasticity initiates, and refined-grain samples simply reach this condition at higher stresses due to Hall-Petch strengthening.

Chapter 2 revealed that the TRIP effect is activated at the yield point, and its evolution is controlled by the deformation level, independent of grain size. This information made it possible to develop a strategy to further study the influence of C and N on the TRIP effect in isolation in Chapter 4 (effect of C/N on TRIP), since the addition of these interstitial elements modifies the grain size, as seen in Chapter 3 (effect of C/N on grain size). Therefore, in Chapter 4, precautions were taken to ensure that all samples had the same deformation level through controlled cold rolling processing.

Therefore, the first part of the central problem is answered as follows: in the $Cr_{40}Co_{40}Ni_{20}$ MPEA, grain refinement can be used as a strengthening strategy without compromising TRIP, which supports the idea that grain refinement and TRIP can efficiently operate together to improve or tune mechanical properties. Furthermore, a Hall-Petch-based model and a mechanism were proposed in Chapter 2 to describe the influence of FCC grain size on the onset and evolution of the TRIP effect.

5.1.3 Interstitial doping, grain refinement and phase equilibria

Chapter 3 evaluated the use of interstitial alloying (C and N) as a microstructural refinement route in the $Cr_{40}Co_{40}Ni_{20}$ alloy. The results showed that homogenization at 1200 °C (2 h) results in a fully single-phase FCC structure in all compositions, while cold deformation triggers the FCC to HCP strain-induced transformation (TRIP), and subsequent recrystallization heat treatments (>750 °C, 1 h) dissolve the HCP martensite.

A main conclusion from Chapter 3 is that both N and C additions promote microstructural refinement by different and sometimes overlapping mechanisms. In precipitate-free conditions, grain refinement is associated with slower grain growth kinetics, characterized by a reduction in the grain growth exponent (n) in doped alloys. This is consistent with the idea that interstitial solutes may reduce grain boundary mobility, which is often linked to a drag-type effect. This topic has been identified as an important research direction in the context of MPEAs [11,12]. In conditions where precipitation occurs, refinement can be further enhanced through the Zener pinning mechanism, due to the presence of second phases that limit grain boundary motion [11,12,117].

However, this thesis also showed that interstitial alloying is not a purely microstructural refinement tool, because C and N also influence the phase equilibria. The results showed that C and N increase the stability of the FCC phase against sigma phase precipitation, reducing or suppressing sigma phase formation under certain heat treatment conditions. This is relevant because sigma phase is generally undesirable due to its brittle character [45], and its suppression broadens the processing window for these alloys.

At the same time, precipitation behavior differed between the interstitial elements. No nitride precipitation was observed in the N-doped alloys under the investigated conditions, even with 0.32 at% N added. In contrast, $M_{23}C_6$ carbide precipitation occurred under various conditions in C-doped alloys, consistent with a higher tendency for carbide formation in FCC matrices.

Therefore, the second part of the central problem is answered as follows: C and N are effective microstructural refiners in the $Cr_{40}Co_{40}Ni_{20}$ alloy, retarding grain growth even without precipitates. Under conditions where precipitation occurs, the pinning mechanism also acts in grain refinement, providing highly refined structures. In parallel,

C and N modify phase stability and precipitation behavior, which must be considered in alloy and process design.

5.1.4 Interstitial doping, martensite formation (TRIP) and reversion, recrystallization and grain growth

The results from Chapter 4 show that, although interstitial doping enables microstructural refinement, it also modifies the strain-induced phase transformation response.

A major outcome is that N additions consistently disfavor the TRIP effect. For C, the behavior was non-monotonic, but higher C levels also disfavored TRIP. This indicates that interstitials do not only modify grain growth kinetics and phase equilibria, but they also influence the stability of the FCC phase during deformation and therefore the FCC to HCP transformation tendency. This trend is consistent with the idea that small composition changes can alter the energetic balance that governs deformation mechanisms in low SFE FCC alloys. In multiple alloy families, including steels and MPEAs, changes in SFE strongly influence whether deformation proceeds by dislocation slip, twinning, or martensitic transformation [20,35,53]. From an alloy design standpoint, this means that interstitial additions should be treated as a high-impact variable, even at small concentrations.

An additional mechanistic result from Chapter 4 is related to martensite reversion during heating. For the investigated conditions, the strain-induced HCP phase transformed back to FCC during annealing by recrystallization of the FCC matrix, rather than by a direct displacive or diffusional HCP to FCC transformation prior to recrystallization. This observation is relevant because it indicates that microstructural restoration during annealing is dominated by nucleation and growth of recrystallized FCC grains that consume the deformed microstructure and the HCP lamellae.

A key methodological contribution of Chapter 4 was the use of synchrotron diffraction ring texture quantification via coefficient of variation (CV) to identify recrystallization and diffraction-detectable grain growth temperatures. The results from this method showed good correlation with the dislocation density obtained via peak broadening in SXRD, reinforcing its effectiveness. One of the advantages of the ring

texture quantification method via CV is the ability to evaluate not only recrystallization, but also grain growth, which the dislocation density alone cannot assess. One of the caveats regarding ring texture quantification via CV is the need to evaluate several hkl rings or select the most suitable ones. In this study, the CV results regarding recrystallization temperature showed small differences between 111 and 200 FCC rings, making it impossible to reliably conclude about the effect that C and N cause on the recrystallization temperature range solely through CV. On the other hand, both 111 and 200 ring results agreed that C and N delays diffraction-detectable grain growth onset. There are precedents in the literature for interstitials retarding grain growth in Cantor alloy [11,144].

C- and N-doping does not significantly change the onset of recrystallization, but dislocation density quantification indicates that it slightly delays the end of recrystallization. Consistently, it also delays the HCP dissolution inversion point and end, reflecting the strong coupling between martensite reversion and FCC recrystallization in these alloys. Furthermore, grain growth onset occurs later and is systematically delayed by interstitial additions.

The results showing that C and N delay recrystallization and grain growth in Chapter 4 are consistent with the smaller grain size observed in the doped samples in Chapter 3. In Chapter 3, it was observed that N and C had the capacity to refine the microstructure even without pinning by precipitates, which was explained by the lower grain growth kinetics of the doped alloys. The results from Chapter 4 reinforce this explanation: grain growth onset is delayed in doped samples, therefore the grain growth time is shorter, which in itself could explain the smaller grain size after a given time. Added to this is the lower grain growth kinetics of the doped alloys, which causes the grains to grow more slowly, generating more refined structures.

Therefore, the third part of the central problem is answered as follows: C and N allow grain refinement in $Cr_{40}Co_{40}Ni_{20}$, but they can also reduce the TRIP contribution depending on content, meaning that processing routes and interstitial levels must be optimized to balance microstructural refinement and deformation behavior.

5.1.5 Overall answer to the problem stated in this thesis

Combining the findings of Chapters 2-4, the thesis provides a consistent answer to the problem proposed in Chapter 1: how do grain size, TRIP, and interstitial doping interact in the low SFE CrCoNi alloy? The answer can be summarized in the following statements:

1. Grain refinement increases mechanical strength substantially in $Cr_{40}Co_{40}Ni_{20}$, and the TRIP effect remains readily activated once plasticity begins. This is because TRIP is controlled by the strain level and scales with Hall-Petch strengthening, rather than being suppressed by reduced grain size.
2. C and N additions enable further microstructural refinement by retarding the onset and kinetics of grain growth and, depending on conditions, also by precipitation pinning. They also stabilize FCC against sigma precipitation, expanding processing windows.
3. Interstitial doping has strong influence on strain-induced martensitic formation (TRIP), especially for N and for higher C levels. Upon heating, martensite reversion is governed by FCC recrystallization in this low SFE alloy, meaning that HCP dissolution temperature is strongly linked to the recrystallization window rather than the thermodynamic T_0 alone.

Altogether, the thesis shows that grain refinement and TRIP are synergic strengthening/ductilizing mechanisms in $Cr_{40}Co_{40}Ni_{20}$, and that interstitial alloying offers additional control over grain size and phase stability, while introducing a tunable effect on TRIP extent.

5.2 Main contributions of this thesis

Among the main contributions of this thesis, the following scientific, methodological, and technological contributions can be drawn.

5.2.1 Scientific contributions

This thesis establishes a Hall-Petch-type framework for TRIP activation, showing that the stress required to trigger and progress the FCC to HCP transformation scales proportionally with the grain refinement strengthening and presents a grain-size dependence comparable to yielding ($k_y \approx k_{TRIP}$).

The results support a mechanistic interpretation in which TRIP activation is coupled to the onset of dislocation slip (yielding), rather than requiring grain-size-driven changes in the effective SFE as the main explanation for reduced transformation activity in refined microstructures.

5.2.2 Methodological contributions

An X-ray diffraction approach was developed and applied to identify recrystallization and diffraction-detectable grain growth during continuous heating using texture homogeneity metrics based on the coefficient of variation (CV) of Debye–Scherrer rings, enabling quantitative determination of microstructural transition temperatures from diffraction data.

5.2.3 Technological contributions

The low SFE $Cr_{40}Co_{40}Ni_{20}$ alloy was shown to be substantially strengthened by grain refinement (~100% yield stress increase) while preserving TRIP-assisted work hardening and ductility benefits.

Interstitial alloying with C and N was demonstrated as an effective strategy to delay grain growth and stabilize the FCC phase (including suppression of sigma formation), providing a wider processing window and additional flexibility to tailor microstructure for strength-ductility optimization.

5.3 General conclusions

Based on the results and analyses presented in Chapters 2, 3, and 4, as well as the discussion presented in Chapter 5, the following general conclusions can be drawn:

1. The $Cr_{40}Co_{40}Ni_{20}$ MPEA exhibits strong potential for strength improvement through grain refinement, due to its high grain-size sensitivity described by Hall-Petch behavior.
2. The critical stress for TRIP is proportional to the grain refinement strengthening, while grain size has no obvious influence on TRIP effect in terms of strain, since transformation onset occurs close to the yield point and is controlled by dislocation slip activation in the investigated grain size range.
3. C and N additions promote microstructural refinement in the $Cr_{40}Co_{40}Ni_{20}$ alloy, by reducing grain growth kinetics in precipitate-free conditions, and by Zener pinning when precipitation occurs.
4. C and N increase FCC stability against sigma phase precipitation, reducing or suppressing sigma phase formation under certain heat treatment conditions.
5. Nitride precipitation was not observed in the N-doped alloys under the investigated conditions, even with 0.32 at% N. $M_{23}C_6$ carbide precipitation occurred under various conditions in C-doped alloys, indicating a stronger tendency for carbide formation in the FCC matrix.
6. N additions disfavor the TRIP effect, while C additions show a non-monotonic effect, but higher C levels also disfavor TRIP. The decrease in the extent of TRIP effect can be justified by the increase in SFE.
7. The martensitic HCP phase reverses back to FCC during annealing by recrystallization of the FCC matrix, and not by a displacive or diffusional HCP to FCC transformation prior to recrystallization.
8. Overall, this thesis demonstrates that the $Cr_{40}Co_{40}Ni_{20}$ alloy can be strengthened by microstructural refinement while maintaining the TRIP contribution, and that interstitial alloying is an effective refinement strategy, but its use must consider the associated changes in phase equilibria and deformation mechanisms.

SUGGESTIONS FOR FUTURE WORK

1. Extension of the Hall-Petch TRIP framework to other MPEAs and validation of the $k_y \approx k_{TRIP}$ behavior across compositions and processing routes.

2. Systematic quantification of grain refinement mechanisms with controlled interstitial content in solid solution and in second phases, in order to separate the contributions of different effects: solute drag, pinning, sluggish diffusion, etc.

3. Expanded precipitation engineering in C-doped alloys to maximize pinning mechanism through optimized $M_{23}C_6$ size fraction/distribution.

4. Coupled mechanical testing + in situ diffraction for doped/refined conditions to map the TRIP fraction evolution under different strain paths and strain rates.

5. Direct experimental measurement of SFE as a function of interstitial content and correlation with TRIP kinetics, including possible short-range order effects.

6. Apply the CV-based texture method to additional thermomechanical routes (e.g., different cold work levels) to build predictive processing maps of recrystallization/grain growth.

BIBLIOGRAPHIC REFERENCES

[1] W. Zhang, P.K. Liaw, Y. Zhang, Science and technology in high-entropy alloys, Science China Materials. 61 (2018) 2–22. https://doi.org/10.1007/s40843-017-9195-8.

[2] D.B. Miracle, O.N. Senkov, A critical review of high entropy alloys and related concepts, Acta Materialia. 122 (2017) 448–511. https://doi.org/10.1016/j.actamat.2016.08.081.

[3] E.P. George, D. Raabe, R.O. Ritchie, High-entropy alloys, Nature Reviews Materials. 4 (2019) 515–534. https://doi.org/10.1038/s41578-019-0121-4.

[4] M.C. Gao, P.K. Liaw, J.W. Yeh, Y. Zhang, High-entropy alloys: Fundamentals and applications, 1st ed., Springer, 2016. https://doi.org/10.1007/978-3-319-27013-5.

[5] B. Gludovatz, A. Hohenwarter, K.V.S. Thurston, H. Bei, Z. Wu, E.P. George, R.O. Ritchie, Exceptional damage-tolerance of a medium-entropy alloy CrCoNi at cryogenic temperatures, Nature Communications. 7 (2016) 1–8. https://doi.org/10.1038/ncomms10602.

[6] F.G. Coury, K.D. Clarke, C.S. Kiminami, M.J. Kaufman, A.J. Clarke, High Throughput Discovery and Design of Strong Multicomponent Metallic Solid Solutions, Scientific Reports. 8 (2018) 1–10. https://doi.org/10.1038/s41598-018-26830-6.

[7] G. Bertoli, L.B. Otani, A.J. Clarke, C.S. Kiminami, F.G. Coury, Hall-Petch and grain growth kinetics of the low stacking fault energy TRIP Cr40Co40Ni20 multi-principal element alloy, Applied Physics Letters. 119 (2021) 061903. https://doi.org/10.1063/5.0057888.

[8] W. Chen, X. An, Z. Wang, Y. Li, J. Gu, M. Song, Grain size dependent deformation behavior of a metastable Fe40Co20Cr20Mn10Ni10 high-entropy alloy, Journal of Alloys and Compounds. 883 (2021) 1–7. https://doi.org/10.1016/j.jallcom.2021.160876.

[9] M. Naghizadeh, H. Mirzadeh, Effects of Grain Size on Mechanical Properties and Work-Hardening Behavior of AISI 304 Austenitic Stainless Steel, Steel

Research International. 90 (2019) 1–9. https://doi.org/10.1002/srin.201900153.

[10] S. Sevsek, F. Brasche, D.A. Molodov, W. Bleck, On the influence of grain size on the TWIP/TRIP-effect and texture development in high-manganese steels, Materials Science and Engineering: A. 754 (2019) 152–160. https://doi.org/10.1016/j.msea.2019.03.072.

[11] M.R. Zamani, H. Mirzadeh, M. Malekan, S.C. Cao, J.W. Yeh, Grain Growth in High-Entropy Alloys (HEAs): A Review, High Entropy Alloys & Materials 2022 1:1. 1 (2023) 25–59. https://doi.org/10.1007/S44210-022-00002-8.

[12] M.Y. He, Y.F. Shen, N. Jia, P.K. Liaw, C and N doping in high-entropy alloys: A pathway to achieve desired strength-ductility synergy, Applied Materials Today. 25 (2021). https://doi.org/10.1016/j.apmt.2021.101162.

[13] I. Moravcik, H. Hadraba, L. Li, I. Dlouhy, D. Raabe, Z. Li, Yield strength increase of a CoCrNi medium entropy alloy by interstitial nitrogen doping at maintained ductility, Scripta Materialia. 178 (2020) 391–397. https://doi.org/10.1016/j.scriptamat.2019.12.007.

[14] Y.Y. Shang, Y. Wu, J.Y. He, X.Y. Zhu, S.F. Liu, H.L. Huang, K. An, Y. Chen, S.H. Jiang, H. Wang, X.J. Liu, Z.P. Lu, Solving the strength-ductility tradeoff in the medium-entropy NiCoCr alloy via interstitial strengthening of carbon, Intermetallics. 106 (2019) 77–87. https://doi.org/10.1016/j.intermet.2018.12.009.

[15] M. Traversier, P. Mestre-Rinn, N. Peillon, E. Rigal, X. Boulnat, F. Tancret, J. Dhers, A. Fraczkiewicz, Nitrogen-induced hardening in an austenitic CrFeMnNi high-entropy alloy (HEA), Materials Science and Engineering A. 804 (2021). https://doi.org/10.1016/j.msea.2020.140725.

[16] I. Moravcik, V. Hornik, P. Minárik, L. Li, I. Dlouhy, M. Janovska, D. Raabe, Z. Li, Interstitial doping enhances the strength-ductility synergy in a CoCrNi medium entropy alloy, Materials Science and Engineering A. 781 (2020) 1–14. https://doi.org/10.1016/j.msea.2020.139242.

[17] K.S. Chung, J.H. Luan, C.H. Shek, Strengthening and deformation mechanism of interstitially N and C doped FeCrCoNi high entropy alloy, Journal of Alloys and Compounds. 904 (2022) 164118. https://doi.org/10.1016/J.JALLCOM.2022.164118.

[18] K.S. Chung, P.M. Yiu, T.F. Hung, C.H. Shek, Strengthening and deformation

mechanism of a Fe20Co20Cr20Mn20Ni20 high entropy alloy with high nitrogen content, Journal of Alloys and Compounds. 871 (2021) 159587. https://doi.org/10.1016/J.JALLCOM.2021.159587.

[19] X.W. Liu, G. Laplanche, A. Kostka, S.G. Fries, J. Pfetzing-Micklich, G. Liu, E.P. George, Columnar to equiaxed transition and grain refinement of cast CrCoNi medium-entropy alloy by microalloying with titanium and carbon, Journal of Alloys and Compounds. 775 (2019) 1068–1076. https://doi.org/10.1016/J.JALLCOM.2018.10.187.

[20] J.W. Simmons, Overview: High-nitrogen alloying of stainless steels, Materials Science and Engineering: A. 207 (1996) 159–169. https://doi.org/10.1016/0921-5093(95)09991-3.

[21] G. Laplanche, A. Kostka, C. Reinhart, J. Hunfeld, G. Eggeler, E.P. George, Reasons for the superior mechanical properties of medium-entropy CrCoNi compared to high-entropy CrMnFeCoNi, Acta Materialia. 128 (2017) 292–303. https://doi.org/10.1016/j.actamat.2017.02.036.

[22] F.G. Coury, P. Wilson, K.D. Clarke, M.J. Kaufman, A.J. Clarke, High-throughput solid solution strengthening characterization in high entropy alloys, Acta Materialia. 167 (2019) 1–11. https://doi.org/10.1016/j.actamat.2019.01.029.

[23] F.G. Coury, G. Zepon, C. Bolfarini, Multi-principal element alloys from the CrCoNi family: outlook and perspectives, Journal of Materials Research and Technology. 15 (2021) 3461–3480. https://doi.org/10.1016/j.jmrt.2021.09.095.

[24] F.G. Coury, D. Santana, Y. Guo, J. Copley, L. Otani, S. Fonseca, G. Zepon, C. Kiminami, M. Kaufman, A. Clarke, Design and in-situ characterization of a strong and ductile co-rich multicomponent alloy with transformation induced plasticity, Scripta Materialia. 173 (2019) 70–74. https://doi.org/10.1016/j.scriptamat.2019.07.045.

[25] S.F. Liu, Y. Wu, H.T. Wang, J.Y. He, J.B. Liu, C.X. Chen, X.J. Liu, H. Wang, Z.P. Lu, Stacking fault energy of face-centered-cubic high entropy alloys, Intermetallics. 93 (2018) 269–273. https://doi.org/10.1016/j.intermet.2017.10.004.

[26] Z. Li, K.G. Pradeep, Y. Deng, D. Raabe, C.C. Tasan, Metastable high-entropy dual-phase alloys overcome the strength-ductility trade-off, Nature. 534 (2016)

227–230. https://doi.org/10.1038/nature17981.

[27] Z. Li, C.C. Tasan, K.G. Pradeep, D. Raabe, A TRIP-assisted dual-phase high-entropy alloy: Grain size and phase fraction effects on deformation behavior, Acta Materialia. 131 (2017) 323–335. https://doi.org/10.1016/j.actamat.2017.03.069.

[28] D. Wei, X. Li, J. Jiang, W. Heng, Y. Koizumi, W.M. Choi, B.J. Lee, H.S. Kim, H. Kato, A. Chiba, Novel Co-rich high performance twinning-induced plasticity (TWIP) and transformation-induced plasticity (TRIP) high-entropy alloys, Scripta Materialia. 165 (2019) 39–43. https://doi.org/10.1016/j.scriptamat.2019.02.018.

[29] M.J. Sohrabi, M. Naghizadeh, H. Mirzadeh, Deformation - induced martensite in austenitic stainless steels : A review, Archives of Civil and Mechanical Engineering. 1 (2020) 1–24. https://doi.org/10.1007/s43452-020-00130-1.

[30] Y. Wang, C. Huang, X. Ma, J. Zhao, F. Guo, X. Fang, Y. Zhu, Y. Wei, The optimum grain size for strength-ductility combination in metals, International Journal of Plasticity. 164 (2023) 103574. https://doi.org/10.1016/j.ijplas.2023.103574.

[31] A. Mandal, S. Morankar, M. Sen, S. Samanta, S.B. Singh, D. Chakrabarti, A Descriptive Model on the Grain Size Dependence of Deformation and Martensitic Transformation in Austenitic Stainless Steel, Metallurgical and Materials Transactions A. 51 (2020) 3886–3905. https://doi.org/10.1007/s11661-020-05861-7.

[32] Y. Lee, C. Choi, Driving Force for g → « Martensitic Transformation and SFE of austenite in Fe-Mn binary system, Metallurgical and Materials Transactions A. 31A (2000) 355–360. https://doi.org/10.1007/s11661-000-0271-3.

[33] M.J. Sohrabi, H. Mirzadeh, S. Sadeghpour, R. Mahmudi, Grain size dependent mechanical behavior and TRIP effect in a metastable austenitic stainless steel, International Journal of Plasticity. 160 (2023) 103502. https://doi.org/10.1016/j.ijplas.2022.103502.

[34] O.A. Zambrano, Stacking fault energy maps of Fe-Mn-Al-C-Si steels: Effect of temperature, grain size, and variations in compositions, Journal of Engineering Materials and Technology. 138 (2016) 1–9. https://doi.org/10.1115/1.4033632.

[35] B.C. De Cooman, Y. Estrin, S.K. Kim, Twinning-induced plasticity (TWIP) steels, Acta Materialia. 142 (2018) 283–362. https://doi.org/10.1016/j.actamat.2017.06.046.

[36] S.T. Pisarik, D.C. Van Aken, Thermodynamic Driving Force of the γ → ε Transformation and Resulting MS Temperature in High-Mn Steels, Metallurgical and Materials Transactions A: Physical Metallurgy and Materials Science. 47A (2016) 1009–1018. https://doi.org/10.1007/s11661-015-3265-x.

[37] X. Li, L. Chen, Y. Zhao, X. Yuan, R. Devesh, K. Misra, Influence of original austenite grain size on tensile properties of a high- manganese transformation-induced plasticity (TRIP) steel, Materials Science & Engineering A. 715 (2018) 257–265. https://doi.org/10.1016/j.msea.2017.12.107.

[38] W. Lu, X. Luo, Y. Yang, B. Huang, Hall-petch relationship and heterogeneous strength of CrCoNi medium-entropy alloy, Materials Chemistry and Physics. 251 (2020) 1–7. https://doi.org/10.1016/j.matchemphys.2020.123073.

[39] G.W. Hu, L.C. Zeng, H. Du, X.W. Liu, Y. Wu, P. Gong, Z.T. Fan, Q. Hu, E.P. George, Tailoring grain growth and solid solution strengthening of single-phase CrCoNi medium-entropy alloys by solute selection, Journal of Materials Science and Technology. 54 (2020) 196–205. https://doi.org/10.1016/j.jmst.2020.02.073.

[40] Z. Wu, H. Bei, G.M. Pharr, E.P. George, Temperature dependence of the mechanical properties of equiatomic solid solution alloys with face-centered cubic crystal structures, Acta Materialia. 81 (2014) 428–441. https://doi.org/10.1016/j.actamat.2014.08.026.

[41] S. Yoshida, T. Bhattacharjee, Y. Bai, N. Tsuji, Friction stress and Hall-Petch relationship in CoCrNi equi-atomic medium entropy alloy processed by severe plastic deformation and subsequent annealing, Scripta Materialia. 134 (2017) 33–36. https://doi.org/10.1016/j.scriptamat.2017.02.042.

[42] J. Miao, C.E. Slone, T.M. Smith, C. Niu, H. Bei, M. Ghazisaeidi, G.M. Pharr, M.J. Mills, The evolution of the deformation substructure in a Ni-Co-Cr equiatomic solid solution alloy, Acta Materialia. 132 (2017) 35–48. https://doi.org/10.1016/j.actamat.2017.04.033.

[43] F.C. Puosso, G. Bertoli, F.G. Coury, A Hall–Petch study of the high toughness Cr40Co30Ni30 multi-principal element alloy, Journal of Materials Research. 38

(2022) 215–227. https://doi.org/10.1557/s43578-022-00729-5.

[44] K. Feng, Y. Zhang, Z. Li, C. Yao, L. Yao, C. Fan, Corrosion properties of laser cladded CrCoNi medium entropy alloy coating, Surface and Coatings Technology. 397 (2020) 126004. https://doi.org/10.1016/j.surfcoat.2020.126004.

[45] R.W. Cahn, P. Haasen, Physical Metallurgy, 4th ed., Elsevier Science B. V., The Netherlands, Amsterdam, 1996.

[46] G. Laplanche, U.F. Volkert, G. Eggeler, E.P. George, Oxidation Behavior of the CrMnFeCoNi High-Entropy Alloy, Oxidation of Metals. 85 (2016) 629–645. https://doi.org/10.1007/s11085-016-9616-1.

[47] C. Niu, C.R. LaRosa, J. Miao, M.J. Mills, M. Ghazisaeidi, Magnetically-driven phase transformation strengthening in high entropy alloys, Nature Communications. 9 (2018) 1–9. https://doi.org/10.1038/s41467-018-03846-0.

[48] C.E. Slone, S. Chakraborty, J. Miao, E.P. George, M.J. Mills, S.R. Niezgoda, Influence of deformation induced nanoscale twinning and FCC-HCP transformation on hardening and texture development in medium-entropy CrCoNi alloy, Acta Materialia. 158 (2018) 38–52. https://doi.org/10.1016/j.actamat.2018.07.028.

[49] Z. Yang, S. Lu, Y. Tian, Z. Gu, H. Mao, J. Sun, L. Vitos, Assessing the magnetic order dependent y-surface of Cr-Co-Ni alloys, Journal of Materials Science & Technology. (2020). https://doi.org/10.1016/j.jmst.2020.10.078.

[50] D. Hull, D.J. Bacon, Introduction to Dislocations, 4th ed., Butterworth-Heineman, 2001.

[51] G.B. Olson, M. Cohen, A general mechanism of martensitic nucleation: Part I. General concepts and the FCC → HCP transformation, Metallurgical Transactions A. 7A (1976) 1897–1904. https://doi.org/10.1007/BF02659822.

[52] D. Wei, X. Li, S. Schönecker, J. Jiang, W.M. Choi, B.J. Lee, H.S. Kim, A. Chiba, H. Kato, Development of strong and ductile metastable face-centered cubic single-phase high-entropy alloys, Acta Materialia. 181 (2019) 318–330. https://doi.org/10.1016/j.actamat.2019.09.050.

[53] D. Wei, X. Li, W. Heng, Y. Koizumi, F. He, W.M. Choi, B.J. Lee, H.S. Kim, H. Kato, A. Chiba, Novel Co-rich high entropy alloys with superior tensile properties, Materials Research Letters. 7 (2019) 82–88.

https://doi.org/10.1080/21663831.2018.1553803.

[54] M. Bahramyan, R.T. Mousavian, D. Brabazon, Study of the plastic deformation mechanism of TRIP-TWIP high entropy alloys at the atomic level, International Journal of Plasticity. 127 (2020) 102649. https://doi.org/10.1016/j.ijplas.2019.102649.

[55] K. Kishore, A.K. Chandan, P.T. Hung, S. Kumar, M. Ranjan, M. Kawasaki, J. Gubicza, Effect of Si on the evolution of plasticity mechanisms, grain refinement and hardness during high-pressure torsion of a non-equiatomic CoCrMnNi multi-principal element alloy, International Journal of Plasticity. 169 (2023). https://doi.org/10.1016/j.ijplas.2023.103720.

[56] D. Wei, W. Gong, T. Tsuru, I. Lobzenko, X. Li, S. Harjo, T. Kawasaki, H.S. Do, J.W. Bae, C. Wagner, G. Laplanche, Y. Koizumi, H. Adachi, K. Aoyagi, A. Chiba, B.J. Lee, H.S. Kim, H. Kato, Si-addition contributes to overcoming the strength-ductility trade-off in high-entropy alloys, International Journal of Plasticity. 159 (2022) 103443. https://doi.org/10.1016/j.ijplas.2022.103443.

[57] P. Singh, W. Trehern, B. Vela, P. Sharma, T. Kirk, Z. Pei, R. Arroyave, M.C. Gao, D.D. Johnson, Understanding the effect of refractory metal chemistry on the stacking fault energy and mechanical property of Cantor-based multi-principal element alloys, International Journal of Plasticity. (2024) 104020. https://doi.org/10.1016/j.ijplas.2024.104020.

[58] A.K. Chandan, K. Kishore, P.T. Hung, M. Ghosh, S.G. Chowdhury, M. Kawasaki, J. Gubicza, Effect of nickel addition on enhancing nano-structuring and suppressing TRIP effect in Fe40Mn40Co10Cr10 high entropy alloy during high-pressure torsion, International Journal of Plasticity. 150 (2022). https://doi.org/10.1016/j.ijplas.2021.103193.

[59] Y.H. Zhang, Y. Zhuang, A. Hu, J.J. Kai, C.T. Liu, The origin of negative stacking fault energies and nano-twin formation in face-centered cubic high entropy alloys, Scripta Materialia. 130 (2017) 96–99. https://doi.org/10.1016/j.scriptamat.2016.11.014.

[60] J. Ding, Q. Yu, M. Asta, R.O. Ritchie, Tunable stacking fault energies by tailoring local chemical order in CrCoNi medium-entropy alloys, Proceedings of the National Academy of Sciences of the United States of America. 115 (2018)

8919–8924. https://doi.org/10.1073/pnas.1808660115.

[61] Y. Ikeda, F. Körmann, I. Tanaka, J. Neugebauer, Impact of chemical fluctuations on stacking fault energies of CrCoNi and CrMnFeCoNi high entropy alloys from first principles, Entropy. 20 (2018) 1–20. https://doi.org/10.3390/e20090655.

[62] S. Zhao, G.M. Stocks, Y. Zhang, Stacking fault energies of face-centered cubic concentrated solid solution alloys, Acta Materialia. 134 (2017) 334–345. https://doi.org/10.1016/j.actamat.2017.05.001.

[63] J.A. Copley, F.G. Coury, B. Ellyson, J. Klemm-Toole, N. Kedir, C. Kirk, W. Chen, N. Parab, T. Sun, K. Fezzaa, K.D. Clarke, A.J. Clarke, In-situ observation of FCC□HCP transformation-induced plasticity behavior during dynamic deformation of CoCrNi multi-principal element alloys, Metallurgical and Materials Transactions A. (2020) in preparation.

[64] L. Zhu, Z. Wu, Effects of Short Range Ordering on the Generalized Stacking Fault Energy and Deformation Mechanisms in FCC Multiprincipal Element Alloys, 259 (2023). https://ssrn.com/abstract=4479313.

[65] R. Zhang, S. Zhao, J. Ding, Y. Chong, T. Jia, C. Ophus, M. Asta, R.O. Ritchie, A.M. Minor, Short-range order and its impact on the CrCoNi medium-entropy alloy, Nature. 581 (2020) 283–287. https://doi.org/10.1038/s41586-020-2275-z.

[66] Y.C. Wu, J.L. Shao, FCC-BCC phase transformation induced simultaneous enhancement of tensile strength and ductility at high strain rate in high-entropy alloy, International Journal of Plasticity. 169 (2023) 103730. https://doi.org/10.1016/j.ijplas.2023.103730.

[67] D. You, O.K. Celebi, A.S.K. Mohammed, H. Sehitoglu, Negative stacking fault energy in FCC materials-Its implications, International Journal of Plasticity. 170 (2023) 103770. https://doi.org/10.1016/j.ijplas.2023.103770.

[68] B. Yin, S. Yoshida, N. Tsuji, W.A. Curtin, Yield strength and misfit volumes of NiCoCr and implications for short-range-order, Nature Communications. 11 (2020) 1–7. https://doi.org/10.1038/s41467-020-16083-1.

[69] F.G. Coury, C. Miller, R. Field, M. Kaufman, On the origin of diffuse intensities in fcc electron diffraction patterns, Nature. 622 (2023) 742–747. https://doi.org/10.1038/s41586-023-06530-6.

[70] D. You, O.K. Celebi, G. Gengor, A.S.K. Mohammed, W. Abuzaid, H. Sehitoglu,

Short-range ordering mechanics in FCC materials, International Journal of Plasticity. 174 (2024) 103919. https://doi.org/10.1016/j.ijplas.2024.103919.

[71] V. Bacurau, P.A. Moreira, G. Bertoli, A.F. Andreoli, E. Mazzer, F.F. de Assis, P. Gargarella, S. Figueroa, M. Widom, M. Kaufman, A. Fantin, Y. Cao, R. Freitas, D. Miracle, F.G. Coury, Comprehensive Analysis of Ordering in CoCrNi and CrNi2 Alloys, Nature Communications. 15 (2024) 7815. https://doi.org/10.1038/s41467-024-52018-w.

[72] J.H. Jun, C.S. Choi, Variation of stacking fault energy with austenite grain size and its effect on the MS temperature of γ → ε martensitic transformation in Fe-Mn alloy, Materials Science and Engineering A. 257 (1998) 353–356. https://doi.org/10.1016/S0921-5093(98)00994-0.

[73] S. Takaki, H. Nakatsu, Y. Tokunaga, Effects of austenite grain size on ε martensitic transformation in Fe-15mass%Mn alloy, Materials Transactions, JIM. 34 (1993) 489–495. https://doi.org/10.2320/matertrans1989.34.489.

[74] C. Wagner, G. Laplanche, Effect of grain size on critical twinning stress and work hardening behavior in the equiatomic CrMnFeCoNi high-entropy alloy, International Journal of Plasticity. 166 (2023) 103651. https://doi.org/10.1016/j.ijplas.2023.103651.

[75] K. Lu, L. Lu, S. Suresh, Strengthening materials by engineering coherent internal boundaries at the nanoscale, Science. 324 (2009) 349–352. https://doi.org/10.1126/science.1159610.

[76] K. Lu, Stabilizing nanostructures in metals using grain and twin boundary architectures, Nature Reviews Materials. 1 (2016). https://doi.org/10.1038/natrevmats.2016.19.

[77] M. Schneider, E.P. George, T.J. Manescau, T. Záležák, J. Hunfeld, A. Dlouhý, G. Eggeler, G. Laplanche, Analysis of strengthening due to grain boundaries and annealing twin boundaries in the CrCoNi medium-entropy alloy, International Journal of Plasticity. 124 (2020) 155–169. https://doi.org/10.1016/j.ijplas.2019.08.009.

[78] M. Schneider, F. Werner, D. Langenkämper, C. Reinhart, G. Laplanche, Effect of temperature and texture on Hall–Petch strengthening by grain and annealing twin boundaries in the MnFeNi medium-entropy alloy, Metals. 9 (2019).

https://doi.org/10.3390/met9010084.

[79] ASTM E112-13, Standard test methods for determining average grain size, 2013. https://doi.org/10.1520/E0112-13.1.4.

[80] B.H. Toby, R.B. Von Dreele, GSAS-II: the genesis of a modern open-source all purpose crystallography software package, Journal of Applied Crystallography. 46 (2013) 544–549. https://doi.org/https://doi.org/10.1107/S0021889813003531.

[81] S. Tsurekawa, S. Nakamichi, T. Watanabe, Correlation of grain boundary connectivity with grain boundary character distribution in austenitic stainless steel, Acta Materialia. 54 (2006) 3617–3626. https://doi.org/10.1016/j.actamat.2006.03.048.

[82] Y.Q. Zhang, G.Z. Quan, J. Zhao, Y.Z. Yu, W. Xiong, A Review on Controlling Grain Boundary Character Distribution during Twinning-Related Grain Boundary Engineering of Face-Centered Cubic Materials, Materials. 16 (2023). https://doi.org/10.3390/ma16134562.

[83] V.I. Levitas, Recent In Situ Experimental and Theoretical Advances in Severe Plastic Deformations, Strain-Induced Phase Transformations, and Microstructure Evolution under High Pressure, Materials Transactions. 64 (2023) 1866–1878. https://doi.org/10.2320/matertrans.MT-MF2022055.

[84] X.R. Guan, Q. Chen, S.J. Qu, G.J. Cao, H. Wang, X.D. Ran, A.H. Feng, D.L. Chen, High-strain-rate deformation: Stress-induced phase transformation and nanostructures in a titanium alloy, International Journal of Plasticity. 169 (2023). https://doi.org/10.1016/j.ijplas.2023.103707.

[85] Z.C. Cordero, B.E. Knight, C.A. Schuh, Six decades of the Hall–Petch effect – a survey of grain-size strengthening studies on pure metals, International Materials Reviews. 61 (2016) 495–512. https://doi.org/10.1080/09506608.2016.1191808.

[86] B. Guan, Y. Xin, X. Huang, C. Liu, P. Wu, Q. Liu, The mechanism for an orientation dependence of grain boundary strengthening in pure titanium, International Journal of Plasticity. 153 (2022) 103276. https://doi.org/10.1016/j.ijplas.2022.103276.

[87] P. Yu, J.P. Du, S. Shinzato, F.S. Meng, S. Ogata, Theory of history-dependent multi-layer generalized stacking fault energy— A modeling of the micro-substructure evolution kinetics in chemically ordered medium-entropyalloys,

Acta Materialia. 224 (2022) 117504. https://doi.org/10.1016/j.actamat.2021.117504.

[88] C. Chu, W. Chen, L. Huang, H. Wang, L. Chen, Z. Fu, Exceptional strength-ductility synergy at room and liquid nitrogen temperatures of Al7.5Co20.5Fe24Ni24Cr24 high-entropy alloy with hierarchical precipitate heterogeneous structure, International Journal of Plasticity. 175 (2024) 103939. https://doi.org/10.1016/j.ijplas.2024.103939.

[89] K. Jiang, J. Li, T. Suo, Extensive phase transformation in an equiatomic CrCoNi medium entropy alloy under extreme uniaxial tension, International Journal of Plasticity. 176 (2024) 103968. https://doi.org/10.1016/j.ijplas.2024.103968.

[90] M. Lamari, S.Y.P. Allain, G. Geandier, M. Ponçot, A. Perlade, K. Zhu, Behavior of TRIP-aided medium Mn steels investigated by in situ synchrotron X-ray diffraction experiments and microstructure-based micromechanical modelling, International Journal of Plasticity. 173 (2024). https://doi.org/10.1016/j.ijplas.2023.103866.

[91] X. Zhang, Y. Gui, M. Lai, X. Lu, J. Gu, F. Wang, T. Yang, Z. Wang, M. Song, Enhanced strength-ductility synergy of medium-entropy alloys via multiple level gradient structures, International Journal of Plasticity. 164 (2023). https://doi.org/10.1016/j.ijplas.2023.103592.

[92] M.A. Meyers, A. Mishra, D.J. Benson, Mechanical properties of nanocrystalline materials, Progress in Materials Science. 51 (2006) 427–556. https://doi.org/10.1016/j.pmatsci.2005.08.003.

[93] E.O. Hall, The deformation and ageing of mild steel: III discussion of results, Proceedings of the Physical Society. Section B. 64 (1951) 747–753. https://doi.org/https://doi.org/10.1088/0370-1301/64/9/303.

[94] J.N. Petch, The Cleavage Strength of Polycrystals, Journal of the Iron and Steel Institute. 174 (1953) 25–28.

[95] F. Otto, A. Dlouhý, C. Somsen, H. Bei, G. Eggeler, E.P. George, The influences of temperature and microstructure on the tensile properties of a CoCrFeMnNi high-entropy alloy, Acta Materialia. 61 (2013) 5743–5755. https://doi.org/10.1016/j.actamat.2013.06.018.

[96] J.P. Drolett, A. Galiboist, The impurity-drag effect on grain growth, Acta Metall.

Mater. 16 (1968) 1387–1399. https://doi.org/https://doi.org/10.1016/0001-6160(68)90035-7.

[97] Z. Wu, H. Bei, F. Otto, G.M. Pharr, E.P. George, Recovery, recrystallization, grain growth and phase stability of a family of FCC-structured multi-component equiatomic solid solution alloys, Intermetallics. 46 (2014) 131–140. https://doi.org/10.1016/j.intermet.2013.10.024.

[98] E. Hersent, K. Marthinsen, E. Nes, On the effect of atoms in solid solution on grain growth kinetics, Metallurgical and Materials Transactions A: Physical Metallurgy and Materials Science. 45 (2014) 4882–4890. https://doi.org/10.1007/s11661-014-2459-y.

[99] H. Hu, B.B. Rath, On the time exponent in isothermal grain growth, Metallurgical Transactions. 1 (1970) 3181–3184. https://doi.org/10.1007/BF03038435.

[100] R. Le Gall, J.J. Jonas, Solute drag effects during the dynamic recrystallization of nickel, Acta Materialia. 47 (1999) 4365–4374. https://doi.org/10.1016/S1359-6454(99)00319-5.

[101] D.A. Porter, K.E. Easterling, M. Sherif, Phase transformations in metals and alloys, 3rd ed., CRC Press Taylor & Francis Group, Boca Raton, 2009.

[102] J.B. Seol, J.W. Bae, Z. Li, J. Chan Han, J.G. Kim, D. Raabe, H.S. Kim, Boron doped ultrastrong and ductile high-entropy alloys, Acta Materialia. 151 (2018) 366–376. https://doi.org/10.1016/j.actamat.2018.04.004.

[103] G. Bertoli, G.Y. Koga, F.C. Puosso, A.J. Clarke, C.S. Kiminami, F.G. Coury, Microstructure and Wear Behavior of High-Carbon Concentration CrCoNi Multi-principal Element Alloys, Metallurgical and Materials Transactions A. 52 (2021) 3034–3050. https://doi.org/10.1007/s11661-021-06297-3.

[104] B. Kaplan, A. Markström, S. Norgren, M. Selleby, Experimental determination of the solubility of Co in the Cr-based carbides Cr23C6, Cr7C3, and Cr 3C2, Metallurgical and Materials Transactions A: Physical Metallurgy and Materials Science. 45 (2014) 4820–4828. https://doi.org/10.1007/s11661-014-2441-8.

[105] A.L. Bowman, G.P. Arnold, E.K. Storms, N.G. Nereson, The crystal structure of Cr23C6, Acta Crystallographica Section B Structural Crystallography and Crystal Chemistry. 28 (1972) 3102–3103.

https://doi.org/10.1107/s0567740872007526.

[106] H.U. Hong, B.S. Rho, S.W. Nam, Correlation of the M23C6 precipitation morphology with grain boundary characteristics in austenitic stainless steel, Materials Science and Engineering A. 318 (2001) 285–292. https://doi.org/10.1016/S0921-5093(01)01254-0.

[107] E.P. George, W.A. Curtin, C.C. Tasan, High entropy alloys: A focused review of mechanical properties and deformation mechanisms, Acta Materialia. 188 (2020) 435–474. https://doi.org/10.1016/j.actamat.2019.12.015.

[108] M. Klimova, D. Shaysultanov, A. Semenyuk, S. Zherebtsov, N. Stepanov, Effect of carbon on recrystallised microstructures and properties of CoCrFeMnNi-type high-entropy alloys, Journal of Alloys and Compounds. 851 (2021) 156839. https://doi.org/10.1016/j.jallcom.2020.156839.

[109] G. Qin, W. Xue, R. Chen, H. Zheng, L. Wang, Y. Su, H. Ding, J. Guo, H. Fu, Grain refinement and FCC phase formation in AlCoCrFeNi high entropy alloys by the addition of carbon, Materialia. 6 (2019) 100259. https://doi.org/10.1016/j.mtla.2019.100259.

[110] J.T. Fan, L.J. Zhang, P.F. Yu, M.D. Zhang, D.J. Liu, Z. Zhou, P. Cui, M.Z. Ma, Q. Jing, G. Li, R.P. Liu, Improved the microstructure and mechanical properties of AlFeCoNi high-entropy alloy by carbon addition, Materials Science and Engineering A. 728 (2018) 30–39. https://doi.org/10.1016/j.msea.2018.05.013.

[111] H. Feng, H. Li, X. Wu, Z. Jiang, S. Zhao, T. Zhang, D. Xu, S. Zhang, H. Zhu, B. Zhang, M. Yang, Effect of nitrogen on corrosion behaviour of a novel high nitrogen medium-entropy alloy CrCoNiN manufactured by pressurized metallurgy, Journal of Materials Science and Technology. 34 (2018) 1781–1790. https://doi.org/10.1016/j.jmst.2018.03.021.

[112] D.E. Jodi, J. Park, N. Park, Precipitate behavior in nitrogen-containing CoCrNi medium-entropy alloys, Materials Characterization. 157 (2019) 109888. https://doi.org/10.1016/j.matchar.2019.109888.

[113] D.E. Jodi, J. Park, B. Straumal, N. Park, Investigation on the precipitate formation and behavior in nitrogen-containing equiatomic CoCrFeMnNi high-entropy alloy, Materials Letters. 258 (2020) 126806. https://doi.org/10.1016/j.matlet.2019.126806.

[114] M. Klimova, D. Shaysultanov, A. Semenyuk, S. Zherebtsov, G. Salishchev, N. Stepanov, Effect of nitrogen on mechanical properties of CoCrFeMnNi high entropy alloy at room and cryogenic temperatures, Journal of Alloys and Compounds. 849 (2020) 156633. https://doi.org/10.1016/j.jallcom.2020.156633.

[115] D.E. Jodi, J. Park, N. Park, Strengthening of ultrafine-grained equiatomic CoCrFeMnNi high-entropy alloy by nitrogen addition, Materials Letters. 258 (2020) 126772. https://doi.org/10.1016/j.matlet.2019.126772.

[116] B.D. Cullity, S.R. Stock, Elements of X-Ray Diffraction, 3rd ed., Pearson, United States of America, 2014.

[117] P.A. Manohar, M. Ferry, T. Chandra, Five Decades of the Zener Equation, ISIJ International. 38 (1998) 913–924. https://doi.org/10.2355/isijinternational.38.913.

[118] Y.C. Huang, C.H. Su, S.K. Wu, C. Lin, A study on the hall-petch relationship and grain growth kinetics in FCC-structured high/medium entropy alloys, Entropy. 21 (2019) 297. https://doi.org/10.3390/e21030297.

[119] P.A. Beck, J. Towers, W.D. Manly, Grain growth in 70-30 brass, Trans. Am. Inst. Min. Metall. Eng. 175 (1948) 162–177.

[120] N.D. Stepanov, D.G. Shaysultanov, R.S. Chernichenko, N.Y. Yurchenko, S. V. Zherebtsov, M.A. Tikhonovsky, G.A. Salishchev, Effect of thermomechanical processing on microstructure and mechanical properties of the carbon-containing CoCrFeNiMn high entropy alloy, Journal of Alloys and Compounds. 693 (2017) 394–405. https://doi.org/10.1016/J.JALLCOM.2016.09.208.

[121] Z. Li, Interstitial equiatomic CoCrFeMnNi high-entropy alloys: carbon content, microstructure, and compositional homogeneity effects on deformation behavior, Acta Materialia. 164 (2019) 400–412. https://doi.org/10.1016/j.actamat.2018.10.050.

[122] A. Saeed-Akbari, J. Imlau, U. Prahl, W. Bleck, Derivation and variation in composition-dependent stacking fault energy maps based on subregular solution model in high-manganese steels, Metallurgical and Materials Transactions A: Physical Metallurgy and Materials Science. 40A (2009) 3076–3090. https://doi.org/10.1007/s11661-009-0050-8.

[123] R.E. Schramm, R.P. Reed, Stacking fault energies of seven commercial austenitic stainless steels, Metallurgical Transactions A 1975 6:7. 6 (1975) 1345–1351.

https://doi.org/10.1007/BF02641927.

[124] Y. Ikeda, I. Tanaka, J. Neugebauer, F. Körmann, Impact of interstitial C on phase stability and stacking-fault energy of the CrMnFeCoNi high-entropy alloy, Physical Review Materials. 3 (2019) 1–15. https://doi.org/10.1103/PhysRevMaterials.3.113603.

[125] I. Moravcik, M. Zelený, A. Dlouhy, H. Hadraba, L. Moravcikova-Gouvea, P. Papež, O. Fikar, I. Dlouhy, D. Raabe, Z. Li, Impact of interstitial elements on the stacking fault energy of an equiatomic CoCrNi medium entropy alloy: theory and experiments, Science and Technology of Advanced Materials. 23 (2022) 376–392. https://doi.org/10.1080/14686996.2022.2080512.

[126] H.J. Bae, K.K. Ko, M. Ishtiaq, J.G. Kim, H. Sung, J.B. Seol, On the stacking fault forming probability and stacking fault energy in carbon-doped 17 at% Mn steels via transmission electron microscopy and atom probe tomography, Journal of Materials Science and Technology. 115 (2022) 177–188. https://doi.org/10.1016/j.jmst.2021.11.027.

[127] Y.N. Petrov, On the electron structure of Mn-, Ni- and Cr-Ni-Mn austenite with different stacking fault energy, Scripta Materialia. 53 (2005) 1201–1206. https://doi.org/10.1016/j.scriptamat.2005.07.002.

[128] J.D. Yoo, K.T. Park, Microband-induced plasticity in a high Mn–Al–C light steel, Materials Science and Engineering: A. 496 (2008) 417–424. https://doi.org/10.1016/J.MSEA.2008.05.042.

[129] Z. Wu, C.M. Parish, H. Bei, Nano-twin mediated plasticity in carbon-containing FeNiCoCrMn high entropy alloys, Journal of Alloys and Compounds. 647 (2015) 815–822. https://doi.org/10.1016/j.jallcom.2015.05.224.

[130] Z. Wang, I. Baker, Z. Cai, S. Chen, J.D. Poplawsky, W. Guo, The effect of interstitial carbon on the mechanical properties and dislocation substructure evolution in Fe40.4Ni11.3Mn34.8Al7.5Cr6 high entropy alloys, Acta Materialia. 120 (2016) 228–239. https://doi.org/10.1016/J.ACTAMAT.2016.08.072.

[131] I. Gutierrez-Urrutia, D. Raabe, Multistage strain hardening through dislocation substructure and twinning in a high strength and ductile weight-reduced Fe–Mn–Al–C steel, Acta Materialia. 60 (2012) 5791–5802. https://doi.org/10.1016/J.ACTAMAT.2012.07.018.

[132] A. Abbasi, A. Dick, T. Hickel, J. Neugebauer, First-principles investigation of the effect of carbon on the stacking fault energy of Fe–C alloys, Acta Materialia. 59 (2011) 3041–3048. https://doi.org/10.1016/J.ACTAMAT.2011.01.044.

[133] F. Xiong, R. Fu, Y. Li, B. Xu, X. Qi, Influences of nitrogen alloying on microstructural evolution and tensile properties of CoCrFeMnNi high-entropy alloy treated by cold-rolling and subsequent annealing, Materials Science and Engineering: A. 787 (2020) 139472. https://doi.org/10.1016/J.MSEA.2020.139472.

[134] Y.N. Petrov, Effect of carbon and nitrogen on the stacking fault energy of high-alloyed iron-based austenite, International Journal of Materials Research. 94 (2003) 1012–1016. https://doi.org/10.1515/IJMR-2003-0183.

[135] V.G. Gavriliuk, H. Berns, High Nitrogen Steels: Structure, Properties, Manufacture, Applications, Materials Science and Engineering: C. 24 (1999) 394. https://books.google.com/books/about/High_Nitrogen_Steels.html?hl=pt-BR&id=6eF4AfEwF4YC (accessed January 15, 2026).

[136] N. Schell, R. V. Martins, F. Beckmann, H.U. Ruhnau, R. Kiehn, A. Schreyer, The High Energy Materials Science Beamline at PETRA III, Materials Science Forum. 571–572 (2008) 261–266. https://doi.org/10.4028/www.scientific.net/msf.571-572.261.

[137] J. Kieffer, D. Karkoulis, PyFAI, a versatile library for azimuthal regrouping, Journal of Physics: Conference Series. 425 (2013) 202012. https://doi.org/10.1088/1742-6596/425/20/202012.

[138] F.J.. Humphreys, M.. Hatherly, Recrystallization and Related Annealing Phenomena, (2012) 520.

[139] X. Liu, Z. Lei, Z. Men, In Situ Neutron and Synchrotron X-Ray Analysis of Structural Evolution on Plastically Deformed Metals During Annealing, Coatings 2025, Vol. 15, Page 1438. 15 (2025) 1438. https://doi.org/10.3390/COATINGS15121438.

[140] M. Moreno, J. Teixeira, G. Geandier, J.C. Hell, F. Bonnet, M. Salib, S.Y.P. Allain, Real-Time Investigation of Recovery, Recrystallization and Austenite Transformation during Annealing of a Cold-Rolled Steel Using High Energy X-ray Diffraction (HEXRD), Metals 2019, Vol. 9, Page 8. 9 (2018) 8.

https://doi.org/10.3390/MET9010008.

[141] S. Dey, N. Gayathri, M. Bhattacharya, P. Mukherjee, In Situ XRD Studies of the Process Dynamics During Annealing in Cold-Rolled Copper, Metallurgical and Materials Transactions A 2016 47:12. 47 (2016) 6281–6291. https://doi.org/10.1007/S11661-016-3768-0.

[142] G. Bertoli, A.J. Clarke, M.J. Kaufman, C.S. Kiminami, F.G. Coury, Influence of grain size on strain-induced phase transformation in a CrCoNi multi-principal element alloy, International Journal of Plasticity. 183 (2024) 104164. https://doi.org/10.1016/j.ijplas.2024.104164.

[143] Y. Han, H. Li, H. Feng, Y. Tian, Z. Jiang, T. He, Mechanism of dislocation evolution during plastic deformation of nitrogen-doped CoCrFeMnNi high-entropy alloy, Materials Science and Engineering: A. 814 (2021) 141235. https://doi.org/10.1016/J.MSEA.2021.141235.

[144] F. Xiong, R. dong Fu, Y. jun Li, D. li Sang, Effects of nitrogen alloying and friction stir processing on the microstructures and mechanical properties of CoCrFeMnNi high-entropy alloys, Journal of Alloys and Compounds. 822 (2020) 153512. https://doi.org/10.1016/J.JALLCOM.2019.153512.

[145] R. Li, Z. Ma, J. Wang, H. Beladi, M.R. Barnett, FCC stacking fault energies from diffraction depend on orientation, Scripta Materialia. 274 (2026) 117120. https://doi.org/10.1016/J.SCRIPTAMAT.2025.117120.

[146] M. Naeem, H. He, S. Harjo, T. Kawasaki, W. Lin, J.J. Kai, Z. Wu, S. Lan, X.L. Wang, Temperature-dependent hardening contributions in CrFeCoNi high-entropy alloy, Acta Materialia. 221 (2021) 117371. https://doi.org/10.1016/J.ACTAMAT.2021.117371.

[147] M. Naeem, H. He, F. Zhang, H. Huang, S. Harjo, T. Kawasaki, B. Wang, S. Lan, Z. Wu, F. Wang, Y. Wu, Z. Lu, Z. Zhang, C.T. Liu, X.L. Wang, Cooperative deformation in high-entropy alloys at ultralow temperatures, Science Advances. 6 (2020) 4002–4029. https://doi.org/10.1126/SCIADV.AAX4002;PAGE:STRING:ARTICLE/CHAPTER.

[148] B. Sun, T. Shen, Probing the Deformation Mechanisms of Nanocrystalline Silver by In-Situ Tension and Synchrotron X-ray Diffraction, Metals 2020, Vol. 10,

Page 1635. 10 (2020) 1635. https://doi.org/10.3390/MET10121635.

[149] A.J. Zaddach, C. Niu, C.C. Koch, D.L. Irving, Mechanical Properties and Stacking Fault Energies of NiFeCrCoMn High-Entropy Alloy, JOM 2013 65:12. 65 (2013) 1780–1789. https://doi.org/10.1007/S11837-013-0771-4.

[150] X. Tian, Y. Zhang, Effect of Si content on the stacking fault energy in γ-Fe–Mn–Si–C alloys: Part I. X-ray diffraction line profile analysis, Materials Science and Engineering: A. 516 (2009) 73–77. https://doi.org/10.1016/J.MSEA.2009.02.031.

[151] Warren B.E., X-ray diffraction, Dover, 1990.

[152] M.S. Paterson, X-ray diffraction by face-centered cubic crystals with deformation faults, Journal of Applied Physics. 23 (1952) 805–811. https://doi.org/10.1063/1.1702312.

[153] C.N.J. Wagner, Stacking faults by low-temperature cold work in copper and alpha brass, Acta Metallurgica. 5 (1957) 427–434. https://doi.org/10.1016/0001-6160(57)90060-3.

[154] R.P. Reed, R.E. Schramm, Relationship between stacking-fault energy and x-ray measurements of stacking-fault probability and microstrain, Journal of Applied Physics. 45 (1974) 4705–4711. https://doi.org/10.1063/1.1663122.

[155] G. Laplanche, M. Schneider, F. Scholz, J. Frenzel, G. Eggeler, J. Schreuer, Processing of a single-crystalline CrCoNi medium-entropy alloy and evolution of its thermal expansion and elastic stiffness coefficients with temperature, Scripta Materialia. 177 (2020) 44–48. https://doi.org/10.1016/j.scriptamat.2019.09.020.

[156] J. Łuksza, M. Rumiński, W. Ratuszek, M. Blicharski, Texture evolution and variations of α-phase volume fraction in cold-rolled AISI 301 steel strip, Journal of Materials Processing Technology. 177 (2006) 555–560. https://doi.org/10.1016/j.jmatprotec.2006.04.057.

[157] R.D.K. Misra, S. Nayak, P.K.C. Venkatasurya, V. Ramuni, M.C. Somani, L.P. Karjalainen, Nanograined/ultrafine-grained structure and tensile deformation behavior of shear phase reversion-induced 301 austenitic stainless steel, Metallurgical and Materials Transactions A: Physical Metallurgy and Materials Science. 41 (2010) 2162–2174. https://doi.org/10.1007/s11661-010-0230-6.

[158] G.K. Williamson, W.H. Hall, X-ray line broadening from filed aluminium and wolfram, Acta Metallurgica. 1 (1953) 22–31. https://doi.org/10.1016/0001-

6160(53)90006-6.

[159] T. Ungár, A. Borbély, The effect of dislocation contrast on x-ray line broadening: A new approach to line profile analysis, Applied Physics Letters. 69 (1996) 3173–3175. https://doi.org/10.1063/1.117951.

[160] R.A. Renzetti, H.R.Z. Sandim, R.E. Bolmaro, P.A. Suzuki, A. Möslang, X-ray evaluation of dislocation density in ODS-Eurofer steel, Materials Science and Engineering: A. 534 (2012) 142–146. https://doi.org/10.1016/j.msea.2011.11.051.

[161] T. Ungár, I. Dragomir, Á. Révész, A. Borbély, The contrast factors of dislocations in cubic crystals: The dislocation model of strain anisotropy in practice, Journal of Applied Crystallography. 32 (1999) 992–1002. https://doi.org/10.1107/S0021889899009334.

[162] G. Laplanche, S. Berglund, C. Reinhart, A. Kostka, F. Fox, E.P. George, Phase stability and kinetics of σ-phase precipitation in CrMnFeCoNi high-entropy alloys, Acta Materialia. 161 (2018) 338–351. https://doi.org/10.1016/j.actamat.2018.09.040.

[163] T. Gladman, Precipitation hardening in metals, Materials Science and Technology. 15 (1999) 30–36. https://doi.org/10.1179/026708399773002782.

SUPPLEMENTARY MATERIAL

S1 Sample geometry

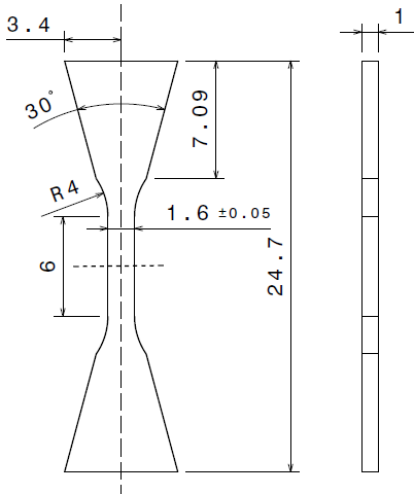

Figure S1: Schematic of the sample geometry for *in situ* tensile testing.

S2 Dislocation density calculation

The FCC dislocation density was determined by the modified Williamson-Hall method [158,159]. For analyses with loading as in Chapter 2, it is advisable to use data from transverse direction (TD) integration, as it typically develops less texture. In Chapter 2, we used a 10° TD (φ range from -5 to 5°) integration. In Chapter 4, without loading, we used a full azimuthal (φ range from 0 to 360°) integration.

The first step is to obtain the position at 2θ and the full width at half maximum (FWHM) of at least three peaks from the same phase. In this case, six FCC peaks were used (111, 200, 220, 311, 222, and 400). Next, it is necessary to subtract the instrumental broadening ($FWHM_{instrumental}$) from the broadening measured in the diffractogram ($FWHM_{measured}$), according to Equation S1, to obtain the broadening of the material/sample ($FWHM_{sample}$). A powder standard was used to obtain instrumental peak broadening (CeO_2 in Chapter 2; LaB_6 in Chapter 4). As the broadening depends on the diffraction angle, the FWHM was measured for ten peaks of the pattern, and using a linear fitting the instrumental broadening was obtained as a function of the position at 2θ of the peaks, as shown in Figure S2.

$$FWHM^2_{sample} = FWHM^2_{measured} - FWHM^2_{instrumental} \quad \textbf{Eq. S1}$$

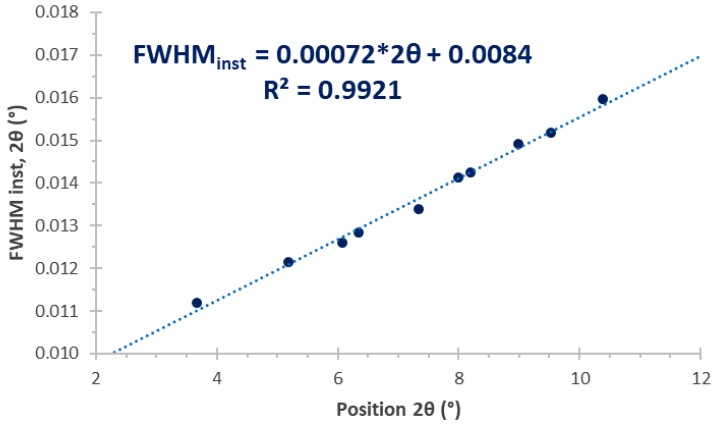

Figure S2: Example of linear fitting on the CeO_2 standard to determine the instrumental broadening as a function of the peak position at 2θ.

The modified Williamson-Hall method is described by the Equations S2-S5, where: θ is the diffraction angle (input); $FWHM_{sample}$ is the peak full width of half

maximum of the sample (input); λ is the radiation wavelength; d is average size of crystallites (output, but it was not be considered); M is a constant depending on the effective outer cut-off radius of dislocations (used as 2.0 [160]); b is the Burgers vector (0.252×10^{-9} m); ρ is the dislocation density (output); unlike the original method, the modified Williamson-Hall method considers the average dislocation contrast factor for different diffraction vectors ($\bar{C}$); $\bar{C}_{h00}$ and q can be calculated for an FCC crystal using the methodology shown in Ungár et al. (1999) [161]. In this work, a uniform distribution of screw and edge dislocations was assumed. H^2 is calculated from the (hkl) Miller indices for each peak. Basically, based on the $FWHM_{sample}$ and the position (θ) of the peaks, a graph is plotted as shown in Figure S3, and the dislocation density (ρ) is determined through the angular coefficient (AC), as shown in Equation S5.

$$\frac{2\cos(\theta) FWHM_{sample}}{\lambda} = \frac{0.9}{d} + \left(\frac{\pi M^2 b^2}{2}\right)^{1/2} \rho^{1/2} \left(\frac{2sin(\theta)}{\lambda} \bar{C}^{1/2}\right) \quad \textbf{Eq. S2}$$

$$\bar{C} = \bar{C}_{h00}(1 - qH^2) \quad \textbf{Eq. S3}$$

$$H^2 = \frac{h^2k^2 + k^2l^2 + l^2h^2}{(h^2 + k^2 + l^2)^2} \quad \textbf{Eq. S4}$$

$$\rho = \frac{2(AC)^2}{\pi M^2 b^2} \quad \textbf{Eq. S5}$$

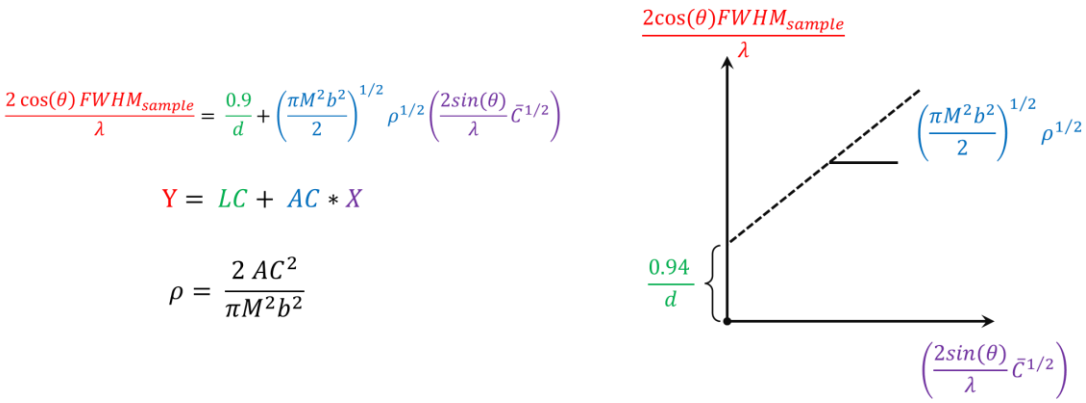

Figure S3: The modified Williamson-Hall plot and the dislocation density (ρ) equation as a function of the angular coefficient (AC).

S3 Microstructure characterization of recrystallized samples

Thermodynamic calculations via CALPHAD (represented in Figure S4) indicate that the $Cr_{40}Co_{40}Ni_{20}$ alloy solidifies at ~1400 ºC with FCC structure, and the sigma phase formation starts between 850 and 950 ºC, depending on the database (TCHEA3, PanHEA2020). However, sigma formation kinetics is relatively slow [162], and for short-time heat treatments followed by water quenching, it was expected that none or a tiny fraction of sigma would be formed. SEM-EBSD analyses, shown in Figure S5, revealed that samples 1 and 2 present an FCC matrix with a small fraction of sigma phase precipitates (0.5%), while samples 3 and 4 are single-phase FCC.

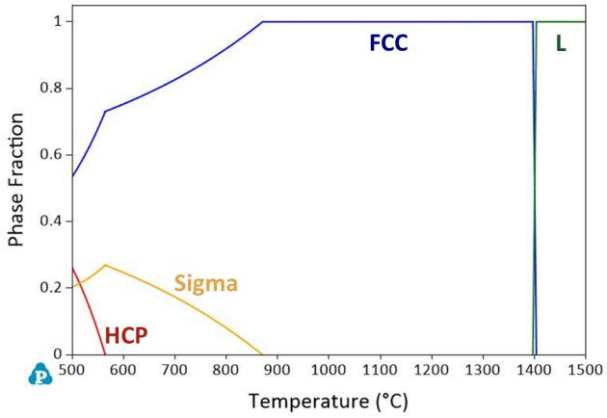

Figure S4: Thermodynamic calculations via CALPHAD (PanHEA2020 database) for the $Cr_{40}Co_{40}Ni_{20}$ alloy.

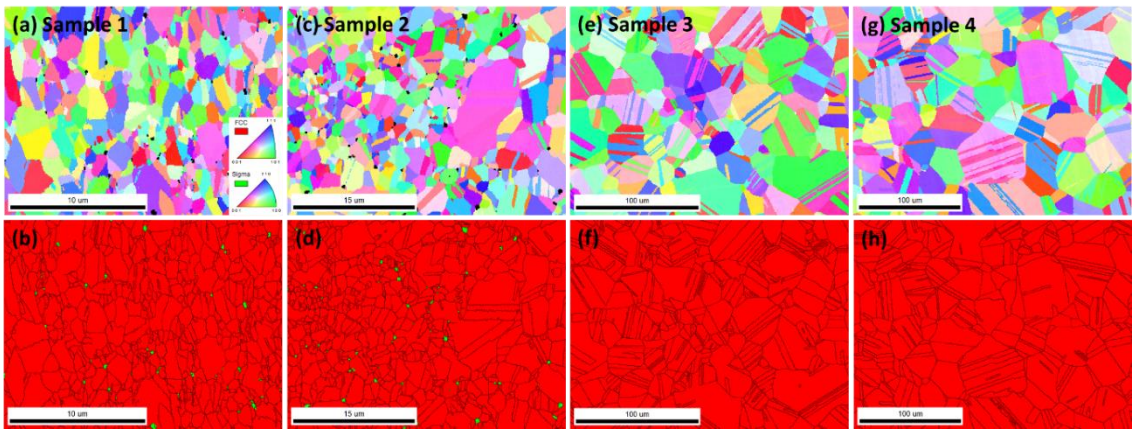

Figure S5: SEM-EBSD analyses of recrystallized samples: 1 (a,b), 2 (c,d), 3 (e,f), and 4 (g,h).

S4 Precipitation strengthening component

The increase in yield strength due to the presence of sigma phase precipitates ($\Delta\sigma_{ppt}$) was estimated using Ashby-Orowan equation (Equation S6) [163], where G is the shear modulus (89.2 GPa), b is the Burgers vector (0.252×10^{-9} m), f is the volume fraction, and d is the diameter of the precipitates.

$$\Delta\sigma_{ppt} = \frac{0.538Gb\sqrt{f}}{d} \, ln\left(\frac{d}{2b}\right) \qquad \textbf{Eq. S6}$$

Only samples 1 and 2 showed a small fraction of sigma phase precipitates, the volume fraction and diameter of the precipitates were measured through SEM-EBSD analyses, which are presented in the previous section (Figure S5). Table S1 compiles the fraction and diameter of the precipitates, the calculated precipitation strengthening component, and the yield strength. It is noted that the precipitation strengthening component is basically negligible, representing less than 2% of the yield strength in samples 1 and 2.

Table S1: Volume fraction and diameter of the precipitates for calculating the precipitation strengthening component.

Sample	*Volume fraction, f (%)*	*Diameter of precipitates, d (μm)*	*Precipitation strengthening component, $\Delta\sigma_{ppt}$ (MPa)*	*Yield strength, $\sigma_{y\ 0.2\%}$ (MPa)*
1	0.5	0.31	17.9	834
2	0.5	0.48	12.1	737
3	-	-	-	409
4	-	-	-	417

S5 *In situ* synchrotron X-ray diffraction during tensile testing

Samples with different grain/crystallite sizes were analyzed by *in situ* SXRD during tensile testing. The diffractograms (colormaps) of all samples are shown in Figure S6.

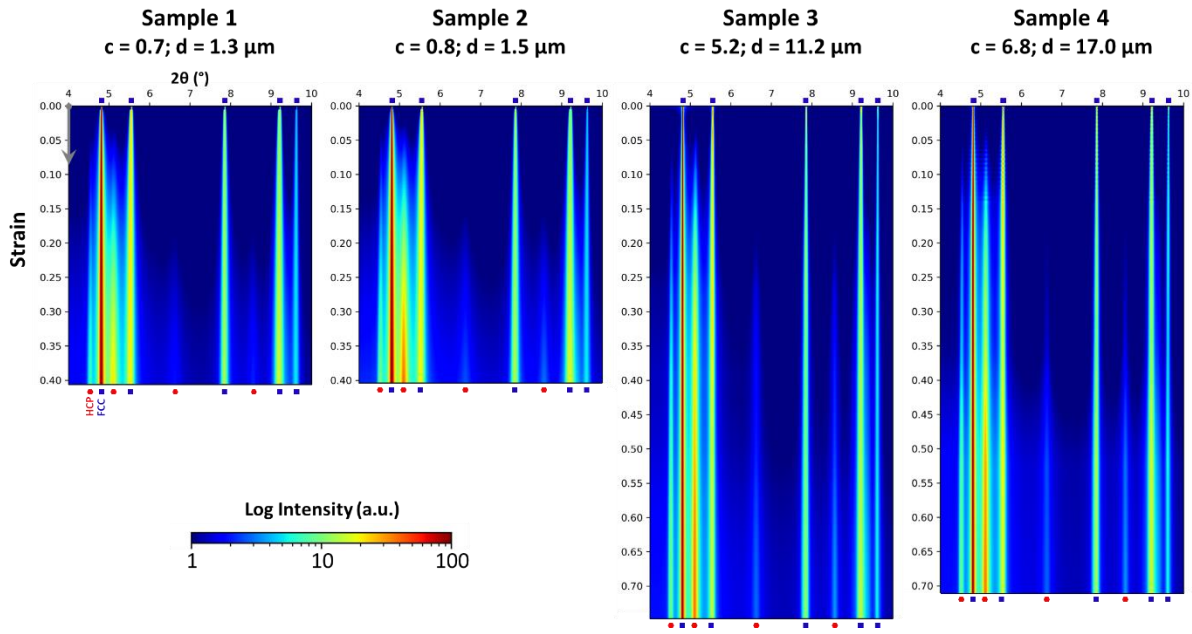

Figure S6: X-ray diffractogram throughout the tensile test vs strain, which present a partial FCC to HCP strain-induced phase transformation, reaching 35 to 52% HCP phase, depending on the initial FCC grain/crystallite size.

S6 Modeling the correlation between applied stress, HCP fraction, and grain/crystallite size

From the *in situ* SXRD data obtained throughout the tensile test, it was possible to obtain the fraction of HCP phase formed (f_{HCP}) at each stress level (σ) for samples with different grain/crystallite sizes (d or c). As shown in Section 3.4 of the paper, it was observed that the evolution of the TRIP effect follows the classic Hall-Petch equation (Equation S7). So, a Hall-Petch fitting was performed for different HCP fractions between 6.0 and 33.5% (where there are 4 points for the fitting), obtaining the slope k_{TRIP} and the intercept $\sigma_{TRIP,0}$ for each dataset, as shown in Table S2, for both grain size and crystallite size.

$$\sigma_{TRIP} = \sigma_{TRIP,0} + \frac{k_{TRIP}}{\sqrt{d}} \quad or \quad \sigma_{TRIP} = \sigma_{TRIP,0} + \frac{k_{TRIP}}{\sqrt{c}} \qquad \textbf{Eq. S7}$$

Table S2: Hall-Petch fitting for different HCP fractions between 6.0 and 33.5%: slope (k_{TRIP}), intercept ($\sigma_{TRIP,0}$), and coefficient of determination (R^2) for both grain size and crystallite size.

	Grain size (d)			*Crystallite size (c)*		
HCP Fraction	***Slope, k_{TRIP} (MPa/μm$^{-0.5}$)***	***Intercept, $\sigma_{TRIP,0}$ (MPa)***	***R^2***	***Slope, k_{TRIP} (MPa/μm$^{-0.5}$)***	***Intercept, $\sigma_{TRIP,0}$ (MPa)***	***R^2***
0.06	662.6	404.8	0.97221	502.1	378.1	0.96330
0.065	658.8	419.9	0.9699	499.2	393.4	0.96047
0.07	653.5	435.8	0.97126	495.1	409.6	0.96170
0.075	650.6	449.1	0.97166	492.9	423.0	0.96230
0.08	654.5	458.6	0.97001	495.9	432.4	0.96045
0.085	655.4	468.4	0.96866	496.5	442.1	0.95900
0.09	656.6	478.8	0.96707	497.4	452.5	0.95728
0.095	662.8	484.0	0.96952	502.1	457.5	0.95968
0.1	660.7	494.7	0.96918	500.4	468.3	0.95922
0.105	663.0	503.3	0.96775	502.2	476.8	0.95784
0.11	664.1	511.2	0.96612	503.0	484.7	0.95610
0.115	671.6	514.9	0.96804	508.6	488.1	0.95783
0.12	667.1	526.6	0.96517	505.2	500.0	0.95474
0.125	674.1	530.9	0.96588	510.4	504.1	0.95539
0.13	674.3	539.9	0.9647	510.6	513.0	0.95411
0.135	671.8	550.1	0.96348	508.7	523.4	0.95279
0.14	676.4	554.7	0.96433	512.0	527.9	0.95317
0.145	678.4	561.3	0.9651	513.5	534.4	0.95410
0.15	685.3	564.2	0.96439	518.6	537.1	0.95264
0.155	683.1	573.5	0.96421	517.0	546.5	0.95275
0.16	691.0	575.6	0.96432	522.9	548.3	0.95243

(continued on next page)

Table S2: (Continued)

	Grain size (d)			*Crystallite size (c)*		
HCP Fraction	***Slope, k_{TRIP} ($MPa/\mu m^{-0.5}$)***	***Intercept, $\sigma_{TRIP,0}$ (MPa)***	***R^2***	***Slope, k_{TRIP} ($MPa/\mu m^{-0.5}$)***	***Intercept, $\sigma_{TRIP,0}$ (MPa)***	***R^2***
0.165	686.7	587.1	0.96222	519.6	560.0	0.95054
0.17	684.4	596.9	0.9621	518.0	569.9	0.95050
0.175	684.7	604.2	0.96037	518.1	577.3	0.94848
0.18	684.4	612.1	0.96021	517.9	585.2	0.94834
0.185	685.7	618.5	0.95865	518.9	591.5	0.94671
0.19	683.2	627.1	0.95818	517.0	600.2	0.94630
0.195	683.0	635.6	0.95583	516.7	608.8	0.94376
0.2	683.3	643.5	0.95509	516.9	616.7	0.94295
0.205	683.1	651.8	0.95305	516.7	625.0	0.94084
0.21	677.6	662.3	0.9498	512.6	635.7	0.93766
0.215	675.3	671.7	0.94941	510.8	645.3	0.93712
0.22	672.1	681.1	0.94656	508.4	654.9	0.93398
0.225	667.9	691.1	0.94384	505.0	665.1	0.93082
0.23	664.4	701.3	0.9425	502.3	675.5	0.92931
0.235	662.9	711.1	0.94022	501.1	685.3	0.92704
0.24	662.1	719.6	0.93831	500.6	693.8	0.92522
0.245	657.6	730.0	0.93439	497.2	704.4	0.92140
0.25	657.4	738.7	0.9326	496.9	713.2	0.91930
0.255	653.6	748.1	0.93158	494.1	722.7	0.91832
0.26	654.8	756.3	0.92704	494.9	730.9	0.91350
0.265	649.5	765.7	0.92623	490.9	740.6	0.91272
0.27	653.3	772.4	0.92329	493.7	747.1	0.90975
0.275	649.7	782.5	0.91829	491.0	757.5	0.90457
0.28	646.9	792.2	0.91348	488.9	767.3	0.89977
0.285	645.2	802.5	0.90825	487.5	777.6	0.89467
0.29	642.8	811.5	0.90403	485.7	786.7	0.89052
0.295	641.6	820.5	0.89882	484.7	795.8	0.88503
0.3	641.6	829.1	0.89568	484.7	804.5	0.88167
0.305	642.4	836.9	0.89167	485.2	812.2	0.87764
0.31	642.5	845.2	0.88675	485.1	820.7	0.87219
0.315	641.8	854.0	0.88206	484.6	829.5	0.86752
0.32	642.7	862.6	0.87796	485.2	838.1	0.86318
0.325	641.9	871.3	0.87136	484.4	847.0	0.85596
0.33	645.9	879.7	0.87018	487.4	855.3	0.85488
0.335	645.8	888.9	0.86304	487.1	864.7	0.84698

Figure S7 show the graphical representation of the model in 2D for the $Cr_{40}Co_{40}Ni_{20}$ alloy: stress required to form a certain HCP fraction, and the fraction formed when a certain stress is applied, for different grain/crystallite sizes.

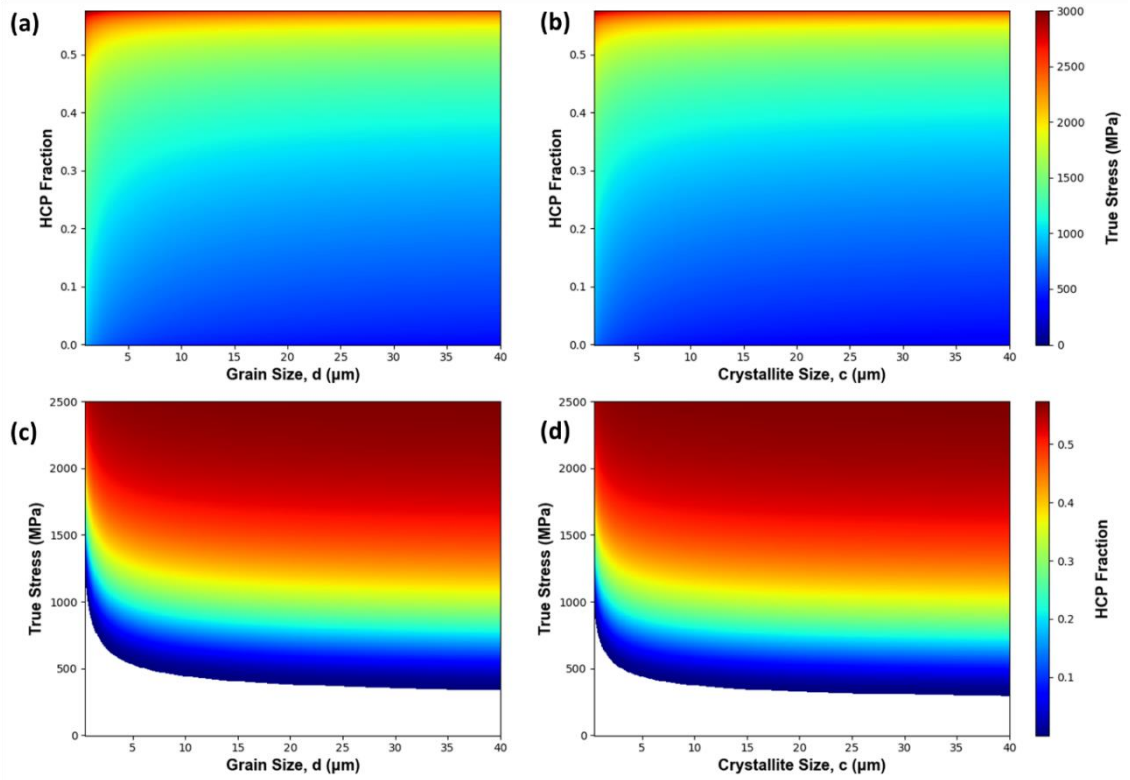

Figure S7: 2D plotting of the modeling developed in this work for the $Cr_{40}Co_{40}Ni_{20}$ alloy: (a,b) critical stress required to form a certain fraction of HCP phase (due to the TRIP effect) as a function of the initial FCC grain and crystallite size, according to Equation 7; and (c,d) HCP fraction formed as a function of grain/crystallite size and applied stress, according to Equation 9.